Comprehensive Summaries of Uppsala Dissertations
from the Faculty of Science and Technology 889

A Search for Neutrinos from Cosmic Point Sources using AMANDA-B10 with Emphasis on Limit Calculation Techniques

BY

JAN CONRAD

ACTA UNIVERSITATIS UPSALIENSIS
UPPSALA 2003

Dissertation for the Degree of Doctor of Philosophy in High Energy Physics presented at Uppsala University to be publicly examined in the Polhem lecture hall (10134) at the Ångström laboratory, on October 23, 2003, at 10.15 a.m. The examination will be conducted in English.

ABSTRACT

Conrad, J. 2003. A Search for Neutrinos from Cosmic Point Sources using AMANDA-B10 with Emphasis on Limit Calculation Techniques. Acta Universitatis Upsaliensis. *Comprehensive Summaries of Uppsala Dissertations from the Faculty of Science and Technology* 889. 160 pp. Uppsala. ISBN 91-554-5744-4.

A search for cosmic point sources of neutrinos has been performed using data taken in 1999 with the AMANDA-B10 neutrino telescope.
This work describes methods for signal and background separation and the statistical analysis of the final data sample. In particular, the multivariate method Support Vector Machines has been applied to achieve good background rejection while at the same time retaining high signal efficiency.
A grid search covering the complete northern hemisphere has been performed. The search revealed no statistically significant excess of events over the expected background from mis-reconstructed cosmic ray induced muons and atmospheric neutrino induced muons. Thus, no cosmic point sources of neutrinos have been detected. Upper limits on the neutrino flux for each cell of the grid are presented.
Twenty potential sources of neutrinos chosen among three classes of astronomical objects (Blazars, Supernova Remnants and Microquasars) have been preselected. Upper limits on the flux of cosmic neutrinos from those sources are presented.
The presence of systematic uncertainties makes the calculation of confidence limits an intricate problem. A method is presented which makes it possible to include these uncertainties into the frequentist construction of confidence intervals. Statistical properties of the presented method have been studied.

Jan Conrad, Department of Radiation Sciences, Uppsala University, Box 535, SE-751 21 Uppsala, Sweden

© Jan Conrad 2003

ISSN 1 104-232X
ISBN 91-554-5744-4

Printed in Sweden by Eklundshofs Grafiska AB, Uppsala 2003

This thesis consists of three parts:

PART I:

A search for neutrinos from cosmic point sources using AMANDA-B10

PART II:

A method to incorporate systematic uncertainties in the calculation of confidence intervals

PART III:

AMANDA-II and neutrino oscillations

Following papers are included in the thesis:

I *J. Conrad, O. Botner, A. Hallgren and Carlos P. de los Heros*
"Integrating Beliefs: The Calculation of Upper Limits on Number of Events and Flux including Systematic Uncertainties"
AMANDA Internal Report, A-IR/20010101 (2001)
TSL/ISV-03-0272

II *J. Conrad, O. Botner, A Hallgren and Carlos P. de los Heros*
"Including Systematic Uncertainties in Confidence Interval Construction for Poisson Statistics"
Phys. Rev. **D67** (2003) 012002

III *J. Conrad, O. Botner, A Hallgren and Carlos P. de los Heros*
"Coverage of Confidence Intervals Calculated in Presence of Systematic Uncertainties"
in Proceedings of Conference on Advanced Statistical Techniques in Particle Physics, Durham (2002)
TSL/ISV-02-0264

IV *J. Conrad*
"A program for confidence interval calculations for a Poisson process with background including systematic uncertainties: POLE 1.0"
submitted to Computer Physics Communications
TSL/ISV-03-0273

Contents

1 Introduction **11**

I A search for neutrinos from cosmic point sources using AMANDA-B10 **17**

2 Cosmic neutrinos **19**
2.1 Introduction 19
2.2 Known sources of neutrinos 20
2.2.1 Atmospheric neutrinos 20
2.2.2 Neutrinos from the sun and the galactic disk 21
2.3 The botany of cosmic neutrino sources 23
2.3.1 Galactic candidates 23
2.3.2 Active Galactic Nuclei 24
2.4 Physics of cosmic neutrino production 24
2.4.1 Constraining the beam: Fermi acceleration 25
2.4.2 Constraining the target: the gamma ray spectrum . . . 29
2.4.3 Combining beam and target: the neutrino flux 29
2.5 Cosmic neutrinos from beyond the Standard Model 32
2.5.1 Dark Matter candidates. 32
2.5.2 Beyond beyond the Standard Model 34

3 The detection of cosmic neutrinos **35**
3.1 Detection principle 35
3.2 Neutrino-nucleon cross section 36
3.3 Muon energy loss in matter 38
3.3.1 Ionisation & radiative loss 38
3.3.2 Čerenkov radiation. 40

3.4 Signal and background 42
3.5 Detector size and target medium 42

4 The AMANDA neutrino telescope 47
4.1 Optical modules and the detector geometry 47
4.2 Trigger system and data acquisition. 51

5 Analysis 53
5.1 Introduction 53
5.2 The analysed datasets 54
5.2.1 Experimental data 54
5.2.2 Monte Carlo simulation 54
5.3 Calibration 55
5.3.1 Time 55
5.3.2 Geometry 55
5.3.3 Optical properties of the ice 56
5.4 Data cleaning 58
5.4.1 Removing noisy OMs and unstable data taking periods 58
5.4.2 Removing non-physical hits 61
5.5 Reconstruction 61
5.6 Separation of signal from background 65
5.6.1 Variable selection 65
5.6.2 Description of cut variables 67
5.6.3 Support Vector Machines: Theory 73
5.6.4 Support Vector Machines: Application 78
5.6.5 Cut value optimisation and optimal bin size 81
5.7 The processing chain 85
5.8 Analysis of the final sample: Strategy 85
5.8.1 Grid search 87
5.8.2 Selected sources 90

6 Results 91
6.1 General definitions 91
6.1.1 Flux limits and effective area 91
6.1.2 The sensitivity 93
6.2 Angular resolution. 93
6.3 Sky-plot 98
6.4 Grid searches for point sources 100
6.4.1 Effective area and sensitivity 100

6.4.2 Excess significance 107
6.4.3 Detection threshold 110
6.5 Systematic and statistical uncertainties 111
6.6 Flux limits 116
6.6.1 Grid search 116
6.6.2 Selected sources 118
6.7 Discussion & outlook 120

II A method to incorporate systematic uncertainties in the calculation of confidence intervals 123

7 Introduction 125

8 Confidence intervals in particle physics 127

9 Summary of the papers 131
9.1 Bayesian method and algorithm (paper I) 131
9.2 The generalized Cousins & Highland method (paper II) 132
9.3 The coverage of the GCH method (paper III) 134
9.4 A routine for confidence interval calculation (paper IV) 135

10 Outlook 137

III AMANDA-II and neutrino oscillations 139

11 141
11.1 Introduction 141
11.2 Neutrino oscillations in AMANDA-II using contained events . 141
11.3 Neutrino oscillations in AMANDA-II using zenith angle distribution 143

References 146

Acknowledgements 159

CHAPTER 1

Introduction

The Nobel prize of physics in 2002 was awarded to Ray Davis, Masatoshi Koshiba and Riccardo Giacconi for pioneering contributions to astrophysics, in particular opening “two new windows on the Universe” [1]. While Giacconi worked with high energy photons (X-rays), Davis and Koshiba were rewarded for the detection of cosmic neutrinos. This discovery marked the beginning of a new discipline: neutrino astrophysics.

Cosmic Neutrinos are also the subject of the work presented in this thesis. In contrast to Davis and Koshiba who were detecting neutrinos originating from nuclear fusion in the Sun and in the core collapse of Super Nova 1987 A, thus having energies of the order of MeV, the energies of the neutrinos being focused on here are around six orders of magnitude higher ($\sim$ TeV).

Astronomy has been expanding the wavelength window in which observations are made ever since the beginning of astronomy with Galileis optical telescope [2]. Today the window extends from the very low energies of radio astronomy and microwave observations to the very high energies of GeV or even TeV gamma rays [3].

With photons as the carrier of information, expanding the window to energies above $\sim$ TeV will be essentially impossible, since photons at this energy scale are more and more inhibited by interaction with the Cosmic Microwave Background (CMB). In effect, the photon mean free path quickly decreases with energy. At PeV energies, for example, the photon mean free path is shorter than ten kpc (which corresponds approximately to the distance to the centre of our own galaxy), see figure 1.1. Using other particles as messenger is an obvious option, but there are not many choices: all charged particles will be deflected by the interstellar and intergalactic magnetic fields and thereby not preserve the direction from the source.

Neutrinos on the other hand only interact weakly and gravitationally, which means they essentially travel undisturbed even from sources at cosmological distances. Extragalactic astronomy at the $\sim$ TeV to PeV scale might therefore be only possible using neutrinos as messengers.

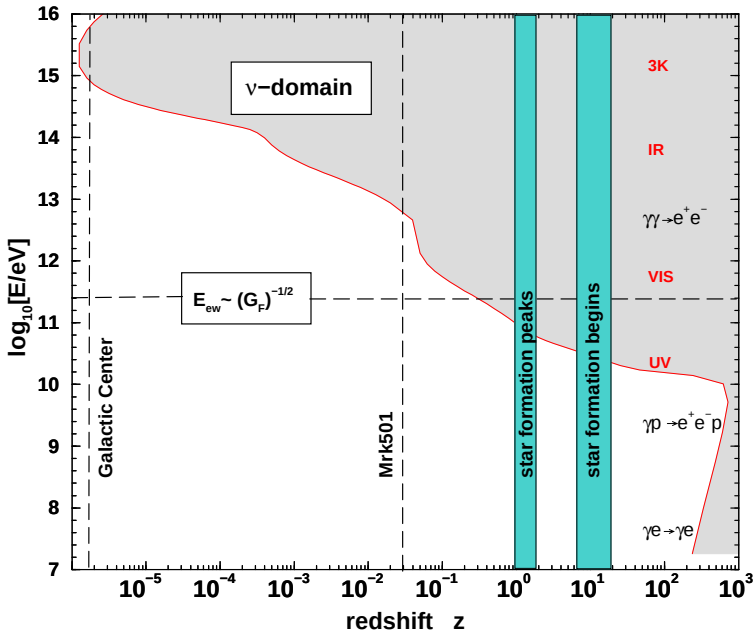

FIGURE 1.1: *The gamma ray horizon due to various absorption processes (predominantly photon pair production in the intergalactic radiation field). The area to the right of the dashed curve is invisible for gamma-ray astronomy. Also indicated are the position of the onset and peak star formation as well as the position of Mrk 501 (nearest active galaxy). Figure taken from [4]*

A particular important example of how using neutrinos as messengers might lead to new insights, is one of the long standing mysteries of nature: the origin of cosmic rays. Cosmic rays are heavy particles (mostly protons with a $\sim$ 10 % admixture of heavier elements) constantly bombarding the Earth's atmosphere. These particles have been observed with energies exceeding $\sim$ EeV. As can be seen in figure 1.2, the differential energy spectrum is a broken power law and exhibits two distinct features (the *knee* and the *ankle*), which seems to indicate that different processes might be operating in these different energy regimes. Below the knee (energies $\sim$ PeV) the spectrum is $\propto$ -2.7, above the knee it steepens (slope $\sim$ -3) and flattens again at energies above $\sim$ 10 EeV ($\sim$ -2.7).

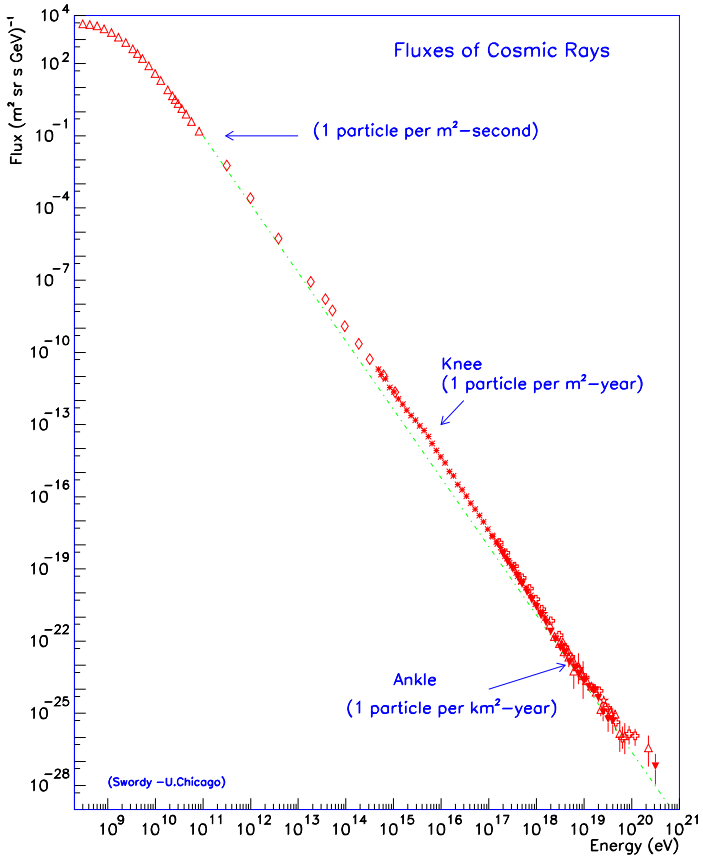

FIGURE 1.2: *The spectrum of observed cosmic rays. Figure taken from [5]*

A promising hypothesis for the origin of cosmic rays is that they are produced and accelerated at cosmological and galactic sites, such as Active Galactic Nuclei (AGN), Super Novae (SN) and Gamma-Ray Bursts (GRB), which release huge amounts of energy. Protons are charged particles thus (as discussed previously) deflected by intergalactic magnetic fields and consequently the connection between the observed cosmic rays and cosmological objects can not be established from the directions of the cosmic rays alone. However, if these objects indeed are sources of cosmic rays, they will most likely also produce high energy neutrinos, following from particle physics arguments (see section 2). The detection of high energy neutrinos from hypothetical sources of cosmic rays would therefore be not only a major step in the understanding of the origin of cosmic rays but also toward understanding the physical processes at work in the most energetic objects in our universe.
Detectors for high energy neutrinos (*neutrino telescopes*) are designed to detect the secondary charged particles produced in neutrino interactions. From the detected particle, it is attempted to infer the direction of the origin of the parent neutrino and, if possible, the type of neutrino and its energy.
The analysis presented in this thesis has been performed with data taken by the Antarctic Muon and Neutrino Detector Array (AMANDA) situated at the South Pole. AMANDA is one of the two operational neutrino telescopes in the world, the other one being the BAIKAL [6] neutrino telescope situated in Lake Baikal in Russia. With AMANDA the feasibility of high energy neutrino detection has been proven [7] and atmospheric neutrinos (see section 2.2) have been observed [8]. It has furthermore been possible to put limits on the flux from hypothetical neutrino point sources [9], the diffuse flux of high energy neutrinos [10], neutrino-induced cascades [11], Gamma Ray Bursts [12] and other physical processes such as flux from neutrinos from dark matter annihilation [13] and magnetic monopoles [14]. AMANDA can be considered as a proto-type for a considerably larger neutrino telescopes: the IceCube neutrino detector [15], which is expected to have the sensitivity to decisively rule out or confirm models of cosmological neutrino production. Apart from possible physics discoveries of AMANDA, the operation of the array and the analysis of data taken with this first generation neutrino telescope thus constitute a necessary step toward the next generation of neutrino telescopes.

This thesis is divided into three parts. Part I is concerned with an analysis which constitutes one of the prime goals of neutrino telescopes: the search for cosmic point sources of high energy neutrinos.
The last step of this analysis will be the calculation of a confidence interval

for the neutrino flux. The presence of significant systematic uncertainties represents a considerable complication of this calculation. Part II describes a possible solution to this problem.
Part III describes an assessment of the sensitivity of AMANDA to neutrino oscillations.

Part I

A search for neutrinos from cosmic point sources using AMANDA-B10

CHAPTER 2

Cosmic neutrinos

2.1 Introduction

The particle physics process, which is central in the production of high energy cosmic neutrinos, is proton collision with some target:

$$\begin{aligned} p + X \rightarrow \quad & M + Y \\ & \hookrightarrow \quad \mu^{\pm} + \nu_{\mu}\,(\bar{\nu}_{\mu}) \\ & \qquad\quad \hookrightarrow e^{\pm} + \nu_{e}\,(\bar{\nu}_{e}) + \bar{\nu}_{\mu}(\nu_{\mu}) \end{aligned} \tag{2.1}$$

where M can be either $\pi^{\pm}$ (which decays to 100 % into muons), a $K^{\pm}$ (which decays to muons with a branching ratio of about 65 %), or a K_L^0 (which subsequently decays into $\pi^{\pm}$ + e$^{\mp}$($\mu^{\mp}$) + ν. Y is determined by the character of X which is either another hadron or a photon.
Thus, if there are processes which accelerate protons to high energies (beam) and there is a medium (target) in which these protons interact to produce kaons and pions, there will be production of high energy neutrinos.
As described in the previous section, cosmic rays constitute a natural beam of protons and the Earth's atmosphere constitutes a natural target. The Earth's atmosphere consequently should yield neutrinos. The existence of those *atmospheric neutrinos* has not only been confirmed by experiment (see e.g. [8]) but their spectrum has been measured and used to determine parameters of neutrino oscillations, see for example [16] for a recent review. Furthermore, other celestial bodies (such as the Sun) and the interstellar gas provide possible targets for the cosmic ray beams. The neutrinos from the atmosphere and the interstellar gas hereby form an isotropic (or nearly isotropic) background to the search for point sources, whereas the Sun is a possible point source itself.

We will discuss these guaranteed sources of cosmic neutrinos further in section 2.2.
As mentioned earlier, the sources of cosmic rays are not known but they are certainly good candidates for being proton accelerators. If in addition there is a medium that surrounds the acceleration sites which acts as a target, production of neutrinos would be the consequence. Vice versa, if neutrinos could be observed from a cosmic point source this would indicate that proton acceleration takes place, thereby supporting the hypothesis that it is also a source of cosmic rays. On the other hand, it is known from astronomical observations of photons from the visible to the TeV range that there are objects in the universe which release huge amounts of energy. Considering the high energies at which cosmic rays are observed, these objects constitute prime candidate sources for both cosmic rays and high energy neutrinos.
In the next section we will describe known sources for cosmic neutrinos and their impact on the search for point sources. We will then turn to the botany of astronomical candidate sources for high energy neutrinos. The physics model describing the neutrino production in those objects will be described in section 2.4. In particular, we will present a very simple but illustrative estimate for the flux of neutrinos originating from Active Galactic Nuclei. Finally, we will briefly discuss some of the more exotic sources of cosmic neutrinos involving non standard-model physics.

2.2 Known sources of neutrinos

2.2.1 Atmospheric neutrinos

Cosmic Rays are constantly colliding with the Earth's atmosphere. These cosmic rays consist mainly of protons with a small ($\sim$ 10 %) admixture of heavier nuclei. In the collision, mesons are produced which subsequently decay to yield neutrinos, see process 2.1.
For pions and kaons, decay into leptons competes with interaction with nuclei in the atmosphere. The rates of both processes become comparable when the mean free path of the mesons in air is comparable to the mean distance the meson can travel during its lifetime, i.e.:

$$c\tau \frac{E}{mc^2} \simeq \frac{1}{n\sigma} \tag{2.2}$$

where E and m are the energy and the mass of the meson, c the speed of light, n is the number density of atmospheric nuclei and σ the meson cross

section. One consequence of this relation is that the horizontal neutrino flux is expected to be larger than the vertical (see figure 2.1), the reason being that mesons produced by cosmic rays with shallow zenith angle will be produced at higher altitude (lower density), giving the mesons more time to decay. This density effect introduces a $\sec\theta_{zenith}$ dependence of the atmospheric neutrino spectrum. The decay channel dominates for vertical muons up to energies of $\sim$ 100 GeV, which is why their energy spectrum in this region follows the spectrum of incident cosmic rays and is well described by a power law spectrum

$$\frac{d\Phi_\nu}{dE_\nu} \propto E^{-\gamma} \tag{2.3}$$

with $\gamma = 2.7$ [17]. Above 100 GeV the spectrum will start to become steeper since more and more mesons interact before decaying. At energies $\gg 1$ TeV the spectrum is characterised by a power law index $\gamma = 3.7$ (i.e. one power steeper than the incident cosmic ray spectrum). It should be noted that because of the effect of different interaction length of the cosmic rays at different zenith angles this change of slope is zenith dependent.

Neutrinos are also produced in charmed meson decay. These mesons continue to contribute to the neutrino spectrum with the shallower slope until much higher energies ($\sim$ 50 PeV), since the lifetimes of charmed mesons are much shorter (for $\pi^\pm$, $c\tau \sim$ 7.8 m, as compared to 315 μm for a $D^\pm$ charmed meson). Thus, despite the fact that the contribution of charmed mesons to the neutrino flux is generally small, it will eventually dominate the contributions from other mesons. Estimates of the energy where this cross over takes place differ between 10 TeV and 100 PeV (see [18] and references therein). Contributions of charmed mesons to the atmospheric neutrino flux are not taken into account in this work. Figure 2.1 presents a summary of model calculations for atmospheric neutrinos up to energies of 10 TeV.

2.2.2 Neutrinos from the sun and the galactic disk

The same process that produces high-energy neutrinos in the atmosphere also leads to a contribution of neutrinos from other targets for cosmic rays, such as the Sun and the galactic disk.

The density is lower in the solar atmosphere than in the Earth, therefore there will be no steepening of the spectrum. Calculations [24] predict the flux of neutrinos from the sun to be larger than the atmospheric neutrino flux (calculated in a 1 square degree pad) above energies $\sim$ 10 TeV.

Another possible target is the interstellar matter located in the galactic disk.

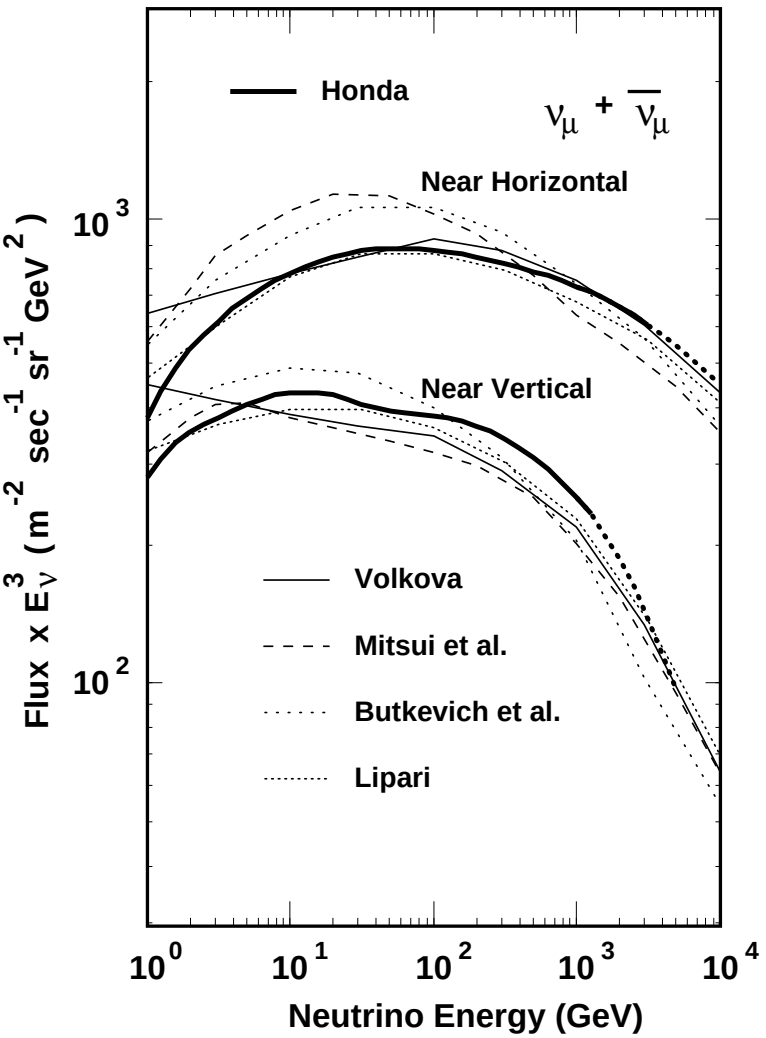

FIGURE 2.1: *The flux of atmospheric neutrinos. Five calculations are compared for near horizontal ($\cos\theta_{zenith}$ =0 - 0.1) and near vertical ($\cos\theta_{zenith}$ =0.9 - 1). The solid line refers to a calculation performed by [19] (Honda). The other curves are calculations performed by [20] (Volkova), [21] (Mitsui et. al.), [22] (Butkevich et al) and [23] (Lipari). Figure taken from [19]*

The low density here again leads to a spectrum which is not as steep as the atmospheric neutrino spectrum. Eventually, it therefore dominates the atmospheric neutrino spectrum (E $\sim$ several hundred TeV) [25] [26].

2.3 The botany of cosmic neutrino sources

In this section we will give an account for candidates for cosmic point sources. It should be mentioned that we will not be complete in this effort. Among sources we will not discuss are those very unlikely to give an appreciable flux (like cosmic rays interacting in the interstellar medium of other galaxies or in intergalactic medium of clusters) and Gamma Ray Bursts which are very promising candidates for neutrino emission, but which are subject of a dedicated analysis [12].

2.3.1 Galactic candidates

Super Nova Remnants Super Nova remnants (SNR) are blast waves which are produced in the core collapse of massive stars ($M > 8M_{\odot}$). The total energy released in such a core collapse is $\sim 10^{65}$ eV, from which about one percent is transferred to the blast wave. SNR are believed to be prime candidates for cosmic ray acceleration up to energies of $\sim 10^2$ - 10^3 TeV [4]. The target for neutrino production in this case would be provided by the interstellar medium. The resulting high energy neutrino fluxes might dominate the atmospheric neutrino spectrum above neutrino energies of $\sim$ 20 TeV [4] (in a one square degree aperture). This estimate has been obtained from measured gamma flux of the SNR Cassiopeia A and γ Cygni by equating gamma-flux and neutrino flux, which is a technique similar to the one we will use in section 2.4.

Microquasars Microquasars (MQ) are formed by accreting black holes with black hole masses, $M_{BH} \geq 3M_{\odot}$. They exhibit a structure very similar to Active Galactic Nuclei (AGN), see section 2.3.2, with jets emanating from the accretion disk and a variable X-ray spectrum, but on a considerably smaller scale (the typical black hole mass of AGN is $M_{BH}^{AGN} \sim 10^8 M_{\odot}$). The acceleration of cosmic rays would be performed in the jet and the target is provided by the photon radiation of the accretion disk or the synchrotron radiation of the electrons in the jet (see section 2.3.2 and 2.4). Scaling from the models used to explain AGN leads to the prediction that acceleration of cosmic rays to energies of $\sim 10^3$ TeV [4], corresponding to neutrino energies of $\mathcal{O}$ (100 TeV), is

possible. [27] examined a sample of 20 MQs and calculate individual neutrino flux predictions from source properties inferred from other observations. The highest flux levels reach the ones expected for SNR.

2.3.2 Active Galactic Nuclei

Active Galactic Nuclei (AGN) are the most powerful objects in the universe with bolometric luminosities of $\sim 10^{30}$ eVs^{-1}. These luminosities are sustained over long time periods and radiated from very small regions ($\sim$ size of our planetary system). The only explanation which theoreticians have been able to come up with is the energy release of gravitational energy due to accretion onto a very massive black hole typically of the order of M = $10^8 M_{\odot}$.
Protons are accelerated either in the accretion process onto the black hole (*AGN core models*) or in jets which emerge perpendicular to the accretion disk (*AGN jet models*). Of special interest is here a class of AGN where the jet emanates along the line of sight, so called *blazars*, since they are sources of gamma rays in the GeV - TeV region supporting the hypothesis of proton acceleration [28]. The target in the case of AGN is either the photons originating in the accretion disk or synchrotron radiation of electrons accelerated with the jet depending on how far from the disk the acceleration takes place. Another possibility is the collision of the jets with the intergalactic medium.
Blazars are prime candidates for the highest energy cosmic rays, since they are probably capable of accelerating protons up to energies of $\sim$EeV. If indeed protons are accelerated in blazars, then the high energy gammas can be explained by neutral pion decay, $\pi^{\circ} \rightarrow \gamma\gamma$ (*proton blazar*). However, it can not be ruled out that the gamma radiation is produced by inverse Compton scattering of electron synchrotron radiation (*electron blazar*). The observation of neutrinos from blazars would be more or less decisive in that matter.

2.4 Physics of cosmic neutrino production

The goal of this section is to obtain a simple estimate for the flux of cosmic neutrinos from a proton blazar (see section 2.3.2). This is done to exemplify one common method to calculate the expected neutrino flux from candidate sources such as those described in the previous section.
The general strategy is to first obtain an estimate of the expected maximal energy of neutrinos and the spectral shape of the neutrino spectrum (which essentially is determined by the acceleration mechanism and the target spectrum). The second step is then to relate the expected neutrino flux to some

observed flux of particles, in our case the flux of gamma rays.

2.4.1 Constraining the beam: Fermi acceleration

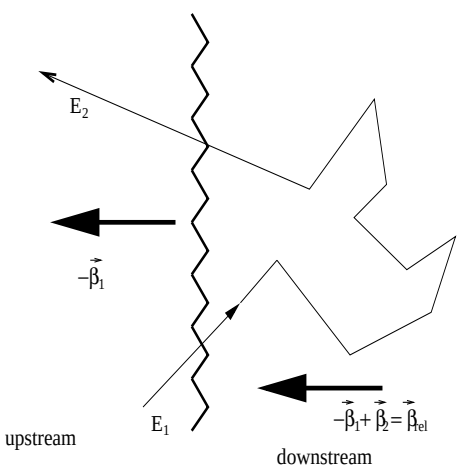

FIGURE 2.2: *Schematics of Fermi Acceleration. For the definition of the quantities, see text*

Fermi acceleration is a mechanism to transfer kinetic energy of a moving magnetised plasma to single charged particles. The Fermi mechanism - with only a few assumptions - provides a spectrum of charged particles which has a slope similar to that observed in cosmic rays, which makes Fermi acceleration the prime candidate for providing the acceleration in cosmic rays.
Consider a test particle which undergoes stochastic collisions and in each collision gains an amount of energy proportional to its own energy, $\delta E = E\xi$. Consider furthermore that the region where these collisions can take place is finite such that a particle has a finite probability, P_{esc}, of escaping that region. Then, the number of particles with an energy $>$ E, can be calculated to be [29]:

$$N(>E) \propto \frac{1}{P_{\text{esc}}} \left(\frac{E}{E_\circ}\right)^{-\frac{P_{\text{esc}}}{\xi}} \tag{2.4}$$

where $E_\circ$ is the test particle's energy at injection. The integral energy spectrum of particles will be a power-law with an index depending on the fraction of energy transferred in each collision and the probability for the particle to escape the acceleration region. Qualitatively, such a spectrum behaves as expected. The higher the escape probability and the smaller the energy transfer, the steeper spectrum one would expect. Vice versa, a low escape probability and a high energy transfer should lead to a shallow spectrum. Both ξ and P_{esc} are determined by the physics of the process, but only the stochastic nature of the acceleration process and the fact that there is a finite probability for the particle to escape the accelerating region leads to a power-law spectrum.
Turning to the physics process, we consider a shock wave moving through a

magnetised plasma and a test particle traversing the shock front back and forth, see figure 2.2 and [29]. The test particle is supposed to start out in the region in front of the shock front ("upstream"), traverse the shock front to the region of shocked gas ("downstream") where it undergoes repeated scattering on magnetic field irregularities present in the shocked gas, and finally traverses the shock front again returning to the upstream region of unshocked gas (we will refer to this process as one *cycle*). If the particle initially has energy, E_1, the question we are interested in is, what will be its energy, E_2, after completing the cycle ?

In answering this question, we will make an important assumption: the scattering process is completely elastic, i.e. the magnetic field irregularities (scattering centres) are assumed to be at rest with respect to the local gas velocity, which in turn implies that the energy of the test particle is not changed by the scattering. The velocity of the test particle, however, changes such that after a few scatterings the average motion will coincide with that of the surrounding gas. Furthermore, we assume that the particle enters the downstream region under an angle θ_d and leaves the downstream region again under an angle θ_u, where the angles are defined with respect to the normal to the plane of the shock front. Then the energy of the particle upon re-entering the upstream region, E_2, is related to the initial energy of the particle, E_1, by the combination of Lorentz factors (upstream → downstream → upstream)

$$E_2 = E_1 \cdot \Gamma_{\text{rel}}^2 (1 - \beta_{\text{rel}} \cos\theta_d)(1 + \beta_{\text{rel}} \cos\theta_u) \tag{2.5}$$

where Γ_{rel} is the Lorentz-factor between the upstream and downstream frame of reference and β_{rel} is the relative velocity of these frames [1] (see figure 2.2 for reference). In the derivation of equation 2.5, it was assumed that the test particle is sufficiently relativistic, such that $pc \sim E$.

The average energy gain per cycle is given by averaging equation 2.5 over $\cos\theta_d$ and $\cos\theta_u$. Assuming an isotropic flux and a plane shock wave, averaging $\cos\theta_d$ in (-1 $\leq$ $\cos\theta_d$ $\leq$ 0) and $\cos\theta_u$ in (0 $\leq$ $\cos\theta_u$ $\leq$ 1) yields $< \cos\theta_d >= -2/3$ and $< \cos\theta_u >= 2/3$, [29]. Inserting these values into equation 2.5 results in:

$$\xi = \Gamma_{\text{rel}}^2 \left(1 + \frac{4}{3}\beta_{\text{rel}} + \frac{4}{9}\beta_{\text{rel}}^2\right) - 1 \sim \frac{4}{3}\beta_{\text{rel}} \tag{2.6}$$

with $\frac{E_2}{E_1} = (1 + \xi)$. The approximate form holds for a non-relativistic shock. This type of shock acceleration is sometimes called *first order shock acceleration*, since the fractional energy gain per collision is proportional to the first

[1] nota bene: the downstream frame of reference is the lab frame

order of the velocity.
In the considered case of a plane (indefinite) shock front, once a test particle has entered the downstream region it has a finite probability of getting scattered further downstream (instead of getting scattered back to the upstream region), thereby being lost for further acceleration cycles. The escape probability is given by the ratio of the rate of particles crossing the shock front and the rate of particles getting scattered away further downstream. The former is given by projecting an isotropic flux of test particles on the shock wave plane, the latter is proportional to the velocity, β_2, with which the shocked gas moves away from the gas in the upstream region. The result [29] is:

$$P_{\text{esc}} = 4\beta_2 \tag{2.7}$$

and combining equation 2.6 and equation 2.7:

$$\gamma = \frac{P_{\text{esc}}}{\xi} = 3\frac{\beta_2}{\beta_{\text{rel}}} = 3 \cdot \frac{r}{1-r} \tag{2.8}$$

with $r = \beta_2/\beta_1$. r can be determined from the kinetic theory of gases and is dependent on the strength of the shock and the specific heats of the gas involved. For a mono-atomic gas and a strong shock (β_1 much greater than sound speed in the gas), r = 1/4 and consequently γ = 1. and thus the differential spectrum of test particles is given by:

$$\frac{dN}{dE} \propto E^{-2} \tag{2.9}$$

Remembering the fact that the scattering is caused by magnetic field irregularities, it should be noted that the implicit assumption in the above derivation is that the magnetic field is parallel to the shock normal. Otherwise, there will be an electric field induced in the rest frame of the shock front leading to a gain in energy for a charged particle crossing the shock.
We will now turn to the question of the maximal energy which can be obtained by Fermi acceleration. For this we introduce the cycle time, T_{cyc}, which is the time it takes for the particle to traverse the shock from upstream to downstream and back, thereby gaining an amount of energy ξE. With this definition the acceleration rate can be expressed as:

$$\frac{dE}{dt} = \frac{\xi E}{T_{\text{cyc}}} \tag{2.10}$$

In order to estimate the maximal energy we will have to integrate equation 2.10 over the lifetime of the accelerator (the time until the shock wave decays) and

we have to know the cycle time.
The cycle time is given by the sum of the times that the particles spend in the upstream region and in the downstream region:

$$T_{\text{cyc}} = t_{\text{up}} + t_{\text{down}} \tag{2.11}$$

Introducing the scattering length, D, the average time a particle spends in a region moving with velocity β is given by $t = \frac{D}{c\beta}$ (see [29] for a derivation). For simplicity we will assume the scattering process in the upstream and downstream region to be the same. Then:

$$T_{\text{cyc}} = 4D\left(\frac{1}{c\beta_1} + \frac{1}{c\beta_2}\right) \tag{2.12}$$

where D is the typical scattering length. The argument to constrain D is that the scattering length can not be smaller than the Larmor radius of the particle, $r_L = \frac{E}{qB}$. The general idea is that a particle with a larger Larmor radius would not respond to the irregularities. Thus, $D_{\text{min}} \simeq r_L$ and inserting this into equation 2.10 and integrating to a finite duration of the shock, T_A, results in:

$$E_{\text{max}} \leq \frac{1}{20}\,\beta_1 \cdot qB \cdot (\beta_1 c \cdot T_A) \tag{2.13}$$

where we have assumed a strong shock (r = 1/4, as above) and made use of equation 5.41.
Note that $(c\beta_1 \cdot T_A)$ can be interpreted as the total size of the accelerating region R_{acc}. For a relativistic shock the result resembles the one given here (see e.g. [30]):

$$E_{\text{max}} \simeq \Gamma_1 \cdot qB \cdot R_{\text{acc}} \tag{2.14}$$

It should be noted that for this equation to be valid, the acceleration efficiency has to be 100 %. Effects which are not included are for example the energy loss of charged particles due to synchrotron radiation (see e.g. [31]).
In summary, Fermi acceleration produces a universal spectrum of particles which has a power-law index close to what is needed to explain the cosmic ray spectrum. The small deviation might be explained by the implicit assumption made here that the test particle does not influence the magnetic fields in the acceleration region, whereas in reality, the cosmic rays themselves might induce hydromagnetic waves and irregularities, see e.g. [29] [30].

2.4.2 Constraining the target: the gamma ray spectrum

In what follows we will consider the following channel for neutrino production:

$$p + \gamma \rightarrow \Delta \rightarrow n\pi^+ \tag{2.15}$$

with subsequent decay of the pions into neutrinos. The target will consequently be gammas.
The spectrum of gammas will be assumed to be a black-body spectrum. The typical energy of this spectrum is $E_\gamma = 10$ eV (UV bump in AGN spectra). It can be shown that the neutrino spectrum in the above case will have the same slope as the incident proton spectrum, i.e. it will be proportional to E^{-2} [32].
In making the above assumption we constrain ourselves to acceleration taking place near the black hole, since the target photon spectrum for protons accelerated far away from the accretion disk will be predominantly produced by the synchrotron radiation of the accelerated electrons in the jet (see section 2.3.2). Synchrotron radiation exhibits a power-law spectrum, $E^{-\alpha}$, leading to a resulting neutrino spectrum proportional to $E^{-\gamma-\alpha}$ [4].

2.4.3 Combining beam and target: the neutrino flux

We have now estimated the shape of the cosmic ray spectrum and its maximal energy (beam), fixed the shape of the gamma ray spectrum and its approximate energy (target) and thereby determined the shape of the neutrino spectrum. In this section we will combine this information to obtain a very simple estimate on the neutrino flux from a cosmic point source. The absolute normalisation of the neutrino spectrum will be estimated from the observed gamma ray luminosity of a well known blazar. As mentioned in the previous section, the calculation will be performed using the Δ-approximation, meaning we assume the pion production to proceed via the Δ-resonance and neglect contributions from other resonances and inelastic scattering.
In a first step we estimate the relationship between the neutrino luminosity and the gamma ray luminosity. Neutrinos are exclusively produced in charged pion decay. Gammas, on the other hand, are predominantly produced by neutral pion decay ($\pi^\circ \rightarrow \gamma\gamma$) but also get contributions from the leptons produced in the charged pion decay (see process 2.1) as well as Bethe-Heitler pair production, $p\gamma \rightarrow e^+e^-p$ [31]. The four leptons originating in the charged pion decay (ν_μ, ν_e, e^+ and $\bar{\nu}_\mu$) on average all carry the same amount of energy. Thus, the e^+ contributes to the gamma flux mainly by synchrotron radiation [31] with $\sim$ 25 % of the pion energy.

At the Δ resonance, the rate of neutral pion production is roughly double the rate of charged pion production:

$$\frac{\Gamma(p\gamma \to \Delta \to p\pi^{\circ})}{\Gamma(p\gamma \to \Delta \to n\pi^{+})} \sim \frac{2}{1} \tag{2.16}$$

Thus following picture emerges: from the total energy going into the pion production ($\frac{1}{4} \cdot \frac{1}{3}$) go into gamma rays from charged pion decay, and $\frac{2}{3}$ from neutral pion decay. Thus the total fraction contributed the gamma luminosity is ($\frac{2}{3} + \frac{1}{12} = \frac{3}{4}$). The fraction going into the neutrinos is consequently ($\frac{1}{3} \cdot \frac{3}{4} = \frac{1}{4}$). This implies that naively one expects the neutrino and gamma luminosities to be related like:

$$\frac{L_\nu}{L_\gamma} = \frac{1}{3} \tag{2.17}$$

If the contribution to L_γ by Bethe-Heitler pair production is included, the result turns out to be [33]:

$$\frac{L_\nu}{L_\gamma} = \frac{3}{13} \tag{2.18}$$

With this knowledge, we can proceed to calculate the spectrum of neutrinos. Whereas [33] perform the calculation for a spectrum $\propto E^{-1}$, it was mentioned previously that for pion production on a black-body photon target neutrinos are expected to exhibit a spectrum $\propto E^{-2}$.

$$\frac{dN_\nu}{dE_\nu} = \mathcal{N} \frac{E_\nu^{-2}}{E_{\nu,\text{max}}} \tag{2.19}$$

Thus it holds for the neutrino luminosity:

$$L_\nu = \mathcal{N} \int_{E_{\nu,\text{min}}}^{E_{\nu,\text{max}}} dE_\nu E_\nu \frac{E_\nu^{-2}}{E_{\nu,\text{max}}} = \frac{3}{13} L_\gamma \tag{2.20}$$

which upon integration yields the normalisation constant $\mathcal{N}$ and inserting into equation 2.19 gives the spectrum of neutrinos:

$$\frac{dN_\nu}{dE_\nu} \sim \frac{3}{13} \left(\frac{L_\gamma}{E_{\nu,\text{max}}^2 \ln \frac{E_{\nu,\text{max}}}{E_{\nu,\text{min}}}} \right) \left(\frac{E_\nu}{E_{\nu,\text{max}}} \right)^{-2} \tag{2.21}$$

The minimal and maximal neutrino energies can be related to minimal and maximal proton energies by including the average fraction of the momentum of the pion relative to the incident proton, $< x_F > \sim 0.2$, and the fraction of

energy of the neutrino relative to the pion, which assuming equipartition is $\frac{1}{4}$, thus:

$$E^{\nu}_{\text{max,min}} = \frac{1}{4} < x_F > \cdot E^{p}_{\text{max,min}} \sim 0.05\ E^{p}_{\text{max,min}} \tag{2.22}$$

The minimum proton energy is given by the proton threshold to produce pions via the Δ resonance on a photon target. This is dependent on the photon energy and is given by:

$$E'_p > \frac{m_\Delta^2 - m_p^2}{4 \cdot E'_\gamma} \tag{2.23}$$

in the co-moving (proton) frame. In the lab frame and after inserting the mass values, this can be expressed as [34]:

$$E_p > 1.4 \cdot 10^{19}\text{eV} \left(\frac{\Gamma}{30}\right)^2 \left(\frac{10\text{eV}}{E_\gamma}\right) \tag{2.24}$$

As mentioned in the previous section, we consider a spectrum as produced by an accretion disk, i.e. a black body spectrum with a characteristic energy of $\sim$ 10 eV. We will for simplicity assume that all photons have this energy, which is a not too bad approximation for a black body spectrum. The minimal neutrino energy is related to the proton threshold energy by equation 2.22, yielding $E_{\nu,min} \sim 770$ TeV. We recall that the maximal proton energy (hence neutrino energy) will be determined by the magnetic field, the size of the acceleration region and the boost factor of the shock wave, see equation 2.14. The size of the acceleration region and the magnetic field is determined by observations and typical values for AGN jets are B $\sim$5 Gauss and $R_{\text{acc}} \sim 0.01$ pc [33]. Inserting these values in equation 2.14 gives together with equation 2.22 for the maximal neutrino energy:

$$E_{\nu,\text{max}} \simeq 2 \cdot 10^6 \text{ TeV} \tag{2.25}$$

For L_γ we use the measurement of the Mrk 421 flux from [35], i.e. $L_\gamma = 2 \times 10^{-10}$ TeV cm^{-2}s^{-1}. Inserting these values in equation 2.21 yields:

$$E_\nu^2 \frac{dN_\nu}{dE_\nu} \sim 5.8 \times 10^{-9} \text{ GeV cm}^{-2}\text{s}^{-1} \tag{2.26}$$

Obviously this result is based on many simplifications. It is obtained assuming a boost factor of $\Gamma = 1$, whereas $\Gamma \simeq$ several tens seems more favoured [34]. On the other hand, we did not include proton energy losses (i.e. we pretend a 100 % acceleration efficiency) and in this elementary calculation we assume the two simplifications to cancel each other. Another serious simplification is

that we performed all calculations in the Δ-approximation. A substantially more detailed discussion of photo-hadronic interactions which also include inelastic pion production seems to yield rather large differences in for example the ratio of gamma to neutrino luminosities. For power law index photon fields the ratio is found to be rather ~ 1 than the value $\frac{1}{3}$ which is used here [36]. Also, it should be mentioned, that in this model we assume all gammas to actually escape the source and be detected, i.e. no absorption. If absorption takes place, the neutrino flux could be higher.
Figure 2.3 summarises present model calculations for cosmic neutrino point sources. The present calculation is included (denoted *stick figure* model).

2.5 Cosmic neutrinos from beyond the Standard Model

The models described above are examples of *bottom-up* models, in which particles (protons) are accelerated to high energies, causing the subsequent neutrino production.
Artifacts of the Big Bang, such as topological defects or relic particles are alternative candidates believed to be able to produce neutrinos in their decay or annihilation, commonly referred to as *top-down* models. In this section we will give a brief account for the (in our view) most relevant of those models. Completeness is prohibited by the creativeness of theoreticians.

2.5.1 Dark Matter candidates.

Estimates of the energy density of the Universe, especially from measurements of the Cosmic Background Radiation and distant Type 1a supernovae indicate a flat universe with a non vanishing cosmological constant and matter contribution of between 30 and 40 % [42]. The nature of this matter contribution is to a large extent unclear. Calculations of primordial nucleosynthesis in combination with measurements of the abundance of light elements in distant gas clouds, suggest that < 5 % of the matter contribution can be attributed to baryonic (standard model) matter, the rest being of unknown origin. One constraint on this type of matter is that it is not interacting electro-magnetically, i.e. it is not visible by standard astronomical means and its existence could so far only be inferred from its gravitational effects (for example on the rotation curves of galaxies). This is what is generally referred to as the *dark matter problem*.
The prime candidates for dark matter are WIMPs (Weakly Interacting Massive Particles), generally being identified with the lightest (presumably stable) particles arising from super-symmetric theories, believed to be the neutralinos.

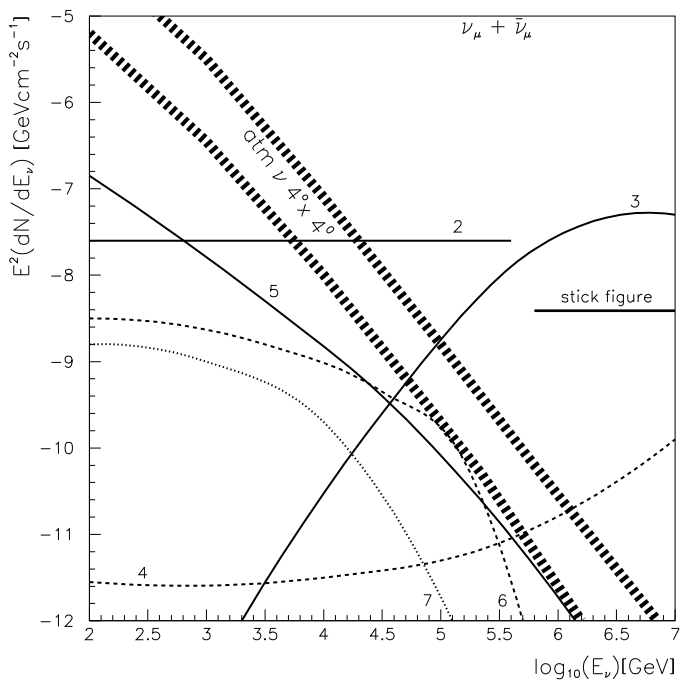

FIGURE 2.3: *Summary of expected $\nu_\mu + \overline{\nu}_\mu$ flux from cosmic sources. 2) AGN core model for 3C 273 [37] for pp interactions, 3) AGN core model for 3C 273 for $p\gamma$ interactions [38], 4) AGN jet model for 3C 273 [39], 5) neutrinos from solar cosmic ray interactions [24], 6) SNR IC444 [40], 7) Cassiopeia A with L_ν=L_γ and E_ν = 0.5 E_γ [41], stick figure denotes the result of the example calculation performed in the present work. Also shown is the horizontal and vertical atmospheric neutrino flux for a 4°$\times$ 4° search bin. Figure adapted from [4]*

Neutralinos have a small probability of scattering off nuclei of ordinary matter. In these scattering processes the neutralino looses energy and will eventually be gravitationally trapped in the potential wells of huge celestial bodies such as the Sun and the Earth. After some time, an equilibrium will be reached between the capture rate and neutralino annihilation rate. Most of the annihilation products will produce neutrinos in hadronisation or decay and these can be detected in neutrino telescopes by searching for an excess of neutrinos in the direction of the celestial body examined. The energy and absolute flux of neutralino induced neutrinos depend on the particular choice of the super-symmetric model and since the non-observation of an excess of neutrinos from the centre of the Earth can be used to put limits on the flux of neutralino-induced neutrinos, part of the tremendous set of possible super-symmetric models have been excluded [13].

2.5.2 Beyond beyond the Standard Model

Even more speculative sources for high energy neutrinos are connected to topological defects which might have been produced in symmetry-breaking phase transitions in the early Universe. These include objects like monopoles, cosmic strings or domain walls. If these defects decay or annihilate they are predicted to emit their energy in form of massive X-quanta which are the quanta of the fields that formed the defect (for example gauge bosons) [43]. These quanta decay and eventually produce neutrinos with energies up to the mass of the X-quantum. These quanta are therefore candidates for the highest energy cosmic rays as well as neutrinos. Predictions by [43] indicate that assuming the mass of the quanta to be $\sim 10^{15}$ GeV the neutrino spectrum might be dominating the atmospheric neutrino spectrum at energies $\gtrsim 10^5$ TeV.

CHAPTER 3

The detection of cosmic neutrinos

3.1 Detection principle

Cosmic neutrinos can not be detected directly. Instead, the aim is to detect charged leptons from the reaction

$$\nu_l + N \rightarrow l + X \tag{3.1}$$

where l denotes charged leptons of any flavor and X represents any hadrons (see figure 3.1 for the corresponding Feynman diagram). A possible neutrino detector will therefore primarily be a detector of charged leptons, in which ways have to be found to ensure that the charged leptons are induced by neutrinos.
The subject of this thesis is the detection of ν_μ induced muons. Already at relatively moderate energies (in the context of cosmic neutrino detection) the track produced by the muon in water/ice detectors has a length which allows efficient reconstruction (see section 3.3 and 6). The muons are furthermore essentially collinear with the incoming neutrino at high energies, the mean deviation given by [29]

$$\sqrt{< \Theta^2_{\nu\mu} >} \sim \sqrt{m_p/E_\nu} \tag{3.2}$$

i.e. less $\sim$ 1.75 degrees for a 1 TeV neutrino. This means that at energies of interest (above $\sim$ TeV, when the atmospheric neutrino background is relatively

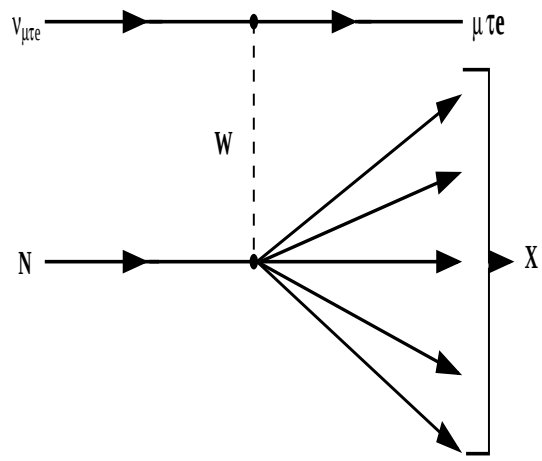

FIGURE 3.1: *Feynman diagram of charged current inelastic νN interaction. The reaction proceeds via $W^{\pm}$ boson exchange.*

low), the muon essentially points back to the source of the neutrino. Signatures of electron neutrinos and neutral-current interactions are subject of dedicated analyses [11][44] and are not further discussed here.
At energies of above $\sim$ PeV [45] the detection of the tau neutrino might become feasible. The tau neutrino exhibits a "double bang" signature with a hadron shower, a tau track and another shower due to the tau decay. To identify the tau lepton, the showers have to be resolved from the track, which probably requires track lengths of hundreds of meters (at PeV the track of a tau is $\sim$ 100 meters long) and thus appropriate detector sizes. This signature is probably beyond the scope of AMANDA, but seems feasible for the next generation neutrino telescope IceCube [46]. Consequently, this signature is not a subject of this thesis.

3.2 Neutrino-nucleon cross section

The charged current νN cross section is given by (e.g. [48])

$$\frac{d\sigma_{CC}}{dxdy} = \sigma_{\circ} \left(\frac{M_W^2}{Q^2 + M_W^2} \right)^2 x\{q + \bar{q}(1 - y^2)\} \tag{3.3}$$

where M_W is the mass of the W boson and q and $\bar{q}$ symbolise the structure functions parameterising the contributions of quark and anti-quarks to the nu-

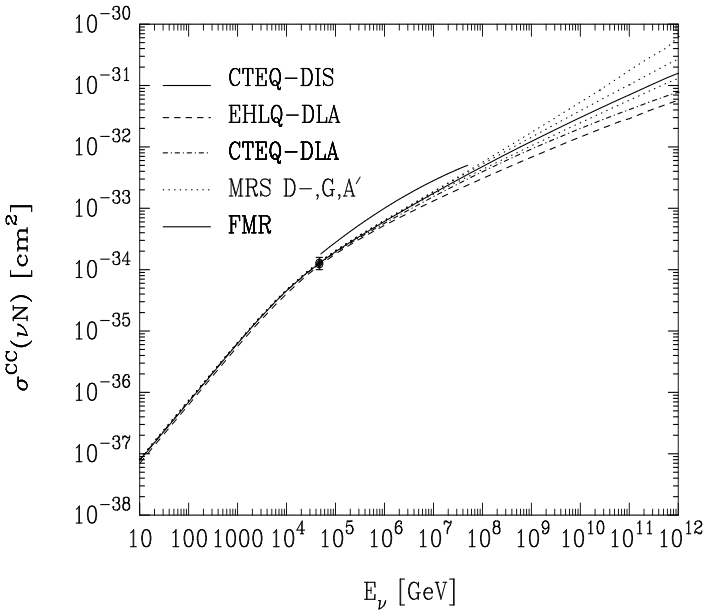

FIGURE 3.2*: Charged current ν N cross section as a function of energy. The different lines indicate different structure functions. The measured point is an average of measurements by H1 and ZEUS at HERA. Figure taken from [47]*

cleon content. x denotes the Bjorken scaling variable, which (assuming the parton model) can be interpreted as the fraction of nucleon momentum carried by the parton. y is the *inelasticity*, which is the fraction of the neutrino energy carried away by the gauge boson. The smaller y, the more energy is transferred to the muon. x and y can be expressed in terms of the square of the four momentum transfer, Q^2, and the energies in the lab system:

$$x = \frac{Q^2}{2M_N(E_\nu - E_\mu)}; \;\; y = 1 - \frac{E_\mu}{E_\nu} \tag{3.4}$$

σ_o is given by

$$\sigma_\circ = \frac{G_F^2 s}{2\pi} = 1.583 \cdot 10^{-38} cm^2 \cdot E_\nu / GeV \tag{3.5}$$

where s is the total centre of mass energy. Figure 3.2 shows the energy dependence of the cross section (from [47]). At low energies ($Q^2 \ll M_W^2$) it grows linearly with E_ν. This behaviour can be understood by noting that valence quark contributions to the structure functions dominate in this regime making the interaction similar to neutrino-lepton interactions (scattering on point like constituents).
Above energies of $\sim$ TeV (with $Q^2_{\text{max}} \approx M_W^2$), the gauge-boson propagator damps the cross section, leading to a less than linear rise. For the purposes of μ detection also the y- dependence on energy has to be taken into account. For energies between TeV and PeV $< y >$ falls off linearly from $\sim$ 0.5 to $\sim$ 0.25 [47], i.e. the fraction of energy transfer to the muon increases leading to a larger range of the muon. The probability for detection depends on a convolution of the cross section and the muon range (see equation 3.13), which means that the slower rise in cross section will be partly compensated by a the larger fraction of energy going to the muon.

3.3 Muon energy loss in matter

3.3.1 Ionisation & radiative loss

The average rate of muon energy loss (or stopping power) can be written as [49]

$$-\frac{dE}{dx} = a(E) + Eb(E) \tag{3.6}$$

Below a critical energy, E_{crit}, $a(E)$ dominates the energy loss. In this regime the main process for loosing energy is due to ionisation and atomic excitation.

Then the stopping power is given by the Bethe-Bloch equation:

$$-\frac{dE}{dx} = Z\frac{K}{A}\frac{1}{\beta^2}\left[\frac{1}{2}\ln\frac{2m_e c^2\beta^2\gamma^2 T_{\text{max}}}{I^2} - \beta^2 - \frac{\delta}{2}\right] \tag{3.7}$$

where we refer to table 3.1 for a definition of the parameters and to [50] for a detailed discussion of the equation. $b(E)$ parametrises the contributions

Parameter	Definition
c, β, γ	usual relativistic factors
N_a	Avogadro's number
m_e,r_e	electron mass and classical radius
K/A	$4\pi N_A/Ar_e m_e c^2$ = 0.307 MeV g^{-1} cm^2 for A = 1 g mol^{-1}
I	mean excitation energy
T_{max}	maximum energy transfer per collision
Z	atomic number of absorber
A	atomic mass of absorber in g mol^{-1}
δ	density effect correction

TABLE 3.1: *The parameters of the Bethe-Bloch equation*

of photo-nuclear and radiative processes such as e$^+$e$^-$ pair production and bremsstrahlung (and a small contribution of Čerenkov radiation, see below), which will start to dominate the energy loss above E_{crit}. At the muon energies of interest in AMANDA ($E_\mu > 100$ GeV) the functions $a(E)$ and $b(E)$ can safely be considered constant. In ice the values of a and b are: $a \simeq 0.2$ GeV/m and $b \simeq 3.4{\cdot}10^{-4}$ m^{-1} [51]. Then the critical energy where radiative losses dominate the ionisation losses is given by $E_{\text{crit}} = a/b \simeq 600$ GeV. Figure 3.3 illustrates the behaviour of the stopping power as a function of muon energy.
In equation 3.7 we find the *density correction term*, δ. This term introduces a correction for the fact that the atoms in a dense medium will react coherently to the incident particle, i.e. in calculating the energy loss of a charged particle to the electric field of an atom in a medium we have to include the effect of the macroscopic polarisation of the medium (for a detailed discussion see [50]). Integrating equation 3.6 yields the range of a muon as a function of energy:

$$R_\mu(E) \sim \frac{1}{b} ln\left(\frac{E}{E_{\text{crit}}} + 1\right) \tag{3.8}$$

again assuming a and b to be constant. Thus, we see that the muon range scales linearly with energy for $E \ll E_{\text{crit}}$ and logarithmically for larger energies.

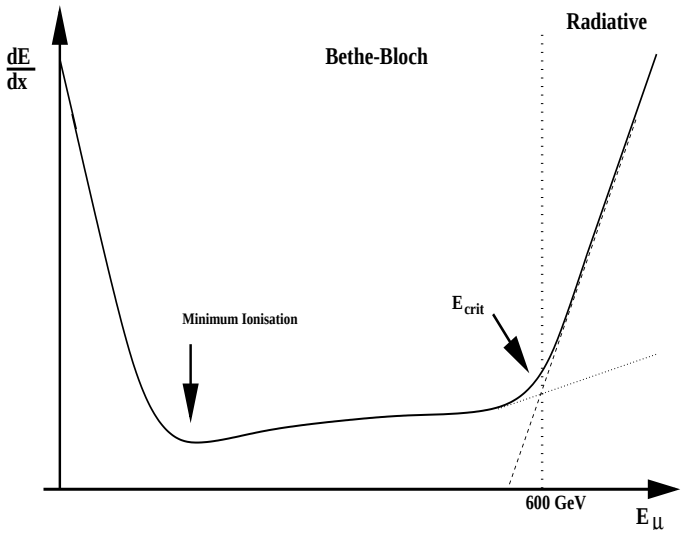

FIGURE 3.3*: The qualitative behaviour of the stopping power for muons in ice.*

3.3.2 Čerenkov radiation.

Čerenkov radiation is a kind of radiative energy loss which (since it is of the order of 2 MeV/m) is negligible for discussions of the stopping power for muons. However, since it is the process which is utilised in AMANDA to detect muons (as we will see in the section 3.5), Čerenkov radiation deserves special attention.

Čerenkov radiation has a physical origin similar to the density correction term appearing in the Bethe-Bloch formula: the atoms which interact with the incident particle get polarised, and subsequently depolarise resulting in a electromagnetic wave. The propagation velocity of this wave will be equal to the speed of light in the medium. If the particle moves faster than this speed, constructive interference will be possible, otherwise the radiation is exponentially decaying. Thus, the condition for observing Čerenkov radiation is given by $\beta > \frac{1}{n(\lambda)}$, or

$$E_{\text{thr}}(\lambda) = \frac{m_{\text{particle}}}{\sqrt{1-(1/n(\lambda))^2}} \tag{3.9}$$

which using a refraction index in ice of n = 1.33 (corresponding to the wavelengths where the photo-detectors are most sensitive, i.e. 300-600 nm, see chapter 4 and [51]) and inserting the mass of the muon (105 MeV) gives an

threshold E^{μ}_{thr} = 160 MeV.
Čerenkov radiation is emitted at a characteristic angle :

$$\cos\theta_C = \frac{1}{\beta n(\lambda)} \tag{3.10}$$

In the case of highly relativistic muons β is very close to unity and n is nearly constant in the wavelength window of interest. We obtain

$$\theta_C = \text{const} = 41^\circ \tag{3.11}$$

The number of photons per unit length emitted in Čerenkov radiation is given by [50]:

$$\frac{d^2N}{d\lambda\, dx} = \frac{2\pi\alpha}{\lambda^2} \cdot \left(1 - \frac{1}{\beta^2 n(\lambda)^2}\right) \tag{3.12}$$

Again assuming the refractive index of ice in the appropriate wavelength range, n = 1.33, and inserting 3.10 in 3.12 we arrive at $\sim$ 300 photons/cm expected from Čerenkov radiation.
Figure 3.4 illustrates the production of Čerenkov radiation and its use for muon detection.

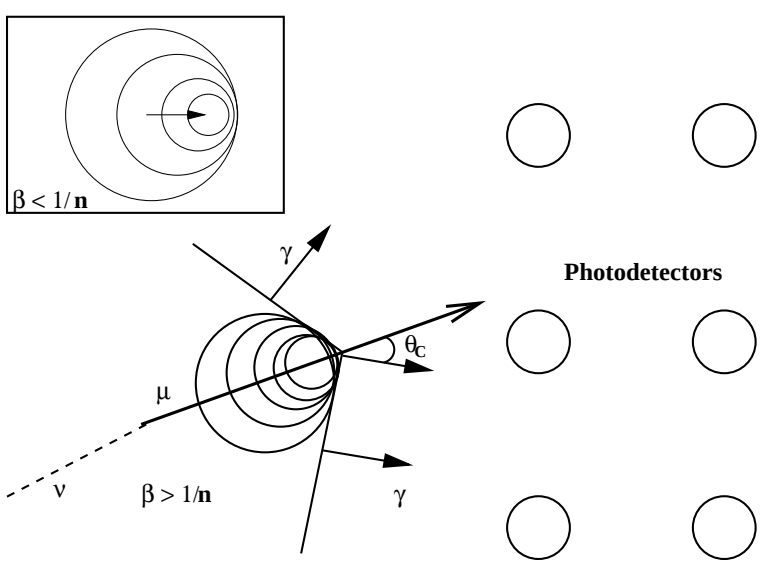

FIGURE 3.4: *Schematics of the detection of muon tracks by Čerenkov radiation. The inlet shows the case for a "slow" particle, where the Čerenkov condition is not fulfilled*

3.4 Signal and background

Figure 3.5 summarises the different sources of muons detected in neutrino telescopes. The vast majority of muons are produced by cosmic ray interaction in the atmosphere (called atmospheric muons). It is impossible to distinguish muons originating from proton interactions from those originating from neutrino interactions, unless a way is found to veto proton induced muons. The main idea of neutrino telescopes is to use the Earth as a filter, stopping all particles other than neutrinos. Thus, "signal" consists of "up-going"(with respect to the Earth's surface) muons. Obviously, to make use of this fact, one needs to be able to reconstruct the direction of the muons. Locating the detector deep underground (or under-ice as in the case of AMANDA) facilitates this task by reducing the downward-going muon background significantly. For AMANDA located 1500 meter deep in ice, for example, the atmospheric muon background is reduced by about 3 orders of magnitude as compared to a detector located at surface [52]. Still, even at a depth of $\sim$ 1500 meters, the ratio between down-going and up-going muons is roughly 10^6. This implies an obvious risk for mis-reconstructions. For example, even after a first (admittedly simple) reconstruction and an exclusion of all tracks being reconstructed from $< 10^\circ$ degrees above the horizon this ratio is still about 10^4.
The mis-reconstructed atmospheric muons thus constitute the largest contribution to the background for the detection of cosmic neutrinos. It should be noted that to some extent all sources of neutrino-induced muons (discussed in chapter 2) except for cosmic point sources constitute a further background to the present analysis. However, since point sources are identified by a clustering over a homogeneous background (determined by data), the exact composition of this background is of secondary interest (see chapter 5)

3.5 Detector size and target medium

A rough estimate of the required size of the detector can be obtained by estimating the rate of muons induced by cosmic neutrino point sources as a function of target area of the detector.
In order for a neutrino to be detected, it must produce a muon with a range sufficient to reach the detector. The detection probability depends therefore on the physics of the neutrino interaction producing the muon and the muon propagation. It is approximately given by:

$$P_{\nu\to\mu} \simeq n\sigma_\nu \, \overline{R_\mu} \tag{3.13}$$

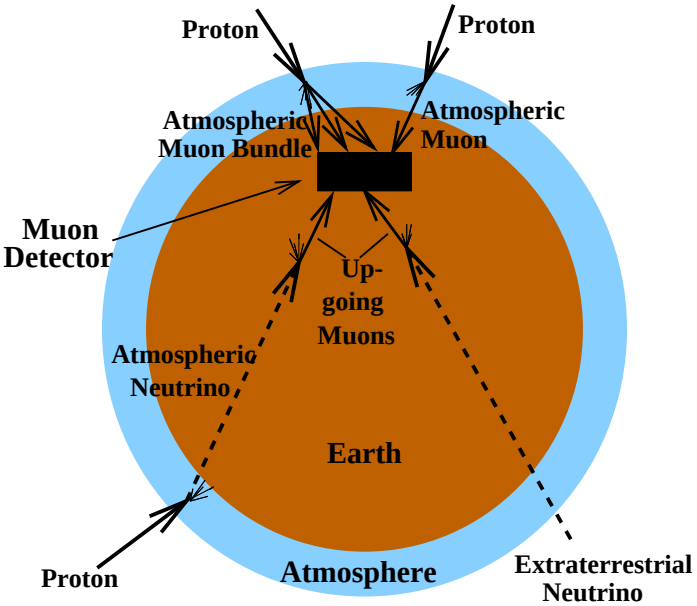

FIGURE 3.5: *Signal and background in a neutrino detector. The majority of triggers are muons produced in the atmosphere by cosmic ray interactions. Neutrino-induced muons are identified by their direction (coming from the directions pointing inside the Earth). Point sources of extraterrestrial neutrinos are the scope of this thesis.*

where n is the number density of particles in the target medium. For energies between 1 TeV $\leq E_\nu \leq$ 1 PeV , $P_{\nu\to\mu}$ can be approximated by [17]:

$$P_{\nu\to\mu} \sim 5 \times 10^{-9} \left(\frac{E_\nu}{\text{GeV}}\right)^{0.8} \tag{3.14}$$

As discussed in chapter 2 (see equation 2.26) we expect a flux of order of $E^2\Phi_\nu(E_\nu) \sim 10^{-7}$ GeV cm^{-2} sr^{-1} [1]. The expected rate of muons is given by convolving the flux with the probability of detection:

$$f_\mu = \int_{10^6\text{GeV}}^{10^9\text{GeV}} dE_\nu\, \Phi(E_\nu) P_{\nu\to\mu}(E_\nu) \tag{3.15}$$

where the integration boundaries are chosen to cover the range in which neutrinos are predicted by the "stick figure" example calculation. Inserting equation 3.14 and the flux prediction into 3.15 leads to an estimate of the rate of muons induced by a neutrino flux as given in equation 2.26:

$$f_\mu \sim 150\ [\text{km}^{-2}\text{sr}^{-1}\text{yr}^{-1}] \tag{3.16}$$

Equation 3.16 indicates that in order to detect reasonable count rates of cosmic neutrino induced muons, neutrino telescopes have to be sensitive to areas of $\mathcal{O}$(km^2).

This fact leaves detection of Čerenkov radiation in a naturally available transparent medium as the only feasible technique for detecting muons for the simple reason that other alternatives would be far too expensive. A key point is that standard Photo Multiplier Tubes (PMT) can detect single photons and measure arrival times with $\sim$ ns accuracy over distances which are limited by the attenuation length in the target medium. A relatively small number of PMTs can therefore be used to cover large target areas and the measured arrival times of photons can be used to reconstruct muon directions.

Large volumes of transparent media are provided by ice, ocean and lake water, with different advantages and disadvantages. AMANDA has chosen ice, whereas the neutrino telescope ANTARES [53] has chosen the Mediterranean sea and the BAIKAL neutrino telescope [6], Lake Baikal in Siberia. The Antarctic ice is extremely pure with absorption length of 90 -100 meters as compared to $\sim$ 50 m in sea water and $\sim$ 20-30 m in Lake Baikal [54]. The

[1] in equation 2.26 we calculated the flux of a point source. Like other authors [33] we assume here 100 of those sources per steradian to convert the point source flux to a diffuse flux.

situation considering scattering is reversed. An important parameter is the effective scattering length, defined as:

$$\lambda_{\text{eff}} = \frac{\lambda_{\text{scatt}}}{1- < \cos\Theta_{\text{scatt}} >} \tag{3.17}$$

which gives the characteristic length for scattering out of the direct light path (i.e. scattering in near forward direction is neglected). The effective scattering length for ice is $\sim$ 20 -30 m, whereas it is about 2000 m in oceans and $\sim$ 380 m in Lake Baikal which gives an advantage in angular resolution to the water sites [54][55]. Obviously, except for the optical properties, there are other factors which should be taken into account when choosing the site. For example, one major drawback of the ocean/lake sites is the presence of environmental noise due to radioactive potassium and bioluminescence. In ice the environmental noise is negligible.
The number of PMTs and the distance between them is dictated by financial constraints. In the best of all worlds, one would instrument an as large a volume as possible with an as dense grid of PMTs as possible. Assuming a fixed number of PMTs, the energy threshold decreases and the detection efficiency increases with PMT density but the sensitive area decreases. The optimal choice thus depends on the main goal of the experiment. For example, for cosmic neutrinos a large detection area is more important than a low energy threshold (where the atmospheric neutrino background dominates anyway). The reader is referred to [56] for a more detailed discussion.

Summary The presence and abundance of atmospheric muons requires a detector for cosmic neutrinos to be build deep under surface. Furthermore, the detector should give the possibility to reconstruct the direction of the muons. The expected fluxes and cross sections as well as the range of muon indicates that $\mathcal{O}(\text{km})^2$ target areas are appropriate to detect cosmic neutrinos. This leads to the choice of Čerenkov photon detection by PMT in a transparent medium as the detection technique. Reconstructing the direction of the incident muon will then be possible by measuring the arrival times of photons on different PMTs distributed in that medium. The natural target media are ice and ocean/lake water. Equipping a large volume of ice or ocean/lake water with a grid of photo multiplier tubes is thus the experimental strategy for detecting cosmic neutrinos.

CHAPTER 4

The AMANDA neutrino telescope

The Antarctic Muon and Neutrino Detector Array (AMANDA) [7],[57] is a neutrino telescope situated at the geographic South Pole. It consists of a three dimensional grid of photo detectors which are situated on strings of combined signal/high voltage cable. These strings are lowered into holes drilled into the antarctic ice sheet by a hot water drill. The construction of AMANDA started in 1993 with the deployment of 80 photo detectors (and instrumented volume of 500000 m^3) and has reached its present configuration ($\sim$ 680 photo detectors and an instrumented volume of about 1.5 $\cdot 10^7$ m^3)[1] in 2000. At present the AMANDA collaboration consists of about 100 physicists from 21 research labs and universities from Europe and the USA. In this section, the relevant parts of the detector will be presented.

4.1 Optical modules and the detector geometry

Figure 4.1 shows a schematic view of the AMANDA detector as it is operated since 2000. AMANDA consists of a cylindrical array of photon detectors with (in the present configuration) a diameter of $\sim$ 200 m and a height of $\sim$ 500 m. The photo detectors - called Optical Modules (OM) - consist of photo multiplier tubes (PMT) situated in a glass pressure vessel (see figure 4.1 for a cross section of an OM). The PMT (Hamamatsu R5912-02) has a diameter of $\sim$ 20

[1] for a neutrino telescope an increase in instrumented volume of factor $\sim$ 30 does not mean an increase in detection capability of factor 30. The volume in which for example muons can be detected is proportional to the range of the muon, thus energy dependent.

cm and consists of 14 dynodes, an anode and a photo-cathode, which is sensitive to photons between 300 nm and 650 nm with a peak quantum efficiency of 23 % at 420 nm. The timing resolution of the PMT is $\sim$ 3 ns FWHM. The pressure vessel is roughly 30 cm in diameter and can withstand pressures of $\sim$ 660 atm. Its glass has a 90 % transmissivity for $\lambda > 400$ nm, but has a cut off at $\sim$ 300 nm. Optical contact between the sphere and the glass cover of the photocatode of the PMT is established using silicon gel. The output of the PMT is transmitted to the data acquisition at surface via co-axial or twisted pair cables which also supply the high voltage (HV) for the dynode chain of the PMTs (via a HV divider).

As mentioned previously, the geometry of the array evolved with time. In 1994 the first four strings equipped with in total 80 photo detectors were deployed in the ice cap at a depth between 800 and 1000 meters (AMANDA-A array). At these depths, air bubbles which are trapped during formation of the south pole glacial ice, lead to a scattering length $\sim$ 25 cm [58], which makes the reconstruction of muon tracks unfeasible. At larger depth, these bubbles disappear [59],[60], which in 1995-1996 lead to the deployment of four additional strings with 80 OMs at a depth between 1500 and 2000 m (the AMANDA-B4 array). With this array, the first neutrino candidates were detected [51]. Six strings were added in the following year, forming the AMANDA-B10 array, consisting of in total 302 optical modules.

In 2000, AMANDA reached its present configuration with 19 strings and 677 photo detectors. Three strings were deployed in 1997/1998 at a depth between 1150 and 2350 m to assess ice properties below and above the B10 array. The final six strings were deployed in 1999/2000, five of which at depth between 1500 m and 2000 m, the sixth, due to problems during deployment, at a depth between 1000 m and 1500 m. The data analysed in this thesis was taken with the AMANDA-B10 configuration in 1999.

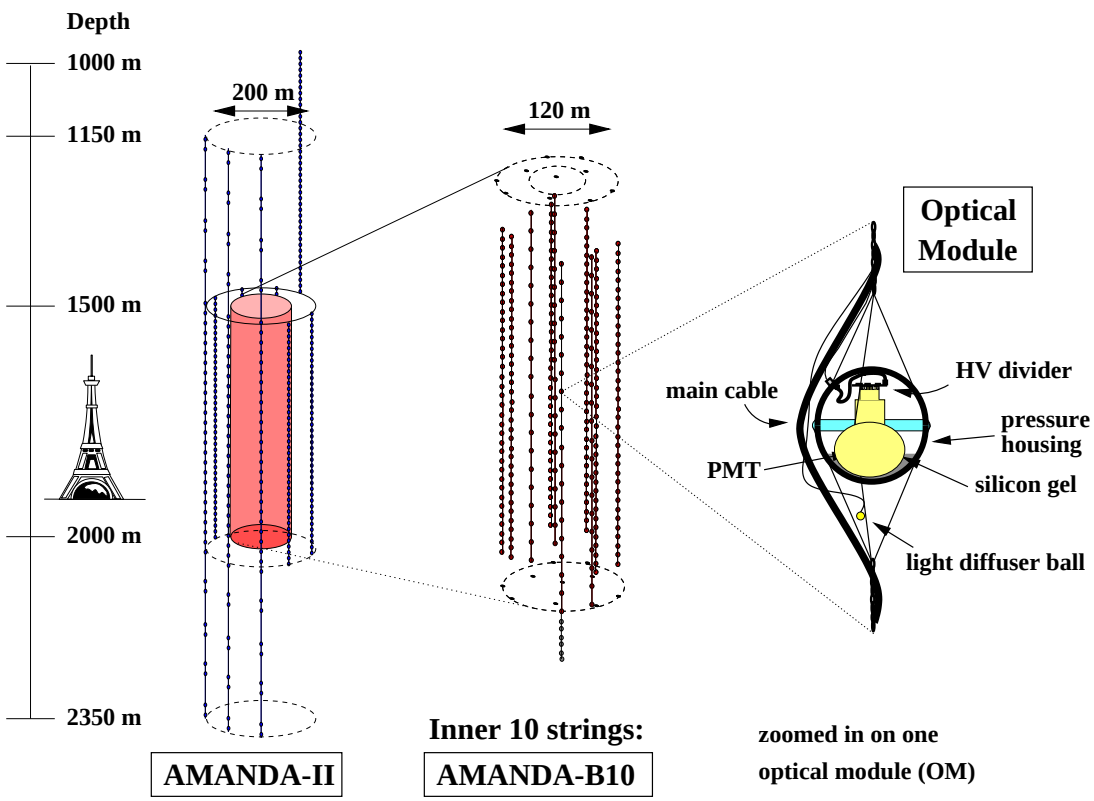

FIGURE 4.1: *The AMANDA detector. In the middle a zoom of the AMANDA-B10 array which was the detector configuration used in the present analysis. The Eiffel tower is included for comparison.*

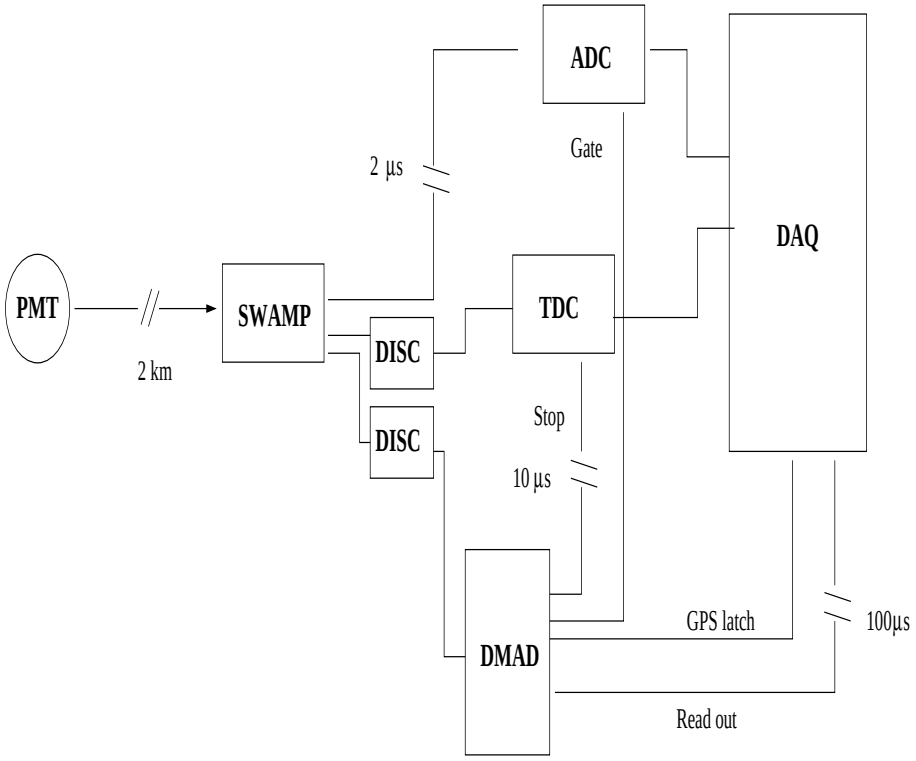

FIGURE 4.2: *Schematic view of the AMANDA-B10 electronics relevant to the present analysis*

4.2 Trigger system and data acquisition.

Figure 4.2 shows a schematic view of the trigger system and the data aquisition of AMANDA-B10. The electrical signal transmitted by the PMT is both attenuated (from amplitude $\mathcal{O}$(V) to $\mathcal{O}$(mV)) and smeared out (from a few nanoseconds to hundreds of nanoseconds) by the $\sim$ 2 km long cable [2]. Due to the attenuation, the signals have to be amplified before entering the discriminators and trigger logic. This is done by the SWAMP (SWedish AMPlifier) modules.

The smearing of the pulse leads to the merging of several single photo-electron pulses into one pulse . The time of a pulse is therefore determined by recording the leading edge and trailing edge by a Time to Digital Converter (TDC), which receives its input from a discriminator connected to the SWAMPs. The TDC is buffered such that it records upto 8 leading and 8 trailing edges per OM in 32 μs time window. The second output of the SWAMPs goes, via a 2 μs delay to peak-sensing Analog to Digital Converter (ADC). The delay is necessary to account for the time it takes to form the trigger, since in contrast to the TDC the ADC are not buffered. The third output of the SWAMPs is fed to a discriminator whose output is fed into the DMAD board (Digital Multiplicity Adder) [61], which performs the trigger logic. The trigger requirement in 1999 was on the number of hits in a predefined time window (a majority trigger). This logic is established by the DMAD by first converting the pulses from the discriminator to a standard pulse, whose length is defined by the preset trigger time window. The standard pulses are then added and if they cross the required threshold a trigger is issued. The DMAD then sends a stop signal to the TDC after an additional 10 μs delay, opens the ADC gate and latches an absolute time stamp (GPS). Furthermore the trigger signal initiates the DAQ read-out of the ADC and TDC values (after an additional delay of 100 μs), which are consequently written to mass storage.

In 1999 the majority trigger was set to 18 hit OMs within about[3] 2.2 μs. Since a typical muon event last for $\sim$ 5 μs, the time structure of an event thus consists of the trigger at 22 μs (the 32 μs buffer of the TDC minus the 10 μs delay) with 2.2 μs of event after and before the trigger time, plus $\sim$ 7.5 μs after-pulsing and $\sim$ 20 μs random noise before the event.

A lower bound on the majority requirement is given by the need for suppress-

[2] as mentioned before two types of cables have been used: co-axial cables for the four strings deployed in 1995/96 and twisted pair cables for the six strings deployed in 1997/1998. Co-ax cables produces more dispersion ($\sim$ 400 ns) than twisted pair ($\sim$ 100 ns)

[3] depending slightly on OM

ing uncorrelated noise hits, mainly originating from radioactive contamination of the glass in the OMs pressure vessel and from thermal noise, typically leading to noise rate (per OM) of $\sim$ 400 Hz (Strings 1 -4) and $\sim$ 1.5 kHz (strings 5-10). Below a majority requirement of about 10, events are strongly noise dominated. Above that the live-time of AMANDA-B10 is correlated linearly with the trigger threshold ranging between $\sim$ 75 % (at threshold 10) and $\sim$ 100 % (at threshold around 30). The position of the trigger requirement is thus given by the trade off between the reduction in live-time and the decrease in energy threshold. A rough estimate gives an energy threshold for muons of about 50 GeV (assuming a muon track of length about 200 m is necessary to give 18 hits).

With the increased detector size of AMANDA-II, the wish for large lifetime leads to a more stringent multiplicity requirement ($\sim$ 24). Since low energy (short track) muons are suppressed by a too high majority requirement, an additional trigger is tested since 2000, which requires a string-wise coincidence of n hits within a window of m modules (so called correlation trigger).

CHAPTER 5

Analysis

Buta beszéd !
Cicu

5.1 Introduction

In this section, a search for continuous emission of neutrinos from specific directions in the northern hemisphere is described. The analysis technique is to identify a hypothesised point source by a statistically significant excess of events over a background which is determined by an average over all off-source bins with equal sensitivity, in practise bins in the same zenith band.
The signal of this search is assumed to have a E^{-2} spectrum of high energy neutrinos concentrated in one point on the sky. The background on the other hand consists of the diffuse flux of atmospheric neutrinos and the misreconstructed atmospheric muons. Optimisation will therefore be on reconstruction quality (atmospheric muons vs. neutrino induced muons), search bin size and angular resolution (point-source flux vs. diffuse flux) and energy (softer atmospheric neutrino spectrum vs. harder cosmic neutrino spectrum).

Of course, knowing potential sources might influence the analysis. To avoid any bias by the experimentalist's prejudice the analysis is therefore initially performed blindly. Blindness is provided by randomising the event times, i.e. the right ascension coordinate. The analysis is then completed on the randomised sample and it is only after having finalised the choice of cut variables and cut values as well as the analysis strategy, that the correct right ascension coordinates are reinstalled.

5.2 The analysed datasets

5.2.1 Experimental data

The data analysed in this thesis was taken by the AMANDA-B10 detector between February 1999 and November 1999. During 1999 the AMANDA detector consisted of 13 strings. However, three outer strings were used for detector studies and thus excluded from subsequent analysis. The detector therefore effectively had 10 strings and 302 optical modules. The effective live-time of the detector was 223.63 days (see section 5.4.1.1). The detector triggered a readout when at least 18 hits were recorded within 2.5 μs. A total number of 1.3 $\times 10^9$ triggers were recorded. The preprocessing to level 2 (see section 5.4) reduced this amount to $\sim$ 1.3 $\times 10^6$ events. The full analysis presented here reduces the amount of data to 642 events (i.e. rejection of data on a level $\sim 10^6$). A summary of the full processing chain can be found in table 5.2.

5.2.2 Monte Carlo simulation

For signal simulation, the neutrino generator *NUSIM* [62] was used. *NUSIM* generates neutrinos and propagates them through the Earth (assuming the standard Earth model [63]) and simulates the neutrino-nucleon interaction in the ice or rock (applying the MRS [64] structure function) including the hadronic shower. *NUSIM* applies importance sampling. Therefore it simulates an E^{-1} spectrum, which is reweighted to the assumed E^{-2} dependency for point sources in the subsequent analysis. Neutrinos were simulated in an energy range between 10 GeV and 10^8 GeV and in a zenith angle range between $80°$ and $180°$ degrees. In total $\sim$ 1.3 $\times 10^6$ neutrinos and anti-neutrinos were simulated.
As a check of the reliability of the signal simulation, atmospheric muons (the dominant background) were simulated using *CORSIKA* [65], which generates a cosmic ray spectrum and simulates the interactions in the atmosphere and subsequent production of secondaries (in our case, we are particularly interested in the muons). In this analysis, $3 \cdot 10^6$ primary cosmic rays have been simulated with an $\mathrm{E}^{-2.67}$ spectrum in an energy range between $\sim 10^{\ 3}$ GeV and 10^9 GeV. This results in $\sim 10^5$ muon triggers. The muons produced in the neutrino or cosmic ray interaction were propagated through the ice using the MMC propagator [66]. The muon energy loss simulation includes decay, ionisation, bremsstrahlung as well as photo-nuclear processes and δ electron production in ice.
The scattering of photons within the fiducial volume of AMANDA is simulated using *PTD* [67]. For muons, the photons originating from Čherenkov

radiation are generated and then scattered according to a given ice model (see section 5.3.3). The result is a table containing the number of photons in the time interval $t, t+\delta t$ at any space point (x,y,z) detected with an OM with orientation (θ, ϕ). Once the detector response simulation has generated the position of a muon track, the number of photo-electrons detected with any OM and the arrival times can be directly read out from these tables.
The last step in the simulation chain is the simulation of the detector response. This is provided by the software package *AMASIM* [68], which simulates the photons generated and all hardware components of the AMANDA detector.

5.3 Calibration

5.3.1 Time

The electrical signal transmitted by the PMT is both attenuated (from amplitude $\mathcal{O}$(V) to $\mathcal{O}$(mV)) and smeared out from $\mathcal{O}$(ns) to $\mathcal{O}$(100 ns) by the $\sim$ 2 km long cable. Due to the smearing, the leading edge time recorded by the DAQ will not be the one measured in the ice and furthermore dependent on the amplitude of the pulse, since the time-stamp registered by the DAQ is taken when the pulse traverses the discriminator threshold. The relation between the time in the ice, t_{OM}, and the time on tape, t_{LE}, can be parametrised as:

$$t_{OM} = t_{LE} - T_{\circ} - \frac{\alpha}{\sqrt{A}} \tag{5.1}$$

where the amplitude, A, is measured in mV and $T_{\circ}$ and α are OM dependent calibration constants. To determine the calibrations constants, a laser source on the surface is used, whose light is guided in an optical fiber to the OM and there diffused by a diffuser ball. This method of calibration requires the measurement of the absolute time of the laser pulse (given by splitting the pulse), the time it takes for the photon to travel from the diffuser ball to the PMT (given by the distance of the diffuser ball to the PMT times the speed of light in ice) and the pulse travel time through the optical fiber. The measurement of the pulse travel time through the optical fiber is done prior to the actual time calibration by measuring the arrival time of the fraction of the pulse which is reflected at the end of the optical fiber.

5.3.2 Geometry

The relative position of OMs in the ice is determined by in-ice light sources, in particular LED and lasers. From the known speed of light in the ice, the

relative position of the OM can be obtained by triangulation. With this method an accuracy of position measurement is ≤ 50 cm [69].

5.3.3 Optical properties of the ice

The optical properties of the ice can be determined by calibration light sources and down-going muons.
Scattering and absorption of photons at various wavelength is measured using in -situ light sources which are located at different places in the array [60]. Arrival time distributions are measured and compared with Monte Carlo distributions characterised by the absorption and scattering coefficients, which thereby can be determined as a function of depth or as function of wavelength. Figure 5.1 shows a measurement of the scattering coefficient done using light sources with different wavelengths. Peaks are clearly visible in the scattering coefficient which are attributed to dust layers at those depths. The rapid rise in the scattering length at depth $<$ 1400 m is assumed to be due to air bubbles in the ice. For absorption the corresponding plot looks essentially flat, since at this wavelength the absorption in the ice dominates the absorption due to dust [60].
An additional source of scattering are air bubbles which are generated around the OM during the re-freezing of the drill hole [1]. The time distributions are essentially unaffected by these bubbles [70], but they influence the angular response of the OM (we will return to this point in section 6.5).

Implementation of the optical properties of the ice The modelling of the ice structures in AMANDA introduces a systematic uncertainty (see section 6.5). The photon scattering and absorption is simulated using PTD (see section 5.2). To implement the ice model in PTD certain approximations are necessary. The actual ice structure measured is divided into layers of homogeneous ice, such that each OM is only seeing a sheet of ice with homogeneous ice properties and different OMs see different ice. A given photon consequently propagates through homogeneous ice only and does not see different ice properties. Furthermore, the wavelength dependent scattering is approximated by (an empirically inferred factor times) its value at λ = 532 nm. In one implementation (which we will call *Fundamental Ice Model (FIM)* for future reference) also the wavelength dependency of the absorption length has been approximated by a constant related to its value at λ = 532 nm. The FIM model is consequently

[1] not to be confused with the air bubbles which are present naturally at shallower depth in the ice cap

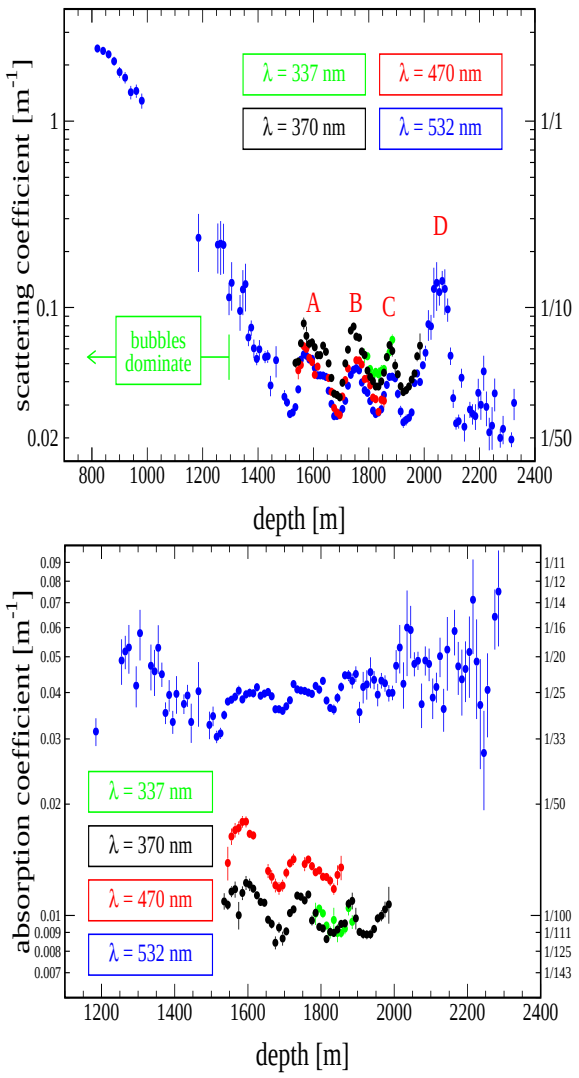

FIGURE 5.1: *Scattering (upper panel) and absorption (lower panel) of photons with different wavelength as a function of depth. At shallow depth the ice air bubbles increase the scattering. Figure taken from [60]*

based on the accurately ($\sim$ 10 %) known ice properties. However the approximations lead to a discrepancy in (amongst others) the multiplicity distribution for downgoing muons. This is due to a larger number of late photons in the simulation than in the data, which indicates that the absorption has been underestimated. It has therefore been decided to adjust the absorption length such as to fit the observed photon distributions. The newly found absorption length is then used for the implementation of the ice model in PTD. After this procedure, the comparison between data and background simulation shows good agreement, see e.g. [71]. For future reference this model will be called the *Modified Absorption Model (MAM)*.
A new implementation of the ice properties into the simulation of photon propagation is under way. This implementation will make use of the the full wavelength dependency of the scattering and propagate photons through different ice layers. However, for the study presented in this thesis, this simulation was not available.
We will return to a discussion of the differences in ice model implementation in section 6.5.

5.4 Data cleaning

5.4.1 Removing noisy OMs and unstable data taking periods

Since the data taking period starting January 2000, a monitoring system [72] is operational based on the ROOT data analysis framework [73]. For each file and run[2] during the data taking period different parameters of the detector (such as ADC/TDC rates, noise rates, trigger rates and time difference distributions) are recorded and subjected to a first statistical analysis. The information is summarised run-wise and then monitored continuously by collaboration members. For the data taken in 1999 this type of data stream has been produced off-line (posterior to the actual data taking) and provides a data base for the selection of noisy OMs and unstable data taking periods. The selection is here performed on noise rate exclusively, since this has the strongest effect on the reconstruction result. In a first step, the noise rate distribution of each OM for each run is fitted with a Gaussian. The result of this fit is then used to classify OMs according to the following criteria:

[2] a standard run is 24 hours long, but shorter run times are possible if interruptions occur and runs have to be started manually.

- an OM is classified as bad for the whole data taking period if it has a deviation $> 5\sigma$ from its own or the global mean in > 50 % of all runs
- an OM is classified as bad for a given run, if it has a deviation $> 10\sigma$ from its own or the global mean in this run.
- a run is classified as bad, if either 50 % of all OMs exhibit a $> 5\sigma$ deviation of the noise rate or 20 % of all OMs a $> 10\sigma$ deviation.

OMs and runs classified as bad are then removed from the subsequent analysis. Figure 5.2 shows the noise rates as a function of run number for four different OMs, two of which have been excluded. As mentioned in section 4.2, noise rates for OMs on string 1 to 4 are $\sim$ 400 Hz, whereas they are $\sim$ 1500 Hz for strings 5 -10, which has to be taken into account in the analysis described above.

5.4.1.1 Calculating the effective live-time

Having removed bad data taking periods and OMs, the effective live-time (wall-clock time minus dead time) can be estimated. For this purpose, again the files produced as part of the AMANDA monitoring system have been utilised. For each file the time-difference distributions were fit with an exponential $\exp \Delta t/\tau$, from which the true rate of events can be calculated as:

$$R_{\text{true}} = \frac{1}{\tau} \tag{5.2}$$

The raw rate (i.e. the one including the dead-time) can be calculated by dividing number of events in each file by the time span of the file, t_{file}. The effective live-time for the whole data taking period can then be estimated by:

$$t_{\text{eff}}(1999) = \sum_{\text{file}|\text{good runs}} t_{\text{file}} \times \frac{R^{\text{file}}_{\text{raw}}}{R^{\text{file}}_{\text{true}}} \tag{5.3}$$

For the present analysis the live-time was calculated to be 223.63 days.

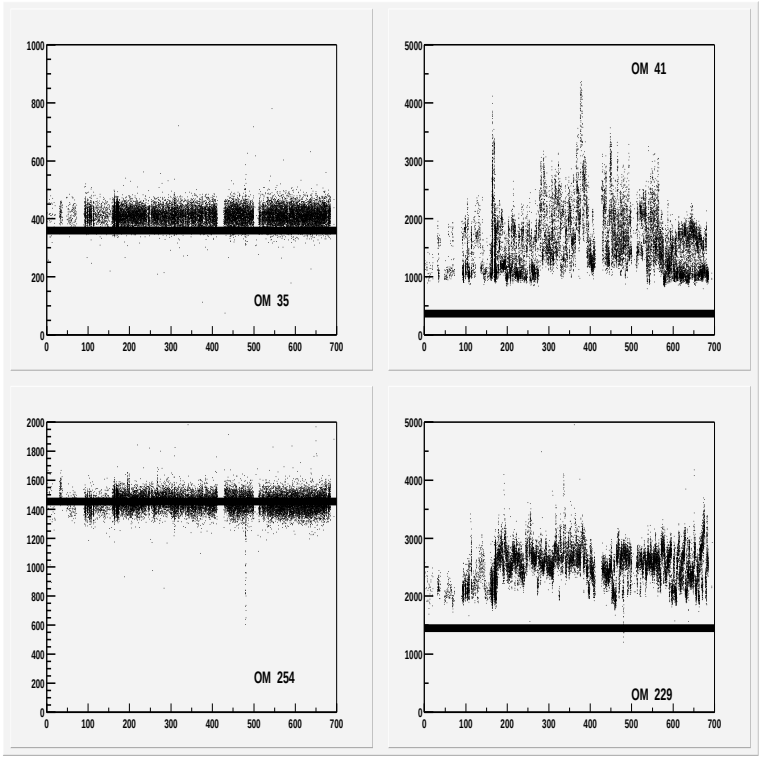

FIGURE 5.2: *Noise rate as a function of run number for four different OMs. The solid line gives the global average for this type of OM. The OMs on the left side are included in the analysis, the OMs on the right side excluded.*

5.4.2 Removing non-physical hits

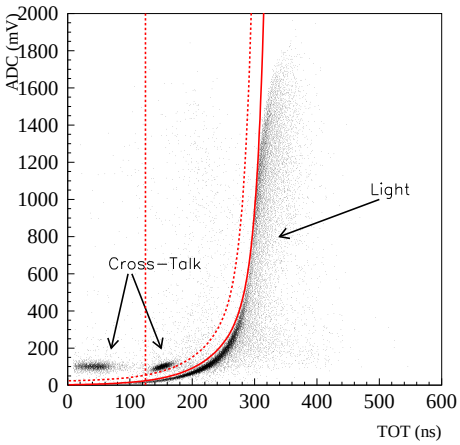

FIGURE 5.3: *The ADC as a function of TOT for OM 149. The correlation for physical hits and those from cross talk are indicated. The straight dashed line indicates the standard time-over-threshold cut. Figure from [44]*

As described in the previous section, in a first step, very noisy OMs and data taking periods have been removed. However, even the average "good" OM exhibits a noise rate, i.e. hits which are not useful for the reconstruction. To be able to exclude those hits several additional requirements have been imposed on each event. First of all, only hits within a certain time window (4500 ns) are accepted, which are most likely to belong to the physical event. Furthermore the calibrated amplitude of the hit is required to be between 0.3 and 1000 photo electrons and the time-over-threshold (TOT) between 125 and 2000 ns. An isolation criterion is imposed excluding all hits which do not have at least 1 neighbouring hit within 500 ns not further than 70 meters away. Another especially disturbing class of hits is due to electronic cross talk, i.e. electromagnetic coupling between different cables. Cross talk in AMANDA occurs exclusively between OMs on the same strings and can be explained by the way cables are wrapped together [74]. The time-over-threshold cut ($>$ 125 ns) already reduces a significant amount of these electronically induced hits, but a more efficient algorithm has been devised [75], which makes use of the fact that hits due physical events exhibit a distinctive correlation between the time-over-threshold value and the ADC value, see figure 5.3, and furthermore uses maps of the cross talk in the detector obtained from the timing calibration data.

5.5 Reconstruction

The reconstruction algorithm used in AMANDA is a maximum likelihood method to find the track matching the light pattern in the detector in an optimal way. There are different flavours of this reconstruction algorithm, de-

pending on what track hypothesis and what track parameters are sought to be reconstructed. Though normally interested in a distinct set of parameters of the track (in our case primarily the direction) performing different types of reconstruction can provide information on for example the quality of the reconstruction, which is why different variants are commonly performed on the same event.
For a detailed discussion the reader is referred to [76]. Here the emphasis will be on the basic ideas and on the variants of the reconstruction which have been used in the analysis.
The experimental data contains times of the leading edges, time-over-thresholds and peak amplitudes of the pulses for each event and each OM signal. The reconstructions utilised in the present analysis make use only of the timing information. For a given set of hits in the array and for a given hypothesis one calculates the likelihood:

$$\mathcal{L} = \prod_i p_i(t_{\text{res},i}, OM_i|H_j) \tag{5.4}$$

where the product runs over all OM with a hit and H_j is a tested track hypothesis. $t_{\text{res},i}$ is given by:

$$t_{\text{res},i} = t_{\text{hit},i} - \left[T_\circ + \frac{d}{\sin\Theta_C \cdot c_{\text{ice}}}\right] \tag{5.5}$$

with $T_\circ$ being the calibration constant (introduced in section 5.3), d the distance from the hypothetical track to the OM, Θ_C the Čerenkov angle and c_{ice} the speed of light in ice. The second term on the right side is the expected arrival time for an unscattered Čerenkov photon. In this analysis the track is characterised by its coordinates, three spatial coordinates (x,y,z) (= $\vec{r}_\circ$) and two angles (ϕ,θ), i.e. our assumption is that all light patterns are produced by single muons (not bundles) without stochastic energy losses (regardless of energy). Reconstructions with other sets of free parameters (like for example the energy) and also other types of signatures (cascades from NC interactions and CC electron and τ neutrinos) are possible [76] [77]. However, they have not been used in this work.
The best fit to the light pattern is determined by minimising $-\log\mathcal{L}$ with respect to the parameters of the track. Each term in equation 5.4 is the probability for an OM to observe a hit with t_{res} given by equation 5.5 assuming a test hypothesis, H. This probability depends on both the timing properties of the OM and - more strongly - the scattering in the ice. While in the detector simulation

(see section 5.2), the timing distribution of each OM is produced by propagating photons in ice with a MC method [67], for calculational reasons in the reconstruction analytic functions are used which are obtained from fits to the MC distributions [78]. For minimisation the Powell's algorithm is used [79] in this analysis. Other minimisation algorithms (simplex, simulated annealing [79] or MINUIT [80]) are optional.

First guess Simple approximations to the light pattern seen in an event serve as first guess for the subsequent minimisation. The first guess used in this analysis is the *line fit*. Here, the positions and times are assumed to be linearly related:

$$\vec{r}_i = \vec{r}_\circ + t_i \vec{v} \tag{5.6}$$

and a χ^2 is calculated:

$$\chi^2 = \sum_{i=1}^{N_{\text{hits}}} (\vec{r}_i - \vec{r}_\circ - \vec{v} \cdot t_i) \tag{5.7}$$

with $\vec{r}_\circ$ and $\vec{v}$ as free parameters. Minimisation of the χ^2 can be performed analytically and consequently yields a vertex position $\vec{r}_\circ$, a direction $\vec{n} = \vec{v}/|\vec{v}|$ (given in terms of θ and ϕ angle) and the length of the vector $\vec{v}$. In the present analysis, the direction is used as a first filter against down-going muons.
Other initial guess methods have been developed for special purposes like the reconstruction of cascade like events or the rejection of coincident muons. Also the line-fit has been replaced recently with a more efficient method ("direct walk"), which however was not available for this analysis. Since we do not use those methods in the present analysis, the reader is referred to [76] for a detailed discussion.

Iterative reconstruction. To avoid finding a local minimum instead of the global one an iterative scheme is used, i.e. several reconstructions of the same type are done on the same event, each starting with a different initial track. Following a first iteration, a new initial track is found by randomly choosing ϕ and θ, and moving the position vector $\vec{r}_\circ$ on the new track to the point closest to the centre of gravity of hits (defined as $\sum_{i=1}^{N_{\text{OM}}} \vec{r}_i$). Then a new minimisation is performed. The likelihood of the newly found minimum is evaluated and compared to the likelihood for the track found by the previous iteration. If the new likelihood is smaller, the new track becomes the reference for the next iteration. The iteration is performed for a user-defined number of times - here 16.

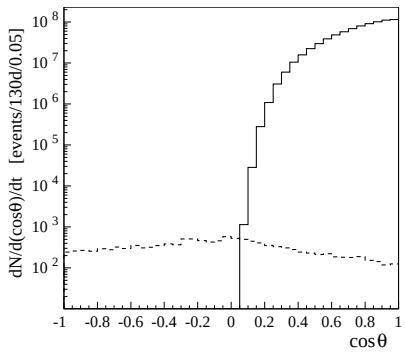

FIGURE 5.4: *Distributions of events in AMANDA as a function of the zenith angles, atmospheric muons constitute the overwhelming majority (solid line). Also shown are atmospheric neutrinos (dashed line). Figure from [8].*

Bayesian reconstruction Maximising the likelihood gives us the hypothesis which has the highest probability to produce the observed hit pattern. This statement should not be confused with a statement about the probability for H given the observed times t_{res}, i.e. $P(H, t_{\text{res}})$. These two probabilities are connected via Bayes' theorem:

$$P(H, t_{\text{res}}) \propto P(t_{\text{res}}, H) \cdot P(H) \tag{5.8}$$

$P(H)$ is the *a priori* probability of the hypothesis. This observation lead to the development of a reconstruction algorithm based on $P(H, t_{\text{res}})$ instead of $P(t_{\text{res}}, H)$, the *Bayesian (zenith weighted) reconstruction* [81]. In AMANDA cosmic muons provide the vast majority of triggers (see figure 5.4). The zenith distribution of atmospheric muons therefore constitutes a good approximation to the prior function. In practise, the zenith distribution of muons is simulated by Monte Carlo and then parametrised by a polynomial. This parametrisation is then implemented in the likelihood reconstruction as an additional (zenith dependent) weight. With this assumptions the reconstruction can be performed using $P(H, t_{\text{res}})$.
In contrast to the likelihood reconstruction, the track parameters found by the zenith weighted reconstruction are not used in the present analysis. Instead, the calculated likelihood for the zenith weighted reconstruction is used as a quality parameter. As will be described in section 5.6.2, this quality parameter yields good separation between signal and background.

Parabola fit The Parabola fit does not constitute a separate reconstruction in the sense that a new track is calculated. Instead, it re-evaluates the result of a previous reconstruction by fitting a two dimensional parabola to the likelihood function. Results of this parabola fit provide new quality parameters, mainly correlated to the track resolution. In the present case, the parabola fit was performed on the track results of the iterative reconstruction. See below for a description of the resulting quality parameters.

5.6 Separation of signal from background

In this section we will describe the method for separating signal from background employed in the present analysis. As mentioned previously, the signal will be assumed to be neutrinos originating from point sources with an energy spectrum $\propto E^{-2}$. The background consists mainly of atmospheric muons but also any component of diffuse flux of neutrino induced muons. Somewhat counter-intuitively, we will consider the data to be our background. This is legitimate since the expected contamination by signal is (optimistically) negligibly small. Using data is beneficial by not having to rely on the accuracy of the background simulation and not being limited by the background simulation statistics.

5.6.1 Variable selection

The point source search has been iterated a few times during the existence of AMANDA [82][83][84] . Many variables which provide good signal efficiency and background rejection efficiency have been identified. In this work we choose to quantify a given variable's quality for background/signal distinction by calculating the "overlap-integral":

$$\mathcal{I} = \sum_{\text{nbins}} f_{\text{sig}}(v)\, f_{\text{bg}}(v) \tag{5.9}$$

where f_{sig} and f_{bg} are the signal and background distributions, where both distributions are normalised to have integral equal one. Inspired from quantum mechanics, the overlap integral gives the integrated probability of both variables having values in the same region. This means, the smaller the overlap integral, the better the separation between background and signal. Figure 5.5 illustrates the concept.

We then chose each cut variable according to following criteria:

- physics motivation (such as correlation with resolution or energy)
- a small value of the overlap integral
- small correlation with the already chosen variables

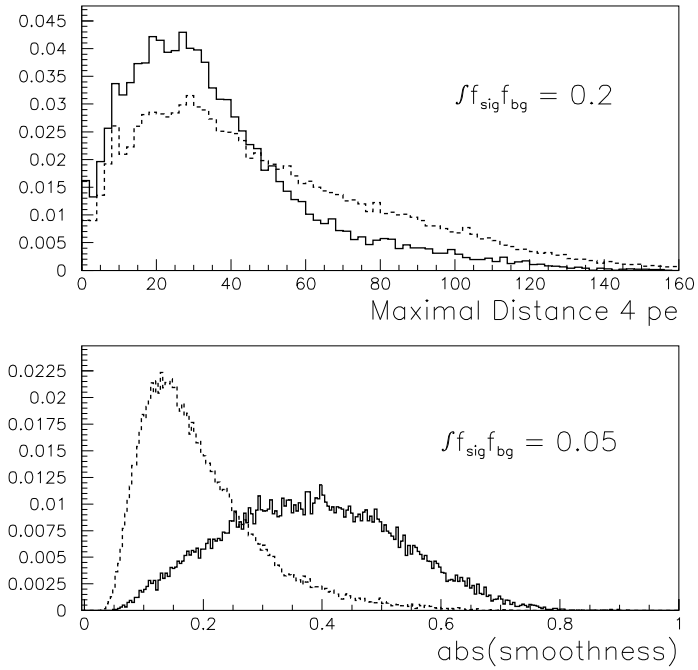

FIGURE 5.5*: Illustration of the overlap integral. Upper Panel: the maximal distance of $>$ 4 photo-electron hit to the track, lower panel: the absolute value of the smoothness (see section 5.6.2). The solid line is the signal distribution. The difference in overlap integral is a factor 4. The smoothness variable has been used in the analysis.*

5.6.2 Description of cut variables

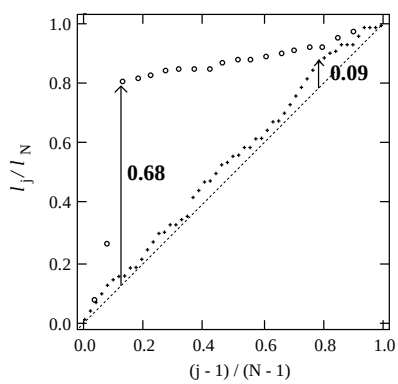

FIGURE 5.6*: Illustration of calculation of smoothness. An event with clustered hits gives a large value of the smoothness, a high quality track-like event a small value. Figure taken from [8]*

Smoothness The likelihood reconstruction does not take into account correlations between hits. Thus, tracks with clusters of hits at one end and those with smoothly distributed hits along the track may obtain equal likelihood despite the fact that the latter is more likely to be a well reconstructed event. This observation lead to the invention of the *smoothness* parameter [85]. The value of the smoothness parameter S is the Kolmogorov-Smirnov test statistic calculated for the observed hit pattern and the hypothesis of constant light emission:

$$S = \max(S_j), S_j = \frac{j-1}{N-1} - \frac{l_j}{l_N} \tag{5.10}$$

here l_j is the distance along the track between the points of closest approach to the first and j^{th} hit OM. Figure 5.6 illustrates the calculation of the smoothness parameter.

The distribution of the smoothness parameter for well reconstructed events will in general be narrower than the corresponding distribution for background events. The above described definition of smoothness considers the distribution of hits along the track which is defined by the first and last hit. In the present analysis two different variants of S have been used. S_{mrl}, where the track is considered between the first hit and the last possible track point within the detector ("maximum reasonable length") and S_{phit}, which is defined as:

$$S_{\text{phit}} = \max\left(\frac{\sum_{i=1}^{j}\Theta_i}{\sum_{i=1}^{N}\Theta_i} - \frac{\sum_{i=1}^{j}P_i^{\text{hit}}}{\sum_{i=1}^{N}P_i^{\text{hit}}}\right) \tag{5.11}$$

Here N is the number of all operational OMs, and $\Theta_i = 1$, if the OM had a hit, 0 otherwise. The hit probabilities P^{hit} are calculated as in the reconstruction. Both variables are presented in figure 5.7. S_{mrl} is used as an initial cut parameter to reduce the data set to an amount manageable for the multivariate

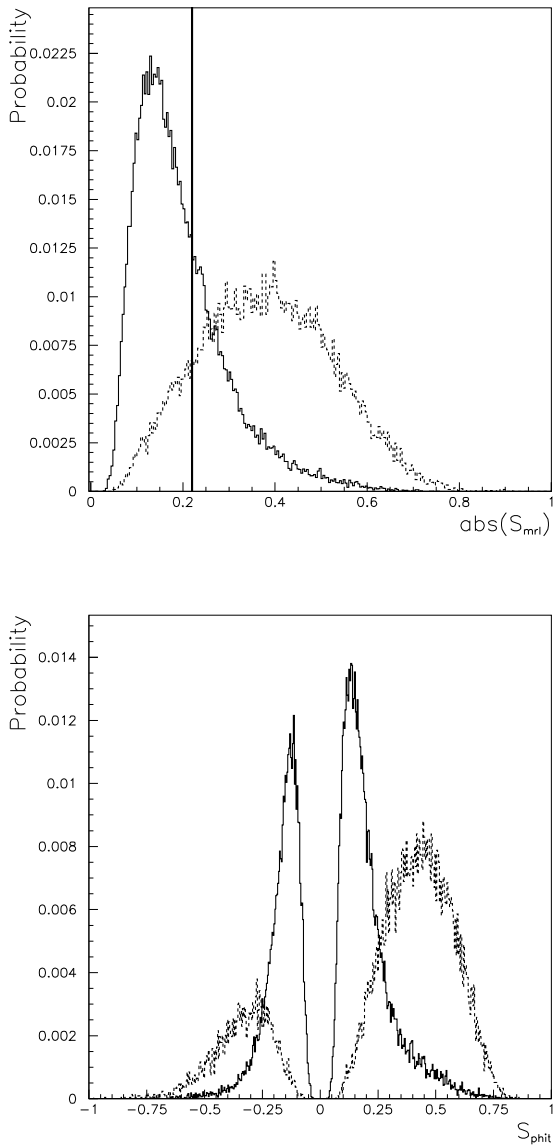

FIGURE 5.7*: The smoothness parameters (definition see text) used in this analysis. The solid line is the signal distribution, dashed is background. A cut has been applied to S_{mrl} at the value indicated by the straight solid line. S_{phit} has been used as input variable for a multivariate method (the Support Vector Machine, see section 5.6.3).*

method we are using to reduce the sample to the final level (the Support Vector Machine, see section 5.6.3). S_{phit} has been used later in the analysis as an input variable to this multivariate method.

Hit probability Another cut variable is formed by summing all hit probabilities for the OMs which had a hit. A bad reconstruction will reveal a track with respect to which the probabilities for the OMs to have a hit are smaller than for a well reconstructed track. Therefore this variable will obtain smaller values for mis-reconstructed tracks than for the well reconstructed. Since the summed probability is proportional to the number of OM with a hit, this variable is also correlated with the muons energy. Figure 5.8 shows the distributions for this parameter for signal and background. The hit probability is used as an input parameter to the Support Vector Machine.

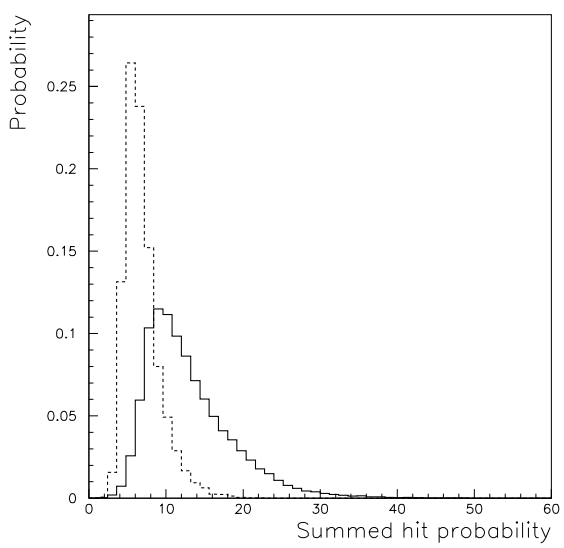

FIGURE 5.8*: The summed hit probability for all OMs which had a hit. The solid line is the signal distribution, dashed denotes the background.*

Likelihood parameter difference As mentioned previously, a series of reconstructions is applied to each event. Each fit returns the *likelihood parame-*

ter:

$$L_{\text{fit}} = -\log \mathcal{L} \tag{5.12}$$

Comparisons between likelihood parameters of different fits can provide useful variables for distinction between signal and background. In the present analysis, the difference of likelihood parameter returned by the Bayesian and the likelihood parameter returned by the iterative fit was found to be particularly useful. The Bayesian fit was hereby performed, such that the algorithm was forced to return a downward-going fit. Especially for relatively vertical signal, the iterative fit returns a rather large likelihood (small likelihood parameter), whereas the zenith-restricted Bayesian fit returns a comparably low likelihood (large likelihood parameter). For data, both fits give a relatively low likelihood irrespective of zenith angle. The result is a variable which gives comparatively good separation for zenith angles $\theta > 100°$, see figure 5.9.

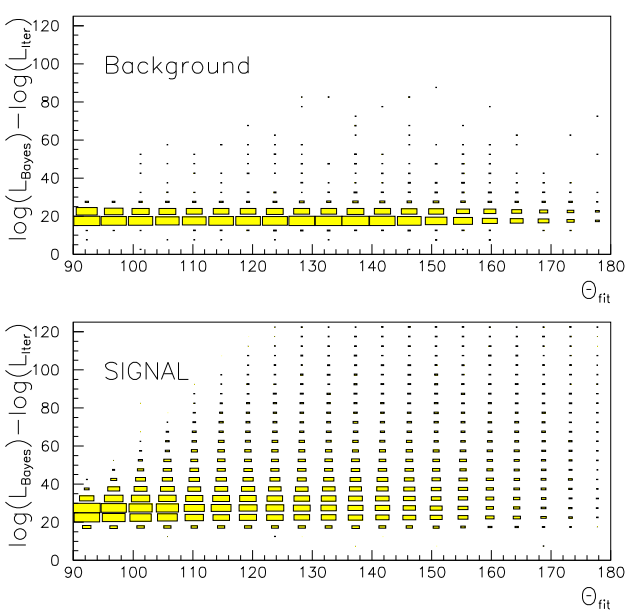

FIGURE 5.9*: The difference of the likelihood parameter for the Bayesian reconstruction and the iterative reconstruction as a function of zenith angle. Signal and background show good separation for $\theta >\sim 100°$*

Track resolution Instead of relying on Monte Carlo simulations for finding the angular resolution of the detector, [86] implemented a method which provides a resolution on track by track basis. From the calculated likelihood function a track resolution can be obtained from fitting a parabola to the likelihood around the minimum. In case of a Gaussian shaped likelihood, the resolution σ is obtained from finding the points in hypothesis space (θ,ϕ) where $\Delta \log \mathcal{L} = \frac{1}{2}$. For the Gaussian assumption, it holds $\sigma = \sigma_{\Delta\theta} = \Delta\theta(\Delta \log \mathcal{L} = \frac{1}{2})$ (and for ϕ correspondingly). Though, in general, $\sigma \neq \sigma_{\Delta\theta}$ in case of non-Gaussian likelihood function, this variable still provides a good handle on separating signal from background, see figure 5.10. Well reconstructed tracks have a narrower likelihood function and consequently a smaller $\sigma_{\Delta\theta,\Delta\phi}$. In the present analysis, both $\sigma_{\Delta\theta}$ and $\sigma_{\Delta\phi}$ are used as input variables for the Support Vector Machine. Furthermore, prior to the SVM, events with $\sigma_{\Delta\theta,\Delta\phi} < 0$ have been removed, since negative values of these quantities indicate pathological likelihood functions and consequently mis-reconstructed events.

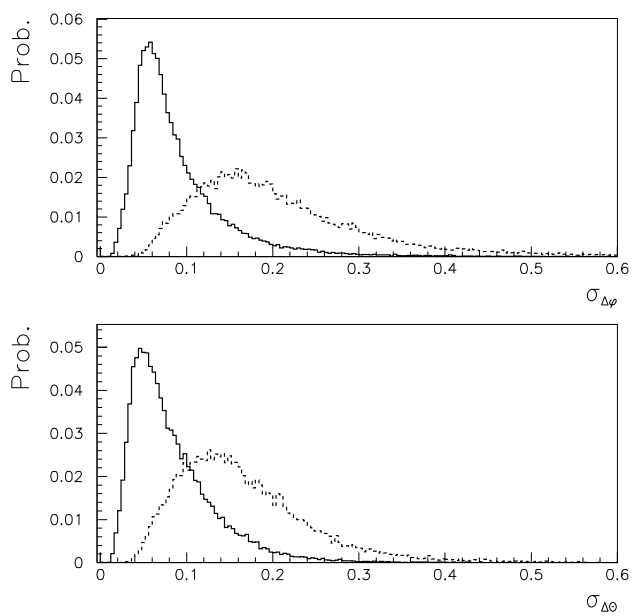

FIGURE 5.10*: The parameters $\sigma_{\Delta\theta}$ and $\sigma_{\Delta\phi}$ obtained from a parabola fit applied to the likelihood function. Solid line is signal, dashed line is background.*

5.6.2.1 Comparison with background simulation

While very important for the analyses where the background estimate relies on simulation prediction, the comparison of the data distributions with the background simulation is of limited interest for the point source search, since the background is estimated from the data itself. We use here the comparison merely as a cross check for the signal simulation. A large discrepancy between simulated atmospheric muons and data would indicate problems in the detector simulation. Figure 5.11 compares the distributions of the data and background simulation for the variables which have been used in the SVM. The distributions are in good or very good agreement.

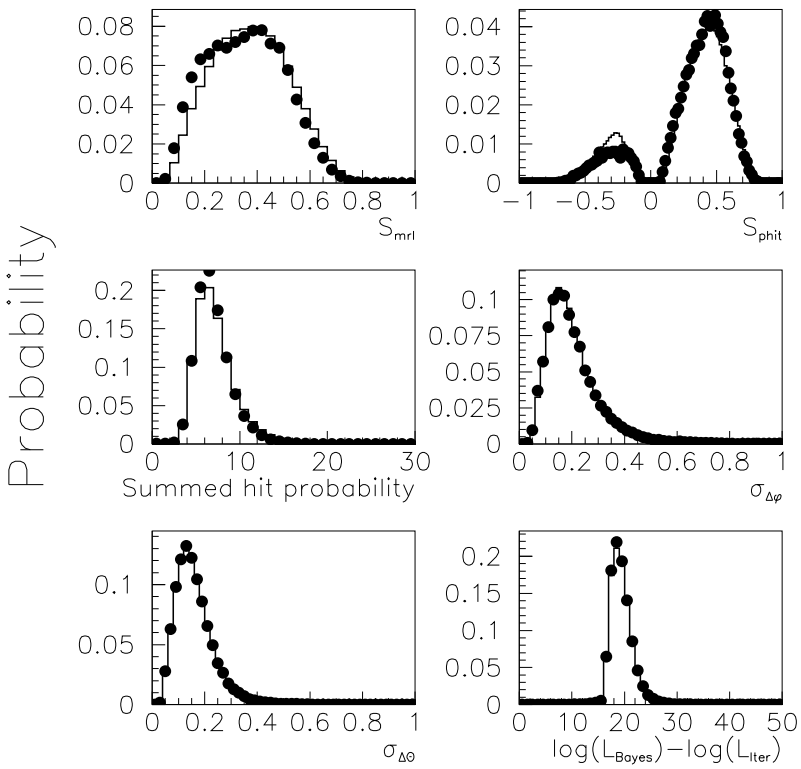

FIGURE 5.11: *Comparison of the variables used in the present analysis with a background simulation. Dots are the simulation, solid lines the data*

5.6.3 Support Vector Machines: Theory

Support Vector Machines (SVM) is a relatively new multivariate analysis method which in its present form has been developed in the beginning of the 90s at AT&T Bell Laboratories for applications in optical character recognition and time series prediction (see [87] and references therein). For particle physics applications it has only recently been discovered, see for example [88]. In this section, a brief introduction to the methodology of the SVM will be given, the reader is referred to [87] and [89] for more detailed introductions.

5.6.3.1 Hyperplane classifiers

Hyperplane classifiers deal with the task to find the function that maps the input parameter space into some classification space. Consider a set of training events $(x_1, y_1), ..., (x_l, y_l) \subset \Lambda \times \mathbb{R}$, where Λ symbolises the space of input parameters ($x_i \in \Lambda$) and $\mathbb{R}$ denotes the target value space ($y_i \in \mathbb{R}$). Commonly it would be $\Lambda = \mathbb{R}^n$ (where n is the number of variables used) and the function to find would be:

$$f : \mathbb{R}^n \rightarrow \mathbb{R} \tag{5.13}$$

One way to construct this function is to find hyperplanes separating the classes. To simplify the discussion, we start by considering the linear case, where a hyperplane will be given by:

$$f(\mathbf{x}) = \mathbf{w} \cdot \mathbf{x} + b \tag{5.14}$$

$\mathbf{w} \in \Lambda$ and $b \in \mathbb{R}$ in equation 5.14 are the parameters which determine the hyperplane. Figure 5.12 illustrates the problem for a one-dimensional input space. Finding the hyperplane is a minimisation problem, in which we require f to be as *flat* as possible, and at the same time to deviate from the training data target values by at most ϵ. The flatness requirement implies the greatest possible margin between the two classes (figure 5.12 illustrates that fact). Flatness can be defined differently, here it is defined by the euclidean norm of $\mathbf{w}$, $\|\mathbf{w}\|^2$. The task is consequently to minimise $\|\mathbf{w}\|^2$ subject to constraints:

$$-\epsilon < (\mathbf{w} \cdot \mathbf{x_i} + b) - y_i \tag{5.15}$$

$$(\mathbf{w} \cdot \mathbf{x_i} + b) - y_i \leq \epsilon \tag{5.16}$$

To find an hyperplane fulfilling the above conditions might not be feasible, therefore one allow for errors (one defines a “soft margin”), which however, is

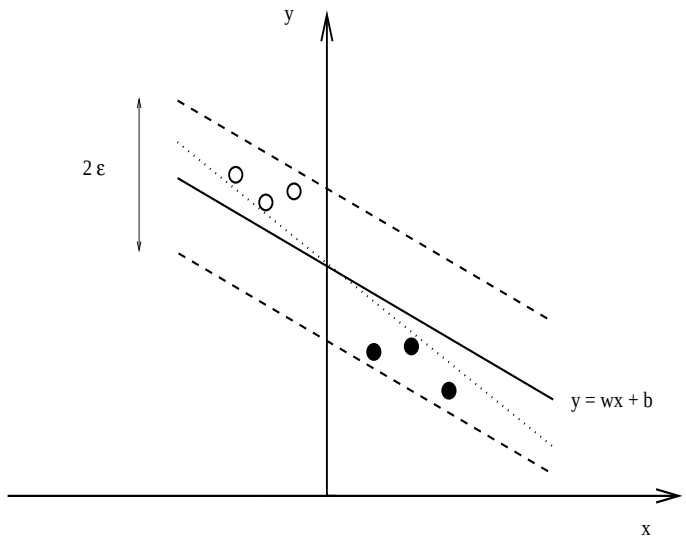

FIGURE 5.12: *Illustration of a hyperplane classifier for one dimensional input data. The optimal hyperplane is given by the one with the smallest slope (flattest), which implies largest possible separation.*

penalised in the minimisation process by the parameter C. More formally, one minimises:

$$\frac{1}{2}\|\mathbf{w}\|^2 + C\sum_{i=1}^{l}\xi_i \tag{5.17}$$

and relaxes at the same time the constraints (equation 5.16) to fulfill the condition $\leq \epsilon + \xi_i$. The ξ_i are a function of ϵ:

$$|\xi_i| := \begin{cases} 0 & \text{if } |\xi| \leq \epsilon \\ |\xi| - \epsilon & \text{otherwise} \end{cases} \tag{5.18}$$

and the constant C quantifies the penalty on the miss-classification.
The method to solve this minimisation problem chosen in the SVM case is to construct a Lagrange function, which includes both the function to minimise and the constraints. This is not only a convenient way to solve a minimisation problem in presence of constraints but in addition will be the key ingredient to generalise the SVM to the non-linear case (see below). The way to introduce constraints into Lagrange function is by using *Lagrange multipliers*, see e.g.

[90]. The corresponding Lagrange function will be:

$$\mathcal{L} = \frac{1}{2}\|\mathbf{w}\|^2 + C\sum_{i=1}^{l}\xi_i - \sum_{i=1}^{l}\alpha_i(\epsilon + \xi_i - y_i + \mathbf{w}\cdot\mathbf{x_i} + b) \\ - \sum_{i=1}^{l}\alpha_i'(\epsilon + \xi_i + y_i - \mathbf{w}\cdot\mathbf{x_i} - b) \tag{5.19}$$

Where we have introduced the Lagrangian multipliers α, α' corresponding to the two boundary conditions. The Lagrangian multipliers are sometimes called *dual variables*.

5.6.3.2 Support vectors and the dual optimisation problem

The task is thus to find the stationary points of $\mathcal{L}$ with respect to $\mathbf{w}$,b, ξ. This means all partial derivatives $\partial_{\mathbf{w},b,\xi}\mathcal{L}$ have to vanish separately. In particular:

$$\partial_{\mathbf{w}}\mathcal{L} = \mathbf{w} - \sum_{i=1}^{l}(\alpha_i - \alpha_i')\,\mathbf{x_i} = 0 \tag{5.20}$$

Thus, $\mathbf{w} = \sum_{i=1}^{l}(\alpha_i - \alpha_i')\,\mathbf{x_i}$ and

$$f(\mathbf{x}) = \sum_{i=1}^{l}(\alpha_i - \alpha_i')\mathbf{x_i}\cdot\mathbf{x} + b \tag{5.21}$$

We see, that the $\mathbf{w}$ can be expanded in linear combinations of the training patterns. The subset of those with non-vanishing α_i are called *Support Vectors*. The relations resulting from the requirement $\partial_{(\mathbf{w},b,\xi)}\mathcal{L} = 0$ can be substituted into equation 5.19, yielding a function with only the Lagrange multipliers as free parameters. The new Lagrange function becomes

$$\mathcal{L} = -\frac{1}{2}\sum_{i=1,j=1}^{l}(\alpha_i - \alpha_i')(\alpha_j - \alpha_j')\mathbf{x_i}\cdot\mathbf{x_j} \\ -\epsilon\sum_{i=1}^{l}(\alpha_i + \alpha_i') + \sum_{i=1}^{l}(\alpha_i - \alpha_i')y_i \tag{5.22}$$

The optimisation task is now to maximise $\mathcal{L}$ with respect to the Lagrangian multipliers. This is sometimes called the *dual optimisation problem* [89].

5.6.3.3 Generalisation to the non-linear case

One way of linearising a problem, is to preprocess the data via a non-linear map. Consider the following example (see [87] and references therein) . Assume a map from $\Phi : \mathbb{R}^2 \rightarrow \mathbb{R}^3$, given by:

$$\Phi(\mathbf{x}) = (x_1^2, \sqrt{2}x_1x_2, x_2^2) \tag{5.23}$$

In the *feature space*, $\mathbb{R}^3$, a linear SVM can be used and reveals a quadratic function in $\mathbb{R}^2$. Preprocessing works in this particular case, but becomes increasingly unhandable for higher polynomials [87]. Noting that for the above example:

$$< \Phi(\mathbf{x}), \Phi(\mathbf{x}') >=< (x_1^2, \sqrt{2}x_1x_2, x_2^2), (x_1'^2, \sqrt{2}x_1'x_2', x_2'^2) >=< \mathbf{x}, \mathbf{x}' >^2 \tag{5.24}$$

where we denote the dot product by $< .. >$, hints towards a solution of the problem: The scalar product of the mapped vectors can be expressed as function of the scalar product of the unmapped vectors.
In the previous section we reformulated the optimisation problem in terms of dual variables. This lead to an expression only involving scalar products of the vectors. As indicated by equation 5.24, in this case, the map Φ does not have to be found explicitly, instead it is sufficient to know the function:

$$\kappa(\mathbf{x}, \mathbf{x}') =< \Phi(\mathbf{x}), \Phi(\mathbf{x}') > \tag{5.25}$$

κ denotes a class of functions, so called *kernel functions*, which correspond to dot products in the feature space. The optimisation problem can then be rewritten as:

$$\begin{aligned}\mathcal{L} = -\frac{1}{2} \sum_{i=1,j=1}^{l} (\alpha_i - \alpha_i')(\alpha_j - \alpha_j')\kappa(\mathbf{x_i}, \mathbf{x_j}) \\ -\epsilon \sum_{i=1}^{l} (\alpha_i + \alpha_i') + \sum_{i=1}^{l} (\alpha_i - \alpha_i')y_i\end{aligned} \tag{5.26}$$

and for the function f:

$$f(x) = \sum_{i}^{l} (\alpha_i - \alpha_i')\kappa(\mathbf{x_i}, \mathbf{x}) + b \tag{5.27}$$

The task has been transformed to the task of finding a kernel function, $\kappa(\mathbf{x}, \mathbf{x}')$. Fortunately, we do not have to find kernel functions for each and every problem. Instead, kernel functions are characterised by certain mathematical requirements and we can choose from known kernel functions and apply them

to the problem in question.
Kernel functions are characterised by Mercer's theorem [3], which states that a function $\kappa(\mathbf{x}, \mathbf{x}')$ is a kernel function, if:

$$\int_{\mathbb{R}} \kappa(\mathbf{x}, \mathbf{x}') g(\mathbf{x}) g(\mathbf{x}') d\mathbf{x}\, d\mathbf{x}' \geq 0 \tag{5.28}$$

$\forall g(x) \in L_2$ (meaning $\int g(\mathbf{x})^2 d\,\mathbf{x} < \infty$). From this theorem and its corollaries [87], kernel functions can be constructed. Examples for those functions include, polynomials:

$$\kappa(\mathbf{x}, \mathbf{x}') = (\gamma \mathbf{x} \cdot \mathbf{x}' + c)^d \tag{5.29}$$

the sigmoid kernel:

$$\kappa(\mathbf{x}, \mathbf{x}') = \tanh \gamma (\mathbf{x} \cdot \mathbf{x}') \tag{5.30}$$

and the Gaussian kernel:

$$\kappa(\mathbf{x}, \mathbf{x}') = \exp\left(-\gamma \|\mathbf{x} - \mathbf{x}'\|^2\right) \tag{5.31}$$

5.6.3.4 ν-SVM.

The algorithm described in the previous sections, finds an optimal hyperplane with at most ϵ margin to the target values. Since ϵ is a fixed value, the required accuracy has to be known in advance[4].
In some cases, however, (particularly in the case of the present analysis) the aim is rather to optimise to the best possible accuracy. Therefore [92] proposed a modification which automatically minimises ϵ. This is achieved by introducing a variable ν into the minimisation problem (compare with equation 5.17):

$$\frac{1}{2}\|\mathbf{w}\|^2 + C\left(\nu\epsilon + \frac{1}{l}\sum_{i=1}^{l} \xi_i\right) \tag{5.32}$$

The differences between this modification and the original method described previously concern mainly the implementation and we refer the reader to [93] for details.

[3] see [87] or [91] for a more formally correct form
[4] which is why the algorithm is sometimes called ϵ-*SVM*

5.6.4 Support Vector Machines: Application

The aim of the present analysis is to separate E^{-2} signal events from background. For use with the SVM we choose 5 variables to characterise each event (see section 5.6.1 for a detailed description):

- Hit probability
- Track resolution in θ
- Track resolution in ϕ
- Smoothness (P_{hit} version)
- Likelihood parameter difference

Consequently, the function we want the SVM to find is:

$$f : \mathbb{R}^5 \rightarrow \mathbb{R} \tag{5.33}$$

and target values are set to $y = 1$ for signal and $y = 0$ for background, meaning the SVM will (if successful) return values close to 1 for E^{-2} signal and close to 0 for background. For the present analysis, we used the software library *libsvm* developed by [94]. This *C++* -library implements ϵ-SVM and ν -SVM with four optional kernel functions (linear, polynomial, Gaussian and sigmoid). We choose to apply a ν-SVM with Gaussian kernel. Other kernels have been tested but did not give significantly different results.
For ν-SVM - apart from choosing the type of kernel function - there are essentially two parameters which should be chosen in advance. These are the parameter γ of the kernel function and the penalty parameter C [5]. To find the optimal set of these two parameters we apply the method of *cross validation*. A grid search in (γ,C) is performed and for any given pair of parameters the accuracy of classification is calculated by following steps:

- divide the training sample randomly into M sub-samples
- For each subsample: build hypothesis from the training data without subsample and determine the error rate of classification on the subsamples which were not used for learning.
- The resulting accuracy of the parameter pair is defined by the average error rate.

[5] the observant reader will have realised that ν is another free parameter, which we fixed for the present analysis.

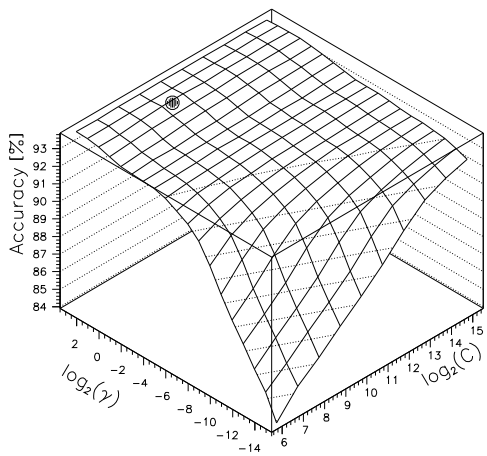

FIGURE 5.13*: Classification accuracy for different values of γ and C. For the analysis in this work $\gamma = 2$ and C = 2^8 was chosen, which is indicated by the filled circle.*

The training sample consisted of 11813 data events and 8938 simulated neutrino signal events. For this training sample, the accuracy of classification seems to be a rather slowly varying function of γ and C for parameter values $\gamma \gtrsim 2^{-4}$ and $C = 2^{12}$, see figure 5.13. We chose the parameters to be γ = 2 and $C = 2^8$, giving a accuracy of 93.8 %[6]. Figure 5.14 shows the achieved separation between data and signal with a energy spectrum $\propto E^{-2}$. It is noteworthy, that the present implementation of the SVM does not have the ability to treat weighted events. This implies that we had to use signal simulation with the intrinsic spectrum which is $\propto E^{-1}$, see section 5.2. This leads to some loss in efficiency, still the separation is satisfactory for our purposes. Figure 5.15 compares the SVM output for E^{-1} spectrum with the output for a E^{-2} spectrum. Also shown is the passing fraction of signal events as a function of cut on the SVM output for E^{-1}, E^{-2} and for an atmospheric neutrino spectrum ($\propto E^{-2.7}$). Passing fraction is here defined as $\frac{n_{\text{sig}}^{\text{passing}}}{n_{\text{sig}}^{\text{total}}}$ with $n_{\text{sig}}^{\text{passing}}$ being the number of signal events with SVM output values larger than the SVM cut

[6]the maximal accuracy was 93.9 %, however, at a penalty parameter $C = 2^{14}$, and since computing time is an increasing function of the penalty parameter, it was decided to accept the slightly lower accuracy.

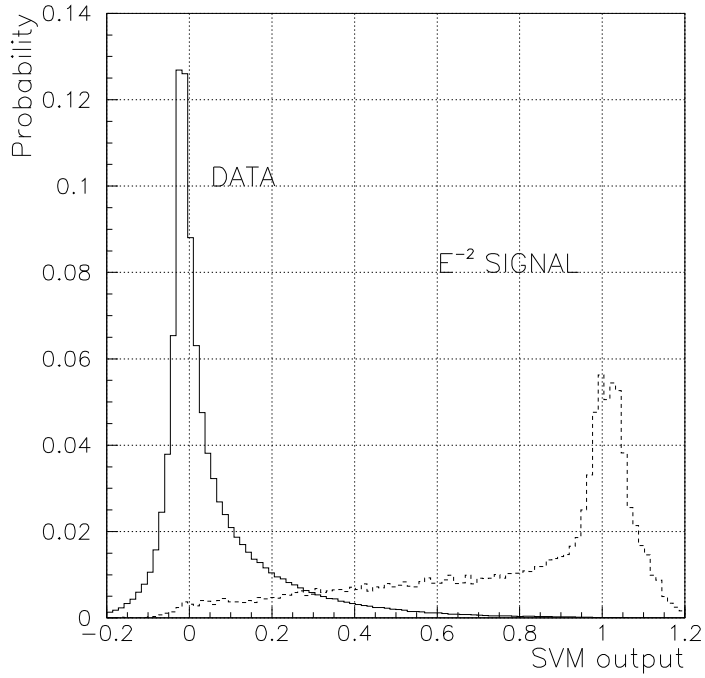

FIGURE 5.14*: The achieved separation between data and E^{-2} signal simulation*

value.
In section 5.6.5 we will see that cut optimisation leads to (zenith dependent) cuts on the SVM output varying between 0.90 and 0.96. From figure 5.15 it is estimated that the loss in efficiency due to the training on an E^{-1} spectrum is of the order of 15 %.

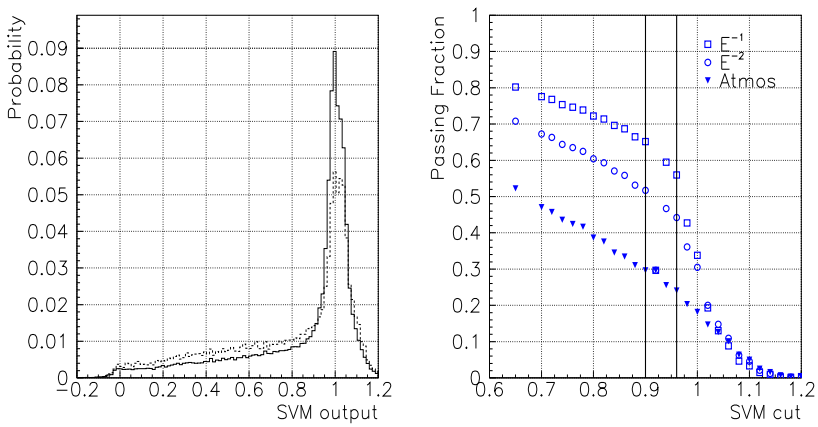

FIGURE 5.15*: Left hand: the SVM output for E^{-1} signal (solid) and for E^{-2} signal (dashed), right hand: the fraction of signal events passing a cut on the SVM output for E^{-1} (boxes), E^{-2} (circles) and atmospheric energy spectrum (triangles).*

5.6.5 Cut value optimisation and optimal bin size

For optimisation of the cut value one has to define a figure of merit, which is maximised (or minimised) with respect to the cut value. A common choice is to optimise on signal to noise, i.e. the optimal cut value for variable v is given by:

$$v_{\text{opt}} = v\left[\max\left(\frac{S(v)}{\sqrt{B(v)}}\right)\right] \tag{5.34}$$

Except for the first cut (on smoothness), here a different approach will be followed. The figure of merit chosen is the *model rejection factor* proposed by [95]. It is designed to give the strictest possible upper limit on a theoretical signal model.

5.6.5.1 The Model Rejection Factor

Considering a source flux $\Phi_\circ$ used as a signal prediction, the 90 % confidence upper limit [7] on the flux can be calculated by:

$$\Phi_{90} = \Phi_\circ \times \frac{\mu_{90}(n_{\text{obs}}, b)}{n_s} \tag{5.35}$$

Here μ_{90} is the 90 % upper confidence limit on the number of signal events (see.e.g. [96] and the discussion in part II) calculated from Poisson statistics, n_{obs} is the number of observed events and b the number of events expected from background. Obviously, minimising the ratio $\mu_{90}(n_{\text{obs}}, b)/n_s$ leads to the strongest constraint on the signal flux. This minimisation will be dependent on the data, since μ_{90} depends on the number of observed events. This bias can be removed by instead considering the *average upper limit*, $\overline{\mu_{90}}$. The average upper limit is defined as the average of all upper limits obtained from an ensemble of experiments with no signal process. This quantity is equivalent to the *sensitivity* introduced by [96], and can be calculated by:

$$\overline{\mu_{90}}(b) = \sum_{n_\circ=0}^{n=\infty} \mu_{90}(n_\circ, b) \frac{b^{n_\circ}}{n_\circ!} e^{-b} \tag{5.36}$$

The sensitivity will be one of the central results of this thesis and we will come back to this quantity in section 6. The figure of merit is consequently the ratio of the average upper limit and the number of expected signal events (from the model), that is we calculate the optimal cut value by:

$$v_{\text{opt}} = v \left[\min \left(\frac{\overline{\mu_{90}}(v)}{n_s(v)} \right) \right] \tag{5.37}$$

here $\overline{\mu_{90}}$ denotes the ensemble average over all upper limits with 90 % confidence level and n_s is the number of signal events surviving the selection criteria. The right side of equation 5.37 will be referred to as the model rejection factor (MRF).

5.6.5.2 Optimal bin size

In a grid search for point sources the choice of bin size is of obvious importance. The general idea behind bin size optimisation is illustrated by performing the calculation for the ideal case of a circular bin and Gaussian resolution

[7] generally, one chooses the confidence level to be $100(1-\alpha)\%$ with α = 0.1, 0.05 or 0.01. We choose $\alpha = 0.1$ for simplicity. The discussion holds for any α.

function. Then, the mean number of signal events expected within a circular bin is:

$$S \propto \int_0^R G(0,\sigma) d\,r \tag{5.38}$$

where $G(0,\sigma)$ represents a Gauss-function with standard deviation σ, centred on the source. For a background distributed uniformly in two dimensions, the mean number of expected background events is proportional to the geometric area:

$$B \propto \pi R^2. \tag{5.39}$$

Maximising $\frac{S}{\sqrt{B}}$ yields

$$R_{\text{opt}} = 1.585\,\sigma. \tag{5.40}$$

For a quadratic bin the solution is slightly smaller $W_{\text{opt}} \sim 1.4\ \sigma$, W_{opt} being the half width of the quadratic bin.

5.6.5.3 Cut value and bin size optimisation in the present analysis

The cylindrical geometry of AMANDA suggests, that the (unoptimised) response of the detector is independent of azimuth angle but depends on zenith angle. This is in particular true for the angular resolution (which is confirmed later on in the analysis, see figure 6.4). It is therefore advantageous to perform the cut optimisation in zenith bands within which the response can be assumed to be constant. Furthermore, in optimising the bin size, the numeric solution given in the previous section can not be used: the angular resolution of the detector is non- Gaussian (see figure 6.2) and it was decided to use the MRF as a figure of merit. Also, the variables in the SVM were chosen with the aim to improve the angular resolution, meaning that SVM cut value optimisation and bin size optimisation will be coupled and should consequently be performed at the same time.
These considerations lead to following algorithm for cut and bin size optimisation in the present analysis:

- The sky is divided into 10 zenith bands between 90° and 180° with 10° width each.
- For each zenith bin a point source is simulated using the full detector simulation.
- For each point in (bin size, SVM cut) space, the MRF is calculated for a quadratic (in solid angle) bin centred on the source. The expected

background b is calculated from all events in the zenith band scaled to the bin size.

- the pair of values for (bin size, SVM cut) with minimal MRF is chosen as optimal cut value and bin size.

Figure 5.16 exemplifies the result of such an optimisation. Shown is the logarithm of the MRF as a function of SVM output cut and half bin size for the zenith band between zenith = 130° and zenith =140°. The results for all zenith bands are summarised in table 5.1.

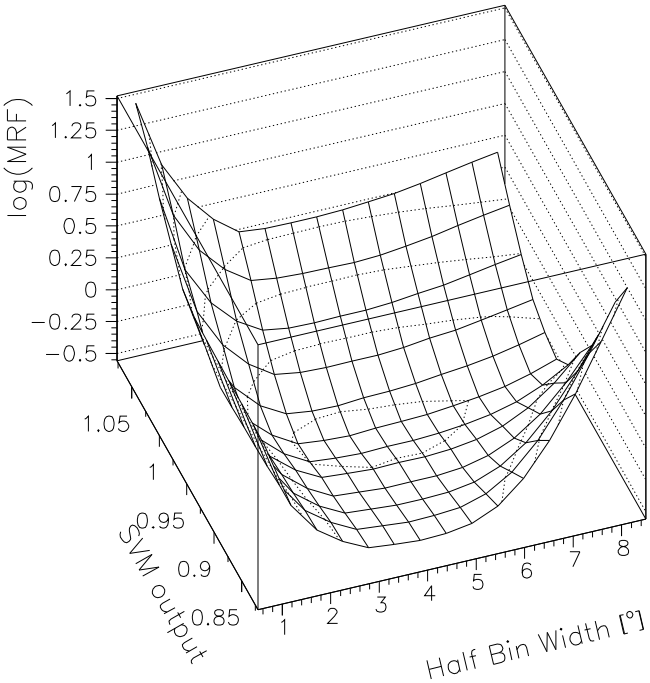

FIGURE 5.16*: Example of the result of simultaneous bin size/SVM cut optimisation with the MRF as figure of merit.*

Zenith band [°]	Optimal SVM cut	Optimal Half Bin Size [°]
90-100	0.94	5
100-110	0.94	5
110-120	0.94	5
120-130	0.92	5
130-140	0.96	4.5
140-150	0.96	3.5
150-160	0.96	3.
160-170	0.94	3.
170-180	0.90	2.5

TABLE 5.1*: The results of the SVM cut value and bin size optimisation*

5.7 The processing chain

Table 5.2 summarises the processing that the data and the signal simulation was subjected to. A first reduction of the data is done centrally together with the calibration, a first cleaning and the first five reconstructions. The resulting data set (commonly referred to as *level 2*) reduces the data set to $\sim$ 1 % of the data on trigger level and keeps $\sim$ 50 % of E^{-2} signal. This reduction is achieved by three cuts: a cut on the zenith angle returned by the line fit (see section 5.5), a cut on the zenith angle returned by the first (non-iterative) likelihood reconstruction and a cut on the number of *direct hits*, N_{dir}. Direct hits are hits which have reached the optical module with only a small delay, the delay being calculated relative to a Čerenkov photon emitted from the reconstructed track. The size of the delay can be chosen differently, here the delay window was [-20:25] ns. The negative lower bound accounts for uncertainties in the calibration of geometry and time. In table 5.2 we omit reconstructions which have not actually been used in the analysis.

5.8 Analysis of the final sample: Strategy

Having isolated a sample of events, the next task is to investigate it for possible clustering in declination/right ascension space and to calculate confidence intervals on the flux of neutrinos from cosmic point sources. In this work, two strategies will be followed: the *grid search*, in which the whole sky is covered with a grid of search bins, and the *search for selected sources*, where a search bin is centred on a potential neutrino source (usually an astronomical object). Details for the two strategies will are described in this section.

Reco Type	Initial Guess	cuts	cleaning	ϵ_{data}
Trigger				1.
Line fit	-	zenith(line fit) >90		
1x Likelihood	Line Fit	zenith(1x Likelihood) >80		
Level 2				0.01
-	-		Run & OM	
-	-	zenith(1×Likelihood)> 90	x-talk cleaning	
16x Iterative	1×Likelihood	zenith(16 x Iterative) >90°		$3 \cdot 10^{-3}$
16x Bayesian	Likelihood	$\lvert S_{mrl} \rvert$(16×Iterative)>0.22	$3 \cdot 10^{-4}$	
Parabola	16×Iterative	$\sigma_{\Delta_\phi, \Delta_\theta} > 0$		
Level 6		SVM		$4 \cdot 10^{-6}$

TABLE 5.2: *The processing chain of the present analysis. For details see text.*

5.8.1 Grid search

In a grid search the hemisphere is divided into a large number of rectangular bins. In this analysis a type of grid is devised, which will be referred to as the *lid grid*. In order to be able to treat sources at highest declinations, one single cell is placed at $\theta = 180°$. Using a single grid is not optimal with respect to an unknown source position (imagine a source lying on a cell boundary). Therefore four different grids are devised. The first (null) grid is defined by an integer number of grid cells in declination starting with $\theta = 90°$ and an integer number of grid cells in right ascension (starting with right ascension = 0 h). The number of grid cells is hereby chosen such that the size of the cells is as close as possible to the optimal bin size found in section 5.6.5. The second grid is obtained from the first by a rotation in right ascension by half a bin width. The third grid is obtained by shifting the null grid by half a bin width in zenith. Instead of a single lid cell, now the highest zenith bin is divided into three cells in order to take care of those hypothetical sources lying on the edge of the lid cell. The fourth grid, finally, is obtained from the third grid by rotation by half a bin width in right ascension. The situation is illustrated in figure 5.17. For the calculation of the limits we will then compare the number of observed events in each cell with a background expectation which is determined by averaging over all off-source bins in the same zenith band.

5.8.1.1 Accessing the significance of an excess

Supposed an excess over a background expectation is detected, the statistical significance of this excess should be determined. In this analysis, the *excess significance* will be defined via:

The probability of detecting an excess larger or equal to the experimental value in an experiment identical to the one actually performed but with no signal.

The smaller this probability the larger the significance of an excess. To quantify an excess, we define the *excess parameter*:

$$\xi = -\log \sum_{n=n_{\text{obs}}}^{n_{\text{tot}}} P^{\text{binom}}(n|n_{\text{tot}}, N_{\text{bins}}) \tag{5.41}$$

with

$$P^{\text{binom}}(n|n_{\text{tot}}, N_{\text{bins}}) = \binom{n_{\text{tot}}}{n} \cdot \left(N_{\text{bins}}^{-1}\right)^{n} \cdot \left(1 - N_{\text{bins}}^{-1}\right)^{n_{\text{tot}}-n}$$

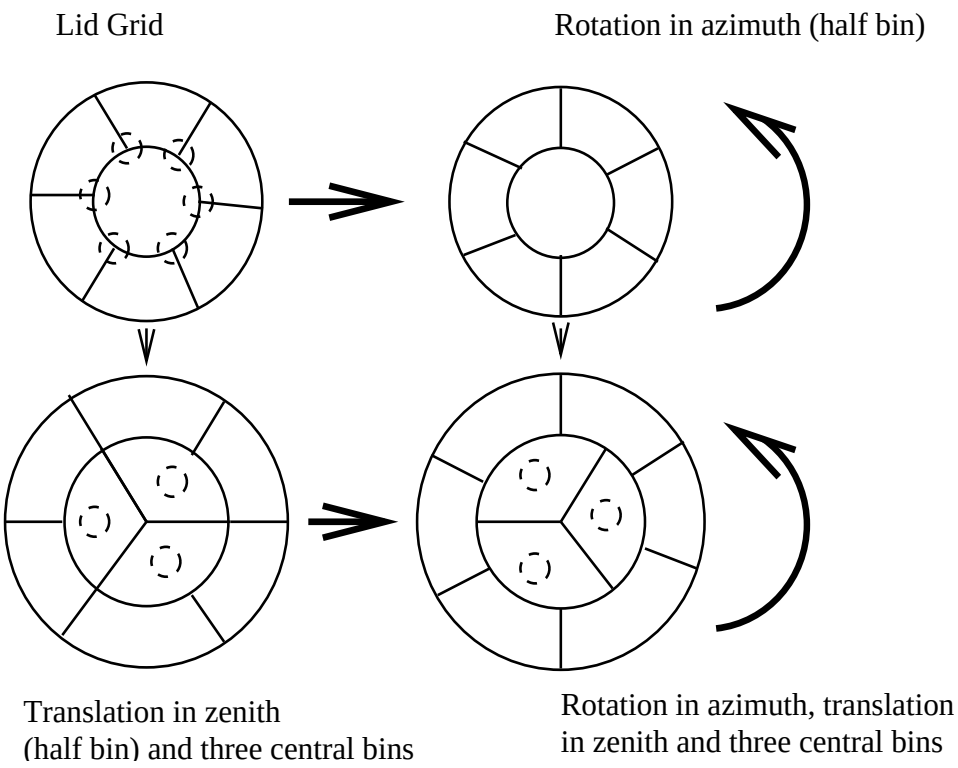

FIGURE 5.17: *The lid grid illustrated. Four different grids are devised: two grids with a lid cells and two grids with three cells in the upper-most zenith band. Hypothetical sources which would be covered by the splitting in the three upper most cells are indicated by the dashed circles.*

Equation 5.41 yields the probability of detecting n_{obs} or more events in one bin, given N_{bins} number of bins and n_{tot} number of events in total in the zenith band, i.e. would be identical to the above defined excess significance in the case that our experiment consisted of a grid only covering one zenith band with (uncorrelated) search bins. The grid proposed in the previous section, however, consists of 1092 grid cells (including grid shifts) with different number of events in each zenith band. Furthermore the search bins are obviously not all uncorrelated. Therefore, it is decided to use a Toy Monte Carlo simulation to calculate the excess significance. The Toy Monte Carlo proceeds as follows:

- a pseudo experiment is constructed by randomising the data in right ascension, i.e. an experiment without source.
- for each pseudo experiment a grid search is performed, identical to the one performed in the actual experiment.
- for each pseudo experiment the excess significance parameter is determined for each bin.
- for each pseudo experiment the maximal excess parameter is determined.
- the first four steps are repeated n_{pseudo} times.

In this way a distribution of the n_{pseudo} maximal excess parameters are obtained. The excess significance of the maximal excess found in the actual experiment is then calculated from:

$$\Xi = \frac{n(\xi_{\text{max}} > \xi_{\text{max}}^{\text{exp}})}{n_{\text{pseudo}}} \tag{5.42}$$

A number of relatively weak sources will not necessarily be found by just concentrating on the maximal excess parameter. As an indication for the existence or non-existence of an overabundance of excesses just below the maximal excess , we calculate the probability:

$$\beta = P\left(n(\xi > \xi_{\text{exp}}) > n_{\text{exp}}(\xi > \xi_{\text{exp}})\right) \tag{5.43}$$

In practise, we will take the ith largest excess, ξ_i, in the experiment and calculate the probability that there will be at least i cells with an excess larger than ξ_i, thus a bias towards a larger number of high excesses in the experiment would reveal itself by a low probability to find a larger (or equal) number of higher (or equally high) excesses in the random sample. In the case of the maximal excess, this probability is the same as Ξ (defined in equation 5.42).

5.8.2 Selected sources

We will present neutrino flux limits for in total 20 preselected sources, which are chosen among potential candidates for high energy neutrinos. As we have seen in section 2, blazars which are known sources of TeV gamma rays are good candidates for neutrino production. We present limits for 6 experimentally confirmed TeV gamma ray sources , which represent all *TeV blazars* in the northern hemisphere as listed by the EGRET catalogue [97].
While TeV sources are certainly good candidates for neutrino production in AGN jets, it has been argued that TeV gamma ray sources are probably weak sources for neutrinos originating in the core. The reason is that TeV emission requires a comparatively low UV photon density which in turn suppresses $p\gamma$ interaction [98]. Blazars with known gamma emission in the GeV range do not suffer from this constraint. We therefore include 3 *GeV blazars* selected from the EGRET catalogue into the list hypothetical sources. These three sources fulfil two additional constraints: firstly, a constraint on the V luminosity of the AGN (this constraints the number density of UV photons) and secondly the condition that a jet either has not been observed at all or that its projected length has been estimated to be less than 1 kpc (which implies that the jet is emitted almost in line of sight with respect to the observer). The reader is referred to [98] for a detailed discussion.
Another possible source of high energy neutrinos, which has been mentioned in section 2 are Microquasars. We include 8 known Microquasars on the northern hemisphere in our list of selected sources. Finally, we include 3 Super Nova Remnants in the list.

CHAPTER 6

Results

6.1 General definitions

6.1.1 Flux limits and effective area

In this analysis, signal efficiency is calculated by the detector simulation. Suppose a point source with differential flux $\left(\frac{d\Phi_\nu}{dE_\nu}\right)_\circ$ is simulated. Then, for each search bin, the differential flux limit can be calculated from the number of signal events, n_s, which pass all cuts, the number of detected events, $n_\circ$, in that bin and the expected background, b:

$$\left(\frac{d\Phi_\nu}{dE_\nu}\right)_{90} = \frac{\mu_{90}(n_\circ, b)}{n_s} \cdot \left(\frac{d\Phi_\nu}{dE_\nu}\right)_\circ \tag{6.1}$$

where $\mu_{90}(n_\circ, b)$ denotes the 90 % upper confidence limit on the number of expected signal events. The limit of equation 6.1 is independent of the assumed absolute normalisation of the flux, but depends on the spectral shape and is not easily converted to different fluxes. To be able to calculate the number of events from an arbitrary flux, it is therefore useful to define a quantity related to the signal detection efficiency, the *effective area:*

$$A_{\text{eff},\nu\mu}(E_{\nu\mu}, \Theta_{\nu\mu}) := \frac{\dot{n}^{\text{det}}_{\nu\mu}}{\Phi_{\nu\mu}} \tag{6.2}$$

where $\Phi_{\nu\mu}$ denotes the incident flux of neutrinos or muons and $\dot{n}^{\text{det}}_{\nu\mu}$ is the number of detected events (originating from that flux) per unit time. In AMANDA, the effective area is a function of the energy, $E_{\nu\mu}$, and the zenith angle of incident particles, $\theta_{\nu\mu}$. To simplify the discussion we will not explicitly state the

zenith dependence, but assume it implicitly.
The effective area is useful to characterise the signal efficiency since it relates detected rates directly to flux. We will present effective areas for both the neutrino and the muon, since we are trying to find a flux of neutrinos but are detecting muons.
Using the definition given in equation 6.2, the number of signal events, n_s, detected during the data taking time, T_{live}, given an arbitrary differential flux $\left(\frac{d\Phi_\nu}{dE_\nu}\right)_\circ$, is:

$$n_s = T_{\text{live}} \int_{E_\nu^{\text{min}}}^{E_\nu^{\text{max}}} dE_\nu \, A_{\text{eff},\nu}(E_\nu) \left(\frac{d\Phi_\nu}{dE_\nu}\right)_\circ \tag{6.3}$$

Given the function $A_{\text{eff},\nu}(E_\nu)$, this expression thus allows to calculate the number of events expected in the detector for any arbitrary flux. On the other hand, from 6.1, the integral flux limit is given by:

$$\Phi_\nu(E_\nu^{\text{min}} < E_\nu < E_\nu^{\text{max}})_{90} = \frac{\mu_{90}(n_\circ, b)}{n_s} \cdot \int_{E_\nu^{\text{min}}}^{E_\nu^{\text{max}}} dE_\nu \left(\frac{d\Phi_\nu}{dE_\nu}\right)_\circ \tag{6.4}$$

Inserting equation 6.3 into 6.4 thus allows to calculate a flux limit for arbitrary fluxes knowing the function A_{eff} and the upper limit found in the experiment. The resulting expression can be simplified by the definition of the *energy-averaged effective area*:

$$\overline{A_{\text{eff},\nu}}(E_\nu^{\text{min}} < E_\nu < E_\nu^{\text{max}}, \frac{d\Phi_\nu}{dE_\nu}) = \frac{\int_{E_\nu^{\text{min}}}^{E_\nu^{\text{max}}} dE_\nu \, A_{\text{eff},\nu}(E_\nu) \cdot \frac{d\Phi_\nu}{dE_\nu}}{\int_{E_\nu^{\text{min}}}^{E_\nu^{\text{max}}} dE_\nu \, \frac{d\Phi_\nu}{dE_\nu}} \tag{6.5}$$

With this definition 6.4 becomes:

$$\Phi_\nu(E_\nu^{\text{min}} < E_\nu < E_\nu^{\text{max}})_{90} = \frac{\mu_{90}(n_\circ, b)}{T_{\text{live}} \cdot \overline{A_{\text{eff},\nu}}} \tag{6.6}$$

The integral limit is thus inversely proportional to the energy-averaged effective area $\overline{A_{\text{eff},\nu}}$.
The limits which we will present in this thesis will be calculated using equation 6.1, thus not make use of expression 6.6. However, the functions $A_{\text{eff},\nu}$ and $\overline{A_{\text{eff},\nu}}$ contain useful information, which is why they will be presented in addition. For example, the limits presented in section 6.6 are for a spectrum with power law index, $\gamma = -2$. They can in principle be converted into integral limits for spectra with arbitrary power law index knowing the function $A_\nu(E_\nu)$ and by multiplying the presented limit with $\frac{\overline{A_{\text{eff},\nu}}(-2)}{\overline{A_{\text{eff},\nu}}(\text{arb})}$.

6.1.2 The sensitivity

It has been noted that schemes of calculating frequentist confidence intervals lead to an undesired effect (see for example [96] and the discussion in chapter 8). If significantly less events are detected than are expected from background, the limit becomes stricter with increasing background expectation. This may be considered undesirable, since it is not connected with an increased sensitivity of the experiment to signal, but rather a downward fluctuation of the background.
It has therefore been suggested [96] that together with the limit one should also present the *sensitivity*, which is defined as the average upper limit one would obtain in a large number of experiments with no signal (see also chapter 5, section 5.6.5). This quantity can be calculated by:

$$\overline{\mu_{90}}(b) = \sum_{n_\circ=0}^{n=\infty} \mu_{90}(n_\circ, b) P(n_\circ|b) \tag{6.7}$$

where $P(n_\circ|b)$ denotes the Poisson probability to detect $n_\circ$ events given a background, b. μ_{90} is the corresponding 90 % confidence upper limit on the number of signal events. The sensitivity to a hypothetical source flux will therefore be given by:

$$\left(\frac{d\Phi_\nu}{dE_\nu}\right)_{90} = \frac{\overline{\mu_{90}}(b)}{n_s} \cdot \left(\frac{d\Phi_\nu}{dE_\nu}\right)_\circ \tag{6.8}$$

for the sensitivity on differential flux. Note that, in contrast to common language, an increase in sensitivity means that - on average - the limit the experiment will report will be *less* stringent. Consequently, optimising the analysis means trying to achieve a *low* sensitivity.

6.2 Angular resolution.

The angular resolution of the detector is assessed using the detector simulation. It is conveniently characterised by the space angle difference, which can be calculated from the true (known from simulation) and reconstructed zenith and azimuth angles:

$$\cos\Psi = \cos\Theta_{\text{fit}} \cos\Theta_{\text{true}} + \sin\Theta_{\text{fit}} \sin\Theta_{\text{true}} \cos\left(\phi_{\text{fit}} - \phi_{\text{true}}\right) \tag{6.9}$$

Here Θ_{fit} and Θ_{true} are the reconstructed and true zenith angle and ϕ_{fit} and ϕ_{true} the corresponding azimuth angles. The definition is illustrated in figure 6.1.

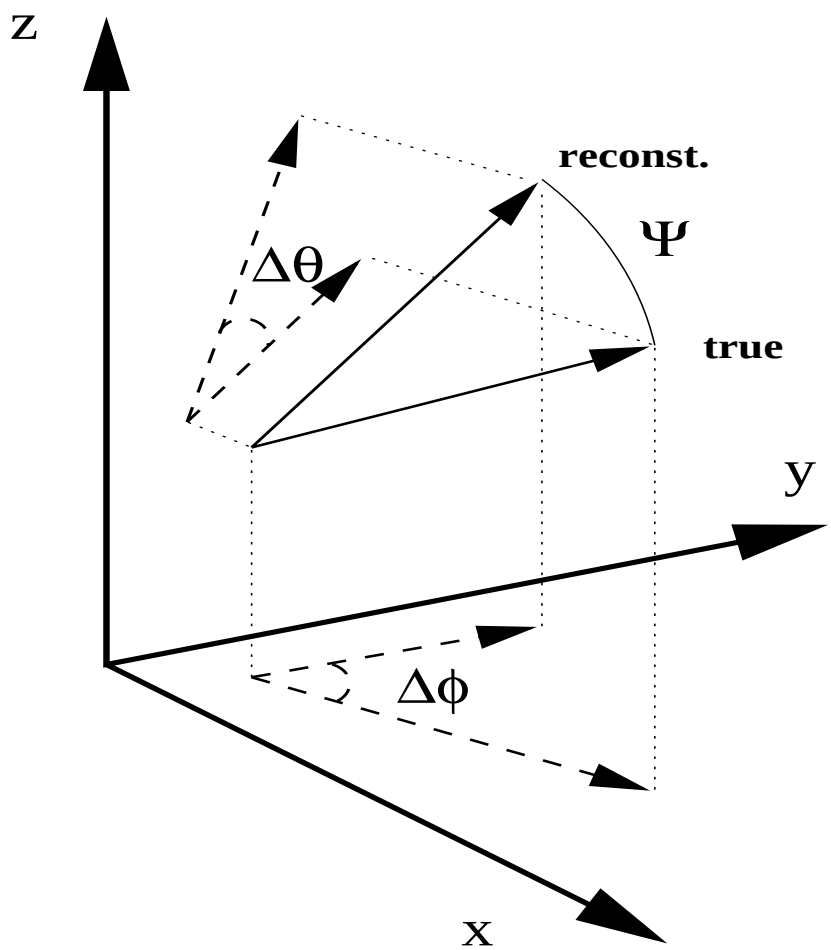

FIGURE 6.1: *The definition of space angle difference in terms of zenith and azimuth mismatches.*

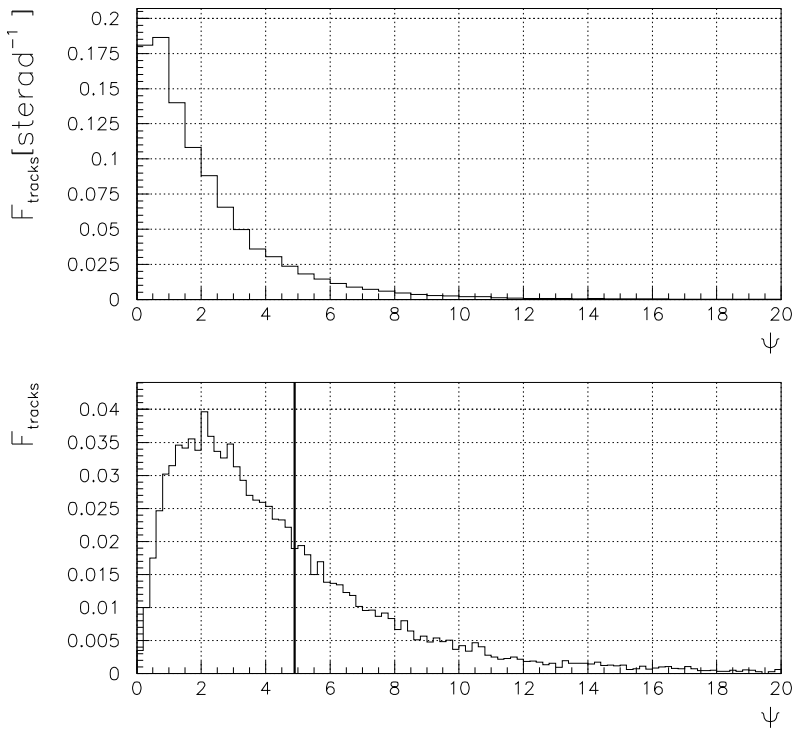

FIGURE 6.2*: Upper panel: the point spread function for the final sample of this analysis, lower panel: the distribution of space angle difference for the final sample of this analysis. The solid line indicates the space angle resolution (see text for definition). The distributions have been normalised to yield an integral equal one.*

Figure 6.2 shows the distribution of the space angle difference and the point spread function (space angle difference distribution divided by the corresponding solid angle element). We define the resolution by integrating the distribution of space angle difference to the value which confines 68% of all reconstructed tracks:

$$0.68 = \int_0^{\Psi_{68}} d\Psi \, f(\Psi) \tag{6.10}$$

Table 6.1 summarises the results for the space angle resolution. It has been customary to define the space angle resolution in terms of median space angle difference [82][83], which for the sake of comparison is included in table 6.1. Also included are its values prior to the SVM cut. The application of the SVM improves the angular resolution considerably. For illustration, figure 6.3 shows

	Prior SVM	Post SVM
Ψ_{68}	6.7	**4.9**
Ψ_{50}	4.5	**3.5**

TABLE 6.1*: The space angle resolution after and prior to the application of the SVM. Also shown is the median space angle difference.*

the distributions of the azimuth and zenith angle mismatch separately.

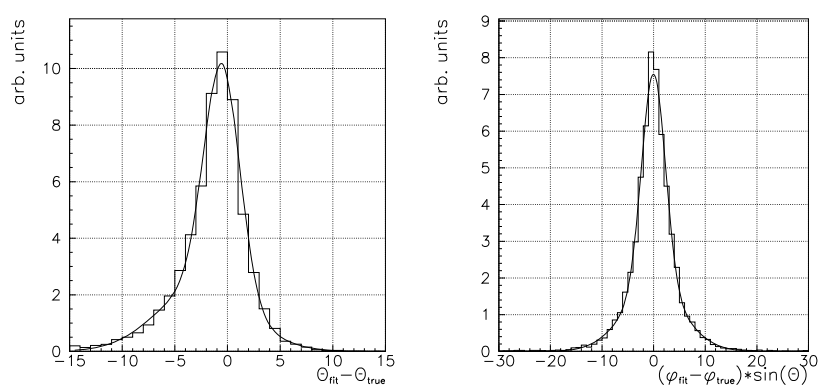

FIGURE 6.3*: Zenith and azimuth mismatches for the final sample of the data. The distributions are reasonably well fit by the sum of two Gauss functions. The azimuth distribution has been multiplied by* $\sin\Theta$ *to account for the zenith dependence of the covered solid angle.*

The distributions are reasonably well fitted by the sum of two Gauss functions:

$$f(x = \theta, \phi) = A_1 G(\sigma_1, x_{01}) + A_2 G(\sigma_2, x_{02}) \tag{6.11}$$

which might indicate the presence of two distinctive classes of events. Table 6.2 summarises the fit results. It should be noted that, in contrast to previous analyses [82],[83] we do not need to parametrise the resolution function for the sake of finding the optimal bin size. Instead we use the (zenith-wise) distribution of angular mismatch as provided by the full detector simulation. Figure 6.4 shows the space angle resolution as a function of zenith angle and for comparison the bin size used in the present analysis, cf. section 6.4. The resolution varies from $\sim 5.8\,^\circ$ to $\sim 3\,^\circ$, which is consistent with the used bin size.

Distribution	A_1	σ_1	x_{01}	A_2	σ_2	x_{02}
$\Delta\Theta$	1.	1.68	-0.53	0.28	4.24	-2.4
$\Delta\phi$	1.	2.30	-0.02	0.27	5.88	-0.1

TABLE 6.2*: The result of the fit of the sum of two Gauss functions to the zenith angle and azimuth angle mismatch.*

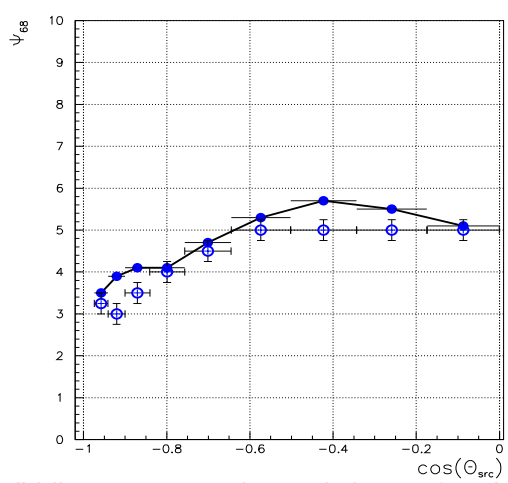

FIGURE 6.4*: Solid line: space angle resolution as function of zenith angle. Also shown are the half width of the bins used in the grid search. Horizontal error bars are zenith bin width, vertical are the step width in bin size used in the bin size optimisation.*

6.3 Sky-plot

Figure 6.5 shows the distribution of the reconstructed zenith angle and right ascension of the final sample. The right ascension distribution shows no visible structure. The distribution is consistent with a flat distribution on 90 % confidence level (inferred from Kolmogorov-Smirnov test). The zenith distribution reflects the zenith dependent background rejection capability of the SVM, which seems to decrease significantly for zenith angles between 140° and 160°. Figure 6.6 shows the sky-plot, i.e. the distribution of events in equatorial coordinates.

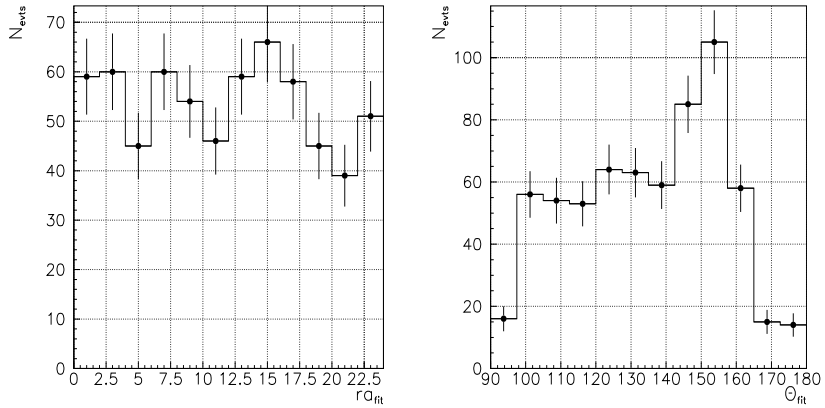

FIGURE 6.5*: Right ascension (left) and zenith angle distribution (right) of the final sample. Note declination δ = Θ -90°*

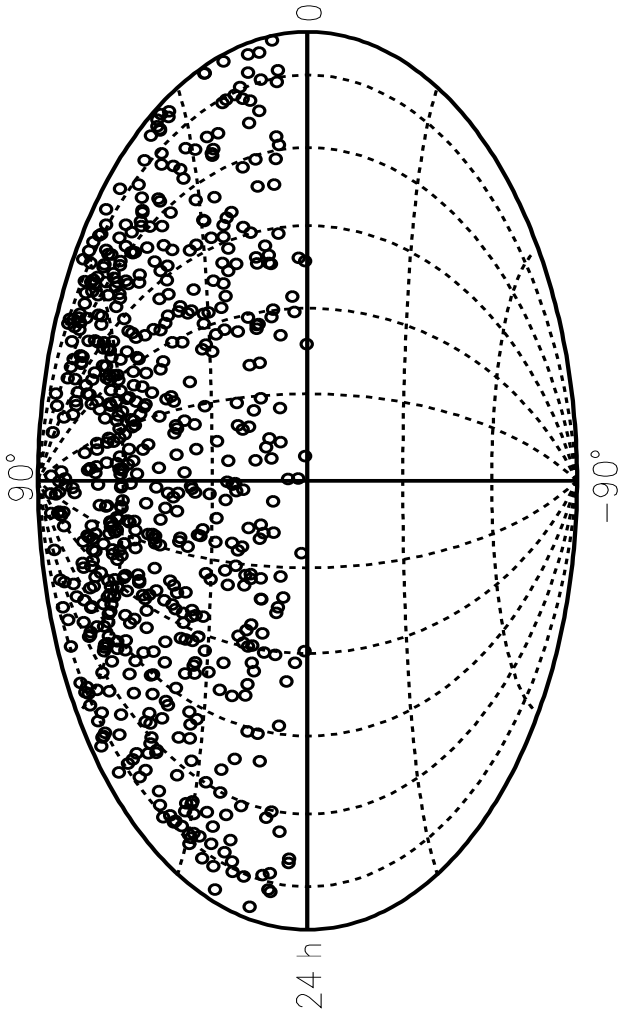

FIGURE 6.6: *The 642 events of the final data set in equatorial coordinates.*

6.4 Grid searches for point sources

6.4.1 Effective area and sensitivity

Figure 6.7 shows the effective area for neutrinos as a function of energy and for four different zenith angles. For lower energy the effective area for smaller zenith angles (shallower directions) is smaller than for larger zenith angles (more vertical directions). This is expected from the cylindrical geometry of the array since horizontal tracks have a smaller lever arm for reconstruction. The effective area increases up to energies of 100 - 1000 TeV where it reaches

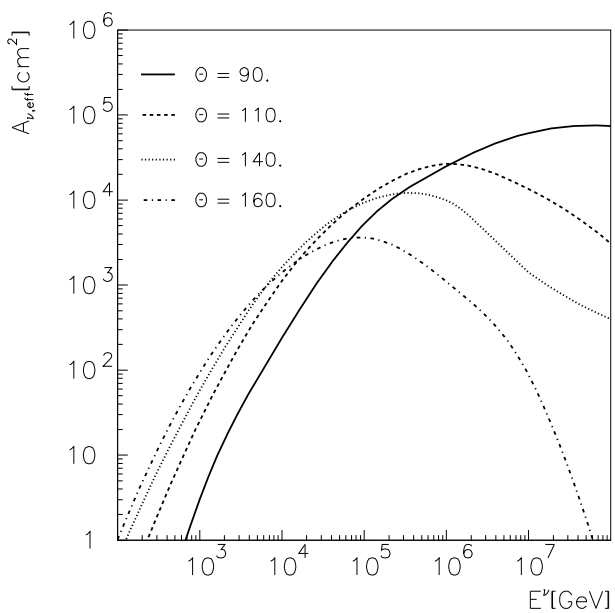

FIGURE 6.7*: The effective area for neutrinos for different zenith angles.*

a maximum and starts to decrease or flattens out. The position of this maximum is correlated with the zenith angle: the larger the zenith angle the smaller the energy at which the maximum is reached. Part of this behaviour can be qualitatively understood by considering the interaction length of the neutrino

in charged current interactions. The interaction length is inversely proportional to the charged current cross-section, thus decreases with energy. At energies of about 40 TeV the interaction length becomes comparable to the Earth diameter, which means neutrino absorption in the Earth will become important above this energy. For a more quantitative discussion the reader is referred to [99].

The effective area for muons (see figure 6.8) also decreases for very high energies, however, the turn around seems to be at roughly the same position irrespective of zenith angle. This behaviour is interpreted as an instrumental effect: for large light output the reconstruction algorithm does not perform very efficiently. This effect also contributes to the decrease in the effective area for neutrinos discussed previously.

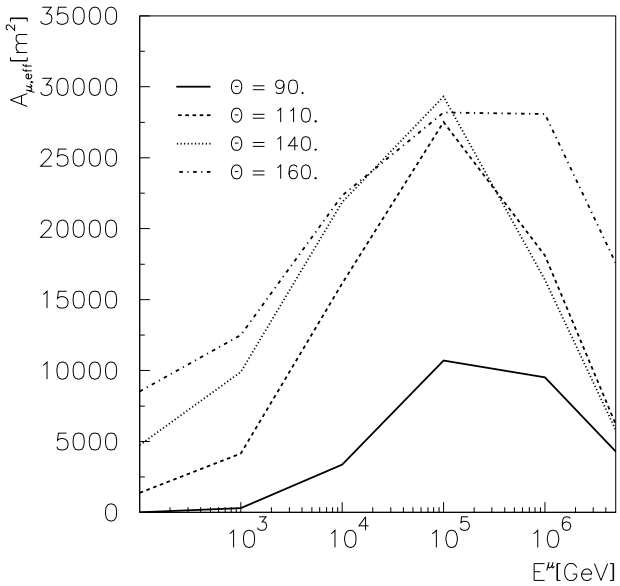

FIGURE 6.8: *The effective area for muons for different zenith angles. The effective area is shown as a function of energy at closest approach to the detector centre.*

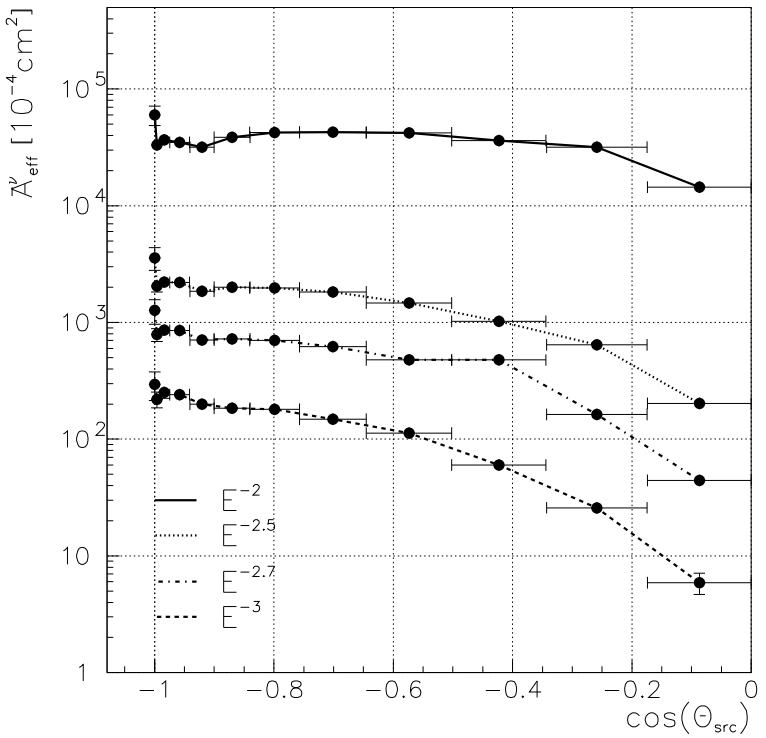

FIGURE 6.9*: Energy averaged effective area for neutrinos. Different slopes of the neutrino spectrum have been assumed. Error-bars account for the statistical uncertainty. The effect of neutrino absorption in the Earth is included.*

The energy averaged effective area is shown for neutrinos in figure 6.9 and for muons in figure 6.10. Different slopes of the neutrino spectrum have been assumed. The achieved area for neutrinos with an energy spectrum $\propto E^{-2}$ is around 5 cm^2 and it is relatively constant for zenith angles larger than 120°. The fluctuation seen for the most vertical bin is partly due to the statistical uncertainty in the signal prediction, partly due to a systematic effect in the ice model implementation (see section 6.5).

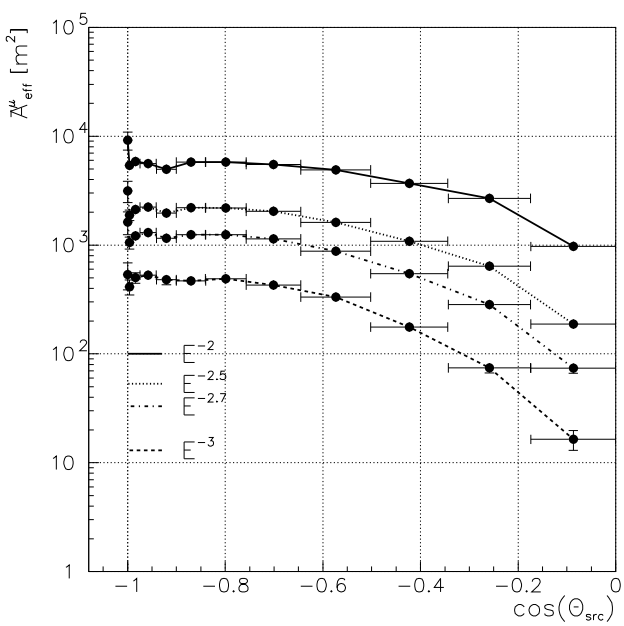

FIGURE 6.10: *Energy averaged effective area for muons as a function of zenith angle. Different slopes of the neutrino spectrum have been assumed. Error-bars account for the statistical uncertainty.*

Figure 6.11 shows the bin efficiency (defined as the fraction of muons which are reconstructed within the search bin). The bin efficiency is more or less constant at around 67 % with a drop of a few percent for zenith angles larger than $\sim 160°$. The relative constancy of the bin efficiency is achieved by the variable bin size (see figure 6.4). The distinctive rise at $\Theta = 180°$ again is attributed to the statistical and systematic uncertainties.

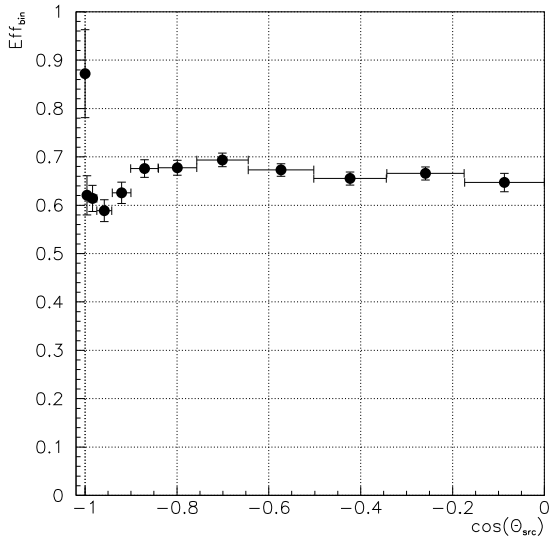

FIGURE 6.11: *Bin efficiency (fraction of muons reconstructed within source bin) as obtained for the lid grid. The vertical error bars account for the statistical uncertainty, horizontal bars represent the zenith bin width.*

The sensitivity achieved by the present analysis (without including systematic uncertainties) is shown in figure 6.12 and summarised in table 6.3. The sensitivity varies between ~ 3 and $12 \cdot 10^{-7}$ GeV cm^{-2}s^{-1}. The rise by roughly 20 % for zenith angles between $\sim 140°$ and $\sim 160°$ is partly due to the increased background (see figure 6.5) partly due to a decrease in signal efficiency in that region. The rise for shallow angles (< 100 °) is due to the drop in signal efficiency. The signficant drop for the most vertical bin is due to the previously mentioned effect of the ice implementation. We will return to that point in the discussion of the systematic uncertainties in section 6.5. Figure 6.13 shows the energy distributions of the neutrinos and muons on the final level. The mean energy of those neutrinos is ~ 50 TeV, the mean energy of muons (energy at closest approach to the center of the detector) is ~ 10 TeV.

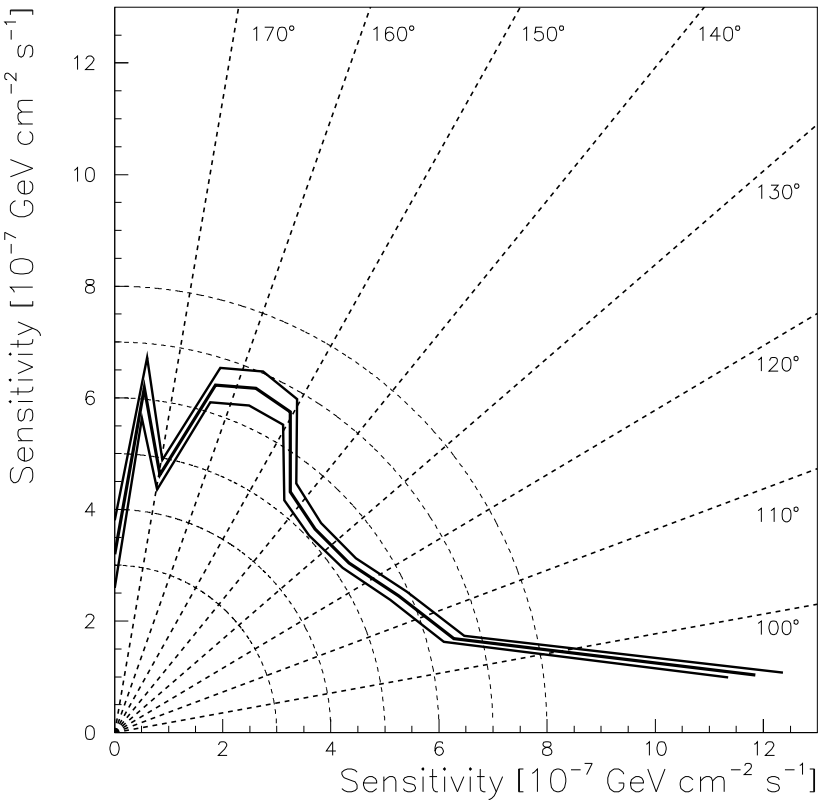

FIGURE 6.12*: The sensitivity for the lid-grid in polar coordinates. The band corresponds to the statistical uncertainties of the signal simulation.*

Zenith [$\circ$]	N_{bins}	N_{events}	Sensitivity [10^{-7}GeVcm^{-2}s^{-1}]
90-100	35	36	11.9
100-110	34	72	6.5
110-120	32	71	5.8
120-130	29	81	5.3
130-139	28	77	5.2
139-147	27	82	5.4
147-154	25	105	6.6
154-160	23	52	6.7
160-166.5	15	42	6.5
166.5-172.5	10	10	4.7
172.5-177.5	6	12	6.2
177.5-180.	1	$b = 1.6$	3.2

TABLE 6.3*: Results of the grid search:the zenith band boundaries, number of bins in the zenith band, N_{bins}, number of events in zenith band, N_{events}, and the calculated sensitivity. The expected background, b, in the lid cell has been estimated from a surrounding zenith band.*

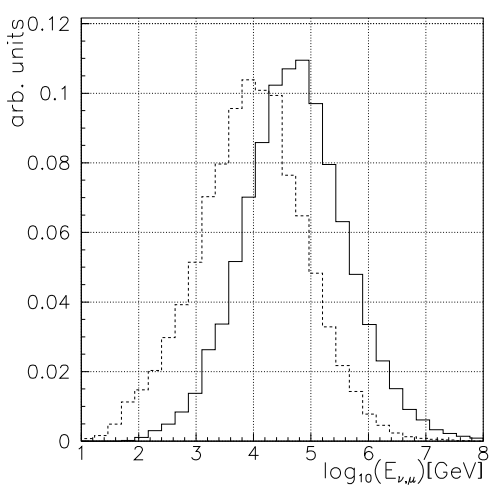

FIGURE 6.13*: The energy distribution of E^{-2} neutrinos (solid) and muons induced by E^{-2} neutrinos (dashed) on the final level of the present analysis. The muon energy is the energy at closest approach to the detector centre.*

6.4.2 Excess significance

In figure 6.14, the distribution of excess parameters found in the present analysis is compared to the one found from 10^4 pseudo experiments in each of which the 642 final events are assigned random right ascensions. The experimental distribution is consistent with the no source distribution on the > 5 σ level (calculated by Kolmogorov-Smirnov test). Also shown is how a hypothetical source with an excess corresponding to the detection threshold (see section 6.4.3) would appear in this figure.

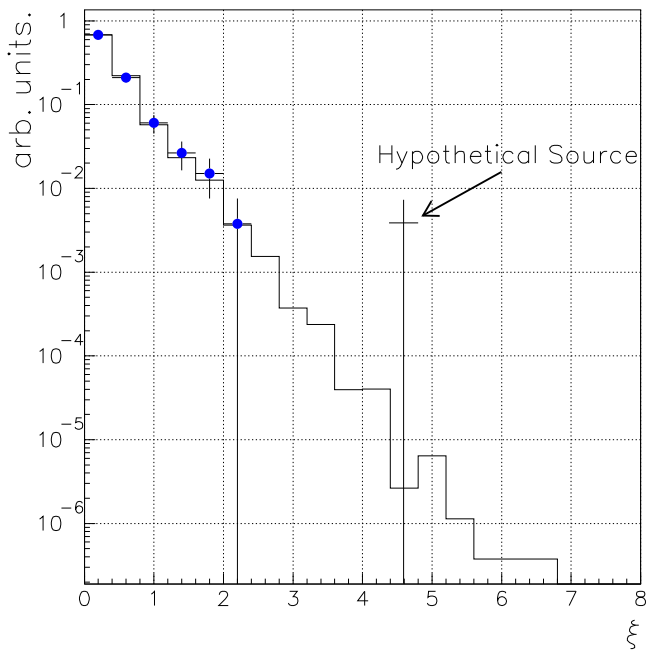

FIGURE 6.14: *The excess parameter distribution obtained from a sample of 10000 pseudo experiments randomised in right ascension as compared to the experiment. Also indicated is how a hypothetical source (with a flux corresponding to the detection threshold, see section 6.4.3) would appear in this figure.*

Figure 6.15 shows the distribution of the maximum excess parameter as obtained from 10^4 pseudo experiments. From integration one obtains Ξ = 94 %

(see equation 5.42 for a definition of Ξ). In words, there is a 94 % probability of obtaining a maximal excess larger than the experimentally found maximal excess from an ensemble of experiments without a source. Also shown is Ξ as a function of maximal signifcance parameter. The coordinates of the four

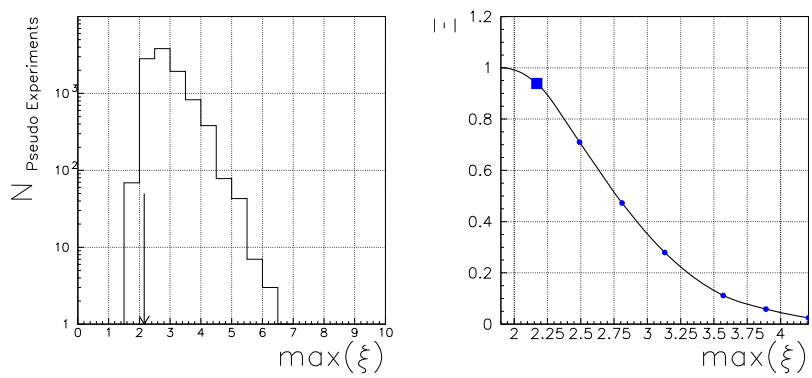

FIGURE 6.15*: On the left: the distribution of maximal excess parameters given by 10^4 pseudo experiments without a source. The arrow indicates the experimentally found maximal excess. On the right: the excess significance, Ξ, as a function of the maximal excess parameter. The filled rectangle indicates the maximal excess parameter found in the present analysis.*

largest excesses are shown together with the number of observed events, the expected background and the probability β (see definition in equation 5.43) in table 6.4. The conclusion is that no statistically significant point sources are found in the present analysis. Figure 6.16 shows the the excess parameter for each cell of the grids (defined in section 5.8.1).

zenith [°]	R.A[h]	n_{obs}	b	ξ	β
125.	0.42	8	2.8	2.16	0.94
157.	13.87	7	2.3	2.15	0.82
143.	2.23	8	3.0	1.96	0.92
153.5	14.08	10	4.4	1.89	0.89

TABLE 6.4*: Summary of the four largest excesses found in the grid search. n_{obs} is the number of observed events, b the expected background. For definitions of β and ξ, see text.*

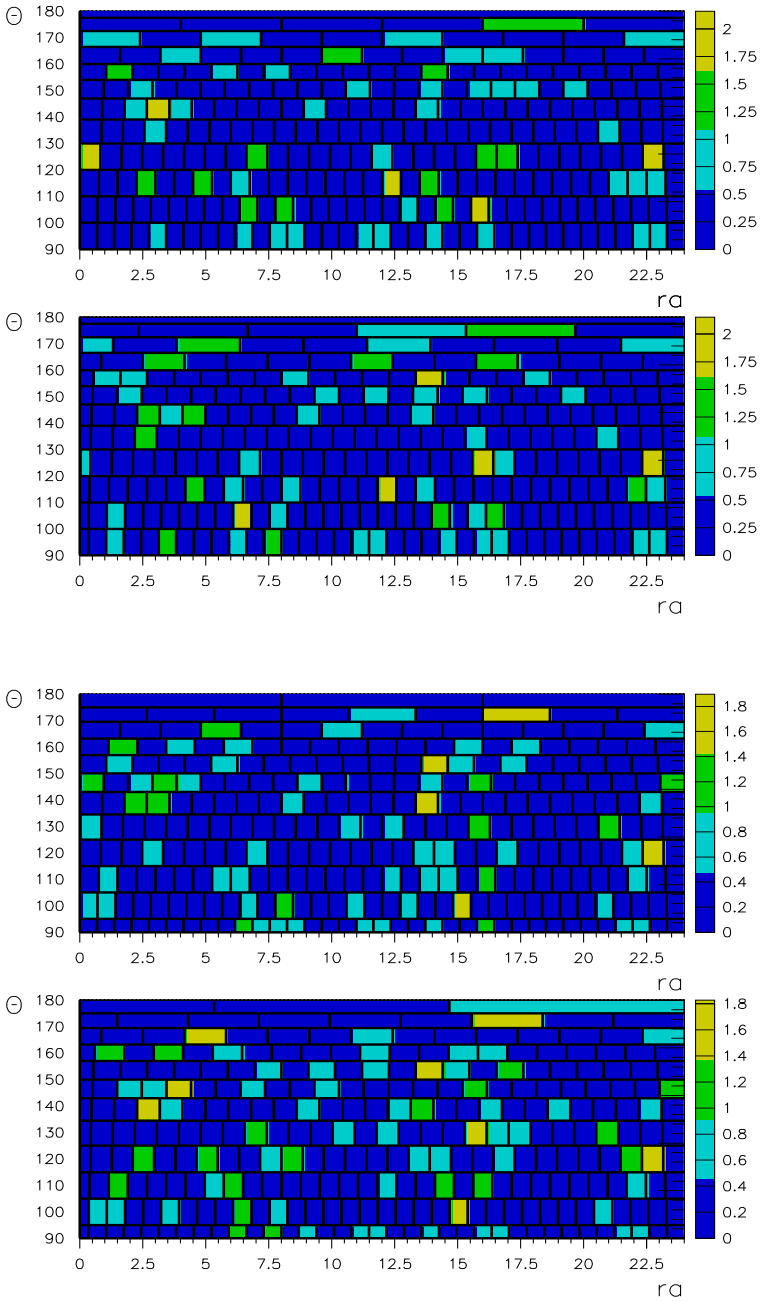

FIGURE 6.16*: The excess parameter for the four grids. Upper two: the lid-grids with a single bin centred on 180°, lower two: the grids with three bins in the upper zenith band. The maximal excess found is ξ = 2.16.*

6.4.3 Detection threshold

An interesting question to ask is, what level of flux would be necessary in order to detect a source with the present analysis ?
From figure 6.15, the size of an excess required to claim the detection of a source can be estimated. Assuming we are willing to claim a source if we would expect an excess larger than the experimentally found in only 1 % of all no-source experiments leads to a required excess parameter of $\xi \simeq 4.75$. This value of the excess parameter fixes the number of observed events, $n_\circ^{\text{source}}$, necessary to detect a source for each zenith band. In order for a flux to be detectable, we will require that it (together with the known background) results in $n_\circ < n_\circ^{\text{source}}$ with less than 10 % probability. This defines a detection threshold: sources below this threshold will not be detected by the all-sky analysis whereas sources above will be detected (with 90 % detection efficiency). The detection threshold is shown together with the sensitivity (see figure 6.12) in figure 6.17. It varies between ~ 7 and $40 \cdot 10^{-7}$ GeV cm^{-2}s^{-1} and differs from the sensitivity by about a factor 3.

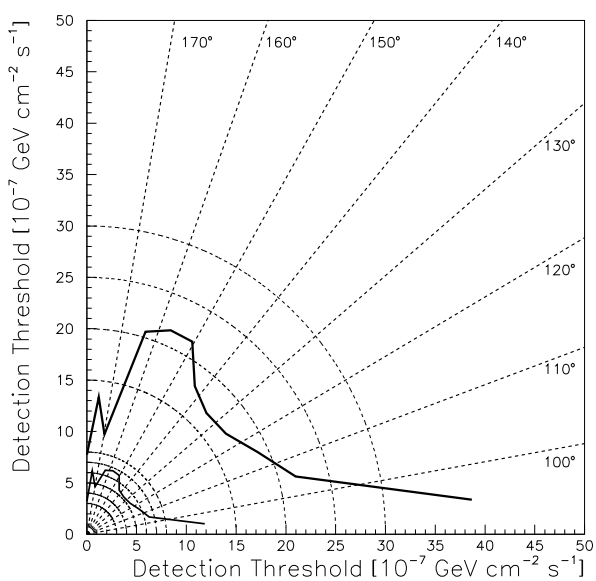

FIGURE 6.17: *The (90 % efficiency) detection threshold for the present analysis. Also shown is the sensitivity (line closer to the origin).*

6.5 Systematic and statistical uncertainties

Since the background for the point source search is estimated from data, the only systematic uncertainty to be considered in the calculation of confidence intervals on the neutrino flux is the uncertainty on the signal efficiency. Once an estimate of the signal efficiency uncertainty has been obtained, it will be included into the limit calculation by folding the function parameterising the uncertainties with the PDF used in the confidence interval construction. Since negative efficiencies are unphysical we will assume a log-normal distribution for the parametrisation of the uncertainties. The reader is referred to part II of this thesis for detailed discussion of the calculational method. The statistical uncertainty of the background estimate and the estimate of the signal efficiency are briefly discussed in a paragraph at the end of this section.

Ice properties and OM sensitivities In section 5.3.3 we discussed briefly the implementation of the ice model into the detector simulation. Problems which arise due to having to use approximations in this implementation are partly remedied by adjusting the absorption length to the experimentally observed time residual distributions.
We will in this study follow a conservative approach: the effect of different implementations of ice properties will be assessed by comparing the FIM implementation and the MAM implementation. The FIM model is built on the ice measurements, the MAM model on fitting to data. The comparison gives us some indication of how the implementation of the ice model affects the estimate of our signal efficiency. We will assume the difference between FIM and MAM to be exclusively due to the ice model implementation. The uncertainty of the absolute level and angular dependence of the OM sensitivity will be considered uncorrelated with this and added in quadrature.
Figure 6.18 shows the difference of the two models. In a crude but conservative approximation we take the maximal found difference for source angles smaller than 180 degrees to give the σ of a log-normal distributed uncertainty on the signal efficiency, i.e. we assume a 20 % uncertainty for zenith angles smaller than 177.5 degrees. For the bin centered on 180 degrees we assume an uncertainty of 40 %.

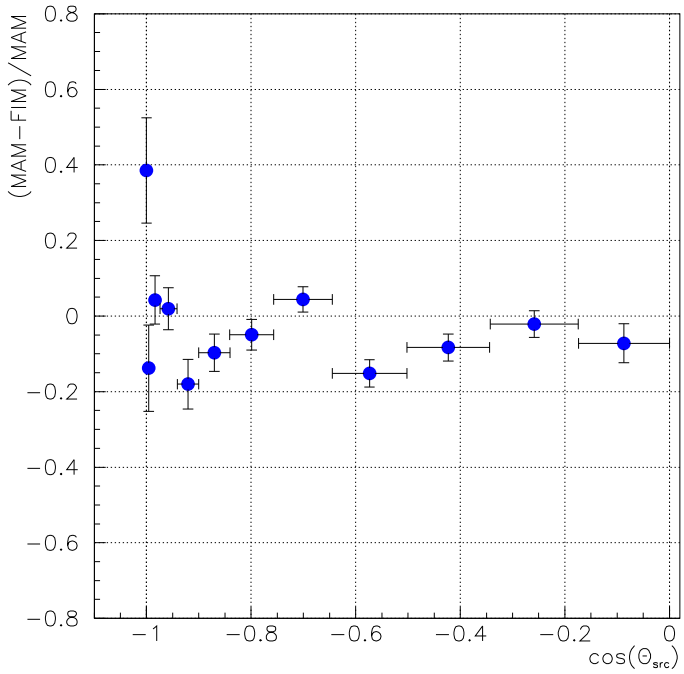

FIGURE 6.18*: The relative difference in signal efficiency between the FIM and MAM implementation of the ice model. The vertical error bars account for the statistical uncertainty in this quantity, horizontal bars for the bin widths.*

The absolute OM sensitivity is a combination of the transmissivity of the glass and gel and PMT specific properties like the quantum efficiency and collection efficiency. These quantities are measurable in the laboratory, but especially the transmissivity might be influenced by ageing of the glass and the gel. We will take laboratory values to estimate of the uncertainties and assume in-situ modifications to be small as compared to those.
The measurements of transmissivity are done on a small number of optical modules and differences between OMs lead us to expect an uncertainty of $\sim$ 10 % whereas measurement uncertainties are negligible [100]. The manufacturer specifications for the uncertainty in the quantum and collection efficiency are 20 % respectively 10 % [101], which we add in quadrature to the uncertainty from the measurements of transmissivity. The overall uncertainty in the OM sensitivity is thererfore estimated to be $\sim$ 25 %. The typical energy of muons from cosmic neutrinos in this analysis is $\sim$ 10 TeV. In [102] it is shown that a 25 % change in the absolute level of sensitivity of all OMs leads to a $\sim$ 10 % change in the rate of muons at these energies. We will therefore assume that the uncertainty in the absolute level of the OM sensitivity adds a 10 % uncertainty on the signal efficiency.
In section 5.3.3 it was mentioned that the refreezing of the water column around the OM leads to additional scattering near the optical module due to air bubbles. This additional scattering would reveal itself mostly by a modification of the angular dependence of the OM sensitivity measured in-ice [70]. The effect has been studied in [103] using the large statistics of down-going muons. The study lead to a modification of the angular response of the OM in the detector simulation in order to reproduce measured (down-going) muon distributions. This modification incorporates uncertainties in the (bulk) ice model and the intrinsic angular dependence of the OMs response as well as the scattering. Since the study was done with an ice-model which is now considered obsolete, the modified angular response can not be viewed as a better representation of the OMs angular response, therefore it has not been used here. However, it can be used as an indication of the uncertainty in our knowledge of the angular sensitivity and [82] showed that the effect of using the two different parameterisations for the angular response of the OM on the efficiency for an E^{-2} signal is $\sim$ 25 %. This uncertainty will be added to the uncertainty originating from the uncertainty in absolute OM sensitivity (10 %, see above) in quadrature, yielding in total a 27 % uncertainty in the signal efficiency due to the imperfect knowledge of absolute OM sensitivity and its angular dependence.

Neutrino-nucleon cross section Uncertainties in the neutrino-nucleon cross section are negligible up to energies of about $Q^2 \sim M_W^2$, see the discussion in section 3.2 and figure 3.2. Above energies of $\sim$ 100 TeV, differences in parameterisations of structure functions are getting increasingly important. As we have seen in the previous section, 90 % of all neutrinos detected in this analysis (assuming an E^{-2} spectrum) have an energy $\lesssim$ 800 TeV. Conservatively, we assume the uncertainty in the neutrino nucleon cross section to be given by the uncertainty at $\sim$ 1000 TeV, which is $\sim$ 15 %, inferred from figure 3.2.

Muon propagation The rate of muons per unit area produced by a cosmic neutrino source depends roughly linearly on the range of the muon, as can be seen from equations 3.13 to 3.15. The present muon propagation simulation is estimated to have an uncertainty in the muon range of 5 - 10 % [104], which we assume to propagate linearly to a 5-10 % uncertainty on the expected rates of muons from cosmic neutrinos. We conservatively assume a 10 % uncertainty in the signal efficiency due to uncertainties in the muon propagation.

Type	Effect on signal eff.	Comments
optical parameters	$\sim$20(40) %	FIM/MAM
OM sens. & air bubbles	$\sim$27 %	[82][100] [101] [102] [103]
Hardware simulation	$\sim$ 5 %	[105]
Timing and geometry	$<$ 2 %	[69][106]
ν cross-section	$\sim$ 15 %	[47]
μ-propagation	$\sim$ 10 %	[104]
Squared sum	39 (51) %	

TABLE 6.5: *Summary of systematic uncertainties. The bracketed values are for the most vertical bin.*

Hardware simulation & calibration A major revision of the detector simulation [105] yielded only a moderate change in the simulated trigger rate for atmospheric muons ($\sim$ 6 %). While this insignficant increase in rate for atmospheric muons (background) can not directly be translated into an rate for high energy neutrinos (signal), it seems reasonable to assume, that the effects of uncertainties in hardware simulations are at least not much bigger for the signal simulation. We will therefore assume the uncertainties to be $\sim$ 5 %.

Uncertainties in the timing calibration (which includes the geometry calibration) are estimated to be of the order of $\sim$ 5 %. [106] has shown that uncertainties of that size affect the signal efficiency by less than 2 %.

Statistical uncertainties Statistical uncertainties originating in the limited statistics of the signal simulation are generally $<$ 5 % except for the three most vertical bins (corresponding to angles larger than 166°) with 6 %, 9 % and 19 % respectively. Except for the most vertical bin they are small compared to the systematic uncertainties discussed in the previous section. The statistical uncertainty on the background estimate is in general of the order of 10 %. However, in the case of few background events in the zenith band, as for the two zenith bands from zenith = 166.5 to 177.5 degrees the statistical uncertainty amounts to $\sim$ 30 %.
One way to treat the statistical uncertainties of the background and signal efficiency estimate is to approximate them to be Gaussian distributed and then treat them analogously to systematic uncertainties using the method described in part II.
This approach will be followed when taking into account the statistical uncertainty for the signal efficiency estimate for the most vertical bin. The statistical uncertainty in the background estimate will be neglected. The justification for neglecting the statistical uncertainty in the background estimate can be found in figure 5 in paper II (see part II). Uncertainties of up to $\sim$ 40 % hardly have any effect on the confidence interval for the relevant levels of background per bin ($\sim$ 2.0) and number of observed events ($\sim$ 1-2).

A remark on neutrino oscillations The results presented here are calculated assuming that no neutrino oscillations are present. This is motivated from the fact that current models of cosmic neutrino production do not take into account neutrino oscillations.
A modification for neutrino oscillations results merely in a multiplicative factor. For current estimates on the oscillation parameters (near maximal mixing, $\delta m^2 \sim 10^3$eV^2) the long baselines ($\sim$ Mpc) over which the neutrinos are observed lead to an approximate equipartition of flavors. The flavor ratio which at the source is ν_e:ν_μ:$\nu_\tau \sim$ 1:2:0 will be 1:1:1 at the detector.

6.6 Flux limits

6.6.1 Grid search

From the number of observed events and the expected off-source bin background, we calculate a 90 % upper limit on the signal flux with a E^{-2} spectrum. The confidence interval calculation is performed using the Feldman & Cousins prescription [96] including the systematic uncertainties in a fashion which is described in detail in part II of this thesis. The limit for each zenith band averaged over right ascension is in general comparable to the sensitivity which is expected in the case of no or few sources. Figure 6.19 exemplifies this for one of the four grids.
Figure 6.20 presents the neutrino limits for each of the grid cells. Muon flux limits can be obtained from these multiplying the neutrino limits by the ratio of the respective effective areas, see figure 6.9.

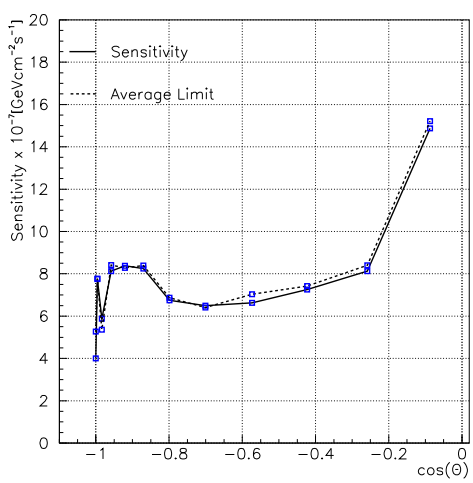

FIGURE 6.19: *The estimated sensitivity (solid line) compared to the average limit obtained for each zenith band (dashed line) in the lid grid*

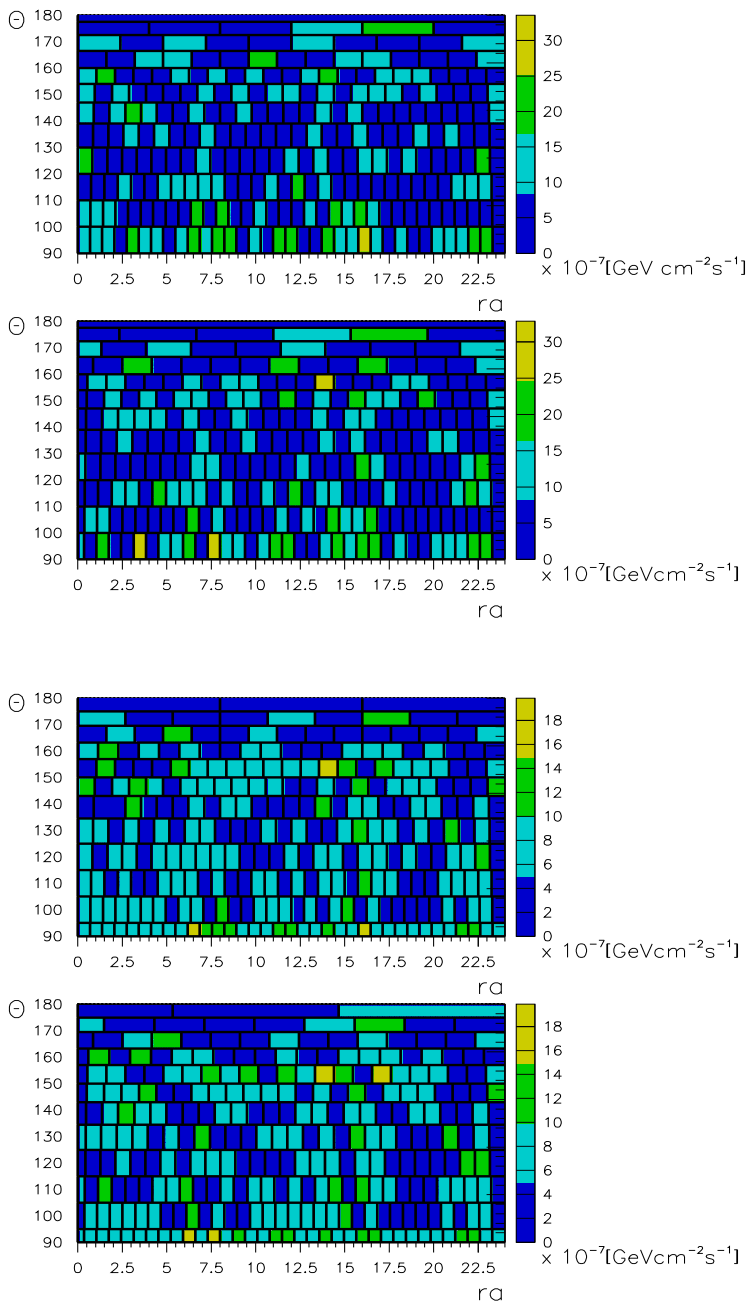

FIGURE 6.20*: The neutrino flux limits for each cell of the four grids. Note for the zenith band at horizon, that the bin size is only half of the bin size in the null grid, therefore the relatively bad limits for this band.*

6.6.2 Selected sources

Table 6.6 summarises the limits on the muon and neutrino flux for 20 pre-selected sources. The most stringent upper limit is for the TeV blazar 1ES

Candidate	Dec [$\circ$]	R.A. [h]	n_{obs}	b	Φ^{ν}_{90}	Φ^{μ}_{90}
TeV Blazars						
Mrk 421	38.2	11.07	2	2.92	3.7	3.2
Mrk 501	39.8	16.90	4	2.99	7.6	6.5
H 1426+428	42.7	14.48	0	2.60	1.2	1.0
1ES 2344+514	51.7	23.78	3	1.88	8.7	6.4
1ES 1959+650	65.1	20.00	1	2.92	2.7	1.7
3C 66A	42.9	2.38	4	2.48	9.1	7.1
GeV Blazars						
QSO 0528+134	13.4	5.52	2	2.05	7.3	8.6
QSO 0235+164	16.6	2.62	1	2.02	4.1	4.8
QSO 1611+343	34.4	16.24	7	2.52	16.6	14.2
Microquasars						
SS 433	5.0	19.20	0	0.98	13.5	19.9
GRS 1915+105	10.9	19.2	1	1.73	5.4	6.5
GRO J0422+32	32.9	4.36	1	2.60	2.4	2.0
Cygnus X1	35.2	19.97	2	2.64	4.6	3.9
Cygnus X3	41.0	20.54	2	2.49	5.2	4.0
XTE J1118+480	48.0	11.30	1	2.71	2.2	1.7
Ci Cam	56.0	4.33	5	2.49	12.5	9.2
LS 1 +61 303	61.2	2.68	2	2.87	4.6	4.3
SNRs						
SGR 1900+14	9.3	19.12	1	1.44	6.6	9.9
Crab Nebula	22.0	5.58	3	2.18	9.2	9.0
Cassiopeia A	58.8	23.39	5	2.50	10.4	6.9

TABLE 6.6: *Neutrino and muon flux limits on selected sources in units of 10^{-7}GeVcm^{-2}s^{-1} (neutrino flux) and 10^{-15}cm^{-2}s^{-1} (muon flux). The muon limits are calculated for a neutrino spectrum $\propto E_{\nu}^{-2}$ and integrated above E_{ν} = 10 GeV.*

1426+428 with 1.2 $\cdot 10^{-7}$GeV cm^{-2}s^{-1}. This stringent limit is due to a downward fluctuation of the background. The limit is a about a factor 5 below the sensitivity at that zenith angles.

For the GeV blazar QSO 1611+343, we find 7 events over a background of 2.52, which results in a two sided confidence interval with $1.1 < \mu_s < 13.50$

(including systematic uncertainties). This should not be confused with having detected a source. Following a similar reasoning as presented in the previous section, we would require at least 10 events over an expected background of 2.52 for the detection of a source. Therefore, we present here only the upper limit of the interval.

6.7 Discussion & outlook

Figure 6.21 shows the sensitivity (including systematic uncertainties) and the detection threshold achieved in the present analysis together with a number of current models for cosmic neutrino production (see section 2, figure 2.3 for reference). As can be seen the sensitivity of the present analysis is roughly 1 - 2 order of magnitudes from the most optimistic models for AGN neutrino production. A previous point source search performed in 1997 with essentially the same detector configuration [82] has achieved a sensitivity which at best is about a factor 1.7 worse [1] than the one achieved in the present analysis.
Of course there are aspects of the present analysis, which could be improved. A single most significant improvement would be the implementation of a SVM which can treat weighted events, making it possible to optimise on a E^{-2} neutrino spectrum, which would probably improve the sensitivity by about 15 % (see figure 5.15 in section 5).
It is obviously unfeasible to test all possible combinations of variables as input to the SVM, so there might be a combination which yields better results. We tested 5 sets of variables which have been preselected for separation power and chose the one with the best performance. It seems difficult to think of additional combinations which lead to major improvements.
The sensitivity shown in figure 6.21 is not strictly valid for the whole zenith range. For example, in the zenith range below 100 degrees the sensitivity rises by a factor of 2, and for the zenith range between 140 and 160 degrees it rises by about a factor 1.2. For the very shallow angles, it will be difficult to achieve a strong improvement, a possible suggestion might be to remove the initial cut on the zenith of the first reconstruction, but no big effects are expected [2]. A detailed study of the background between 140 and 160 degrees is necessary to achieve an improvement in these region, but is not expected to lead to an improvement by more than 20 %.
The presence of a $\sim$ 40 % systematic uncertainty on the signal efficiency leads to roughly a 20 % worse sensitivity with respect to what would have been obtained without uncertainties. To get an improvement in the sensitivity by trying to reduce the systematic uncertainty is difficult: to reduce the effect on the sensitivity to 10 % for example would require an improvement of our knowledge of the signal efficiency by about 20 %.
The AMANDA-B10 detector has been operational from 1997-1999, thus a large improvement will be achieved by combining those years. Since in the

[1] recall that worse means higher sensitivity
[2] for AMANDA-II the larger lever arm for shallow angles leads to a significant improvement

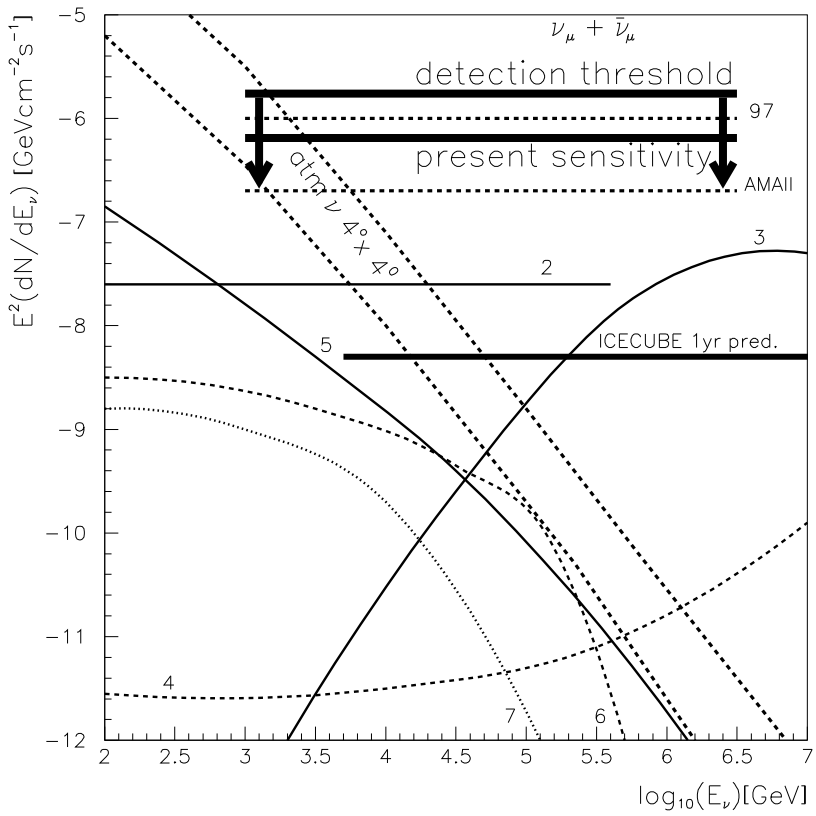

FIGURE 6.21*: The 90 % confidence level sensitivity and the detection threshold compared to a variety of cosmic neutrino source models (see figure 2.3 for reference). The sensitivity and detection threshold is here averaged over zenith angles between 110° and 150° degrees. Also included are the sensitivities achieved by analyses of the data taken with the AMANDA-B10 array in 1997 [82], the AMANDA-II array in 2000 [84] and the predicted sensitivity for the IceCube detector [15].*

background dominated domain the sensitivity scales with $\sqrt{T_{live}}$, an improvement by atbetween a factor 1.7 and 3 can be expected.
It should be mentioned that the 19 string array AMANDA-II has been operational since 2000. With this array a point source search has been performed for data taken in 2000 [84].
This analysis, which strategically is rather similar to the one presented in this thesis, results in a sensitivity which is about a factor 3 smaller than the one of the present analysis. AMANDA-II data taken in the years 2000 to 2002 is currently being analysed. Combining the B10 analyses of the years 1997-1999 with the AMANDA-II analyses of 2000-2002 will conservatively yield a sensitivity within a factor 2 of the most optimistic predictions of cosmic neutrino production. The sensitivity of IceCube is predicted to be sufficient to rule out or confirm models of AGN production [15] (see figure 6.21).

Part II

A method to incorporate systematic uncertainties in the calculation of confidence intervals

CHAPTER 7

Introduction

Often the goal of experiments in physics is to estimate the parameters of a probability density function (PDF) from which experimental results are drawn. Apart from the estimate of the parameter, one must also give the corresponding uncertainty in order to judge the quality of an experimental result. This uncertainty is quantified in terms of *confidence intervals* and *confidence levels*. For a given confidence interval, the higher the confidence level, the more reason to believe that the true value lies within the interval. Vice versa, for a given confidence level, the smaller the confidence interval the more precise estimate of the parameter has been obtained. Generally, confidence intervals should include statistical as well as systematic uncertainties. A method to include systematic uncertainties into the calculation of confidence intervals is the main subject of this part of the thesis. The part is organised as follows: the next chapter gives a short review of the statistics of confidence intervals as they are used in particle physics. Section 9 is devoted to a summary of the four papers in which the method is developed (papers I & II), its statistical properties are examined (paper III) and its technical implementation is documented (paper IV). The final section gives a short discussion and an outlook.

CHAPTER 8

Confidence intervals in particle physics

Within mathematical statistics there are two fundamentally different approaches to probability which reflect themselves in the way confidence intervals are calculated. On the one hand there is Bayesian statistics. Here probability is defined as "degree of belief". Given a confidence interval $[s_1, s_2]$, there is a certain degree of belief that the true value of the parameter lies within the interval. This degree of belief is called the *confidence level*, denoted as 100(1-α)%, where common choices of α are 0.1, 0.05 or 0.01.
Mathematically, this definition of probability allows to calculate the confidence intervals in terms of the likelihood function for different hypothesis under condition of the observed data:

$$1 - \alpha = \int_{s_1}^{s_2} P(s|n_\circ) d\, s \tag{8.1}$$

Here $P(s|n_\circ)$ is the likelihood for parameter s, given the observation $n_\circ$.
On the other hand, there is the frequentist approach to probability. Here probability is defined in terms of repeated experiments. The probability for the outcome $n_\circ$ in a given experiment is:

$$P(n_\circ|s) = \lim_{N\to\infty} \frac{N^{\text{exp}}_{n=n_\circ}(s)}{N} \tag{8.2}$$

where N is the total number of experiments, $N^{\text{exp}}_{n=n_\circ}$ is the number of experiments which result in the measurement $n_\circ$ and s is the parameter of the PDF. Since in frequentist statistics the parameter of the PDF is fixed (although unknown) it can not be treated as a random variable unless it is possible to define

it in terms of repeated experiments. An integration in hypothesis space (as given in equation 8.1), therefore does not make sense. Obviously, this makes calculation of confidence intervals much more complicated, since still the goal remains to make statements about the probability of hypotheses.

Neyman [107] proposed in 1937 a scheme to construct confidence intervals without having to integrate the likelihood function (see paper II for a detailed description of this algorithm). Instead of making statements about the probabilities of hypotheses, statements are made about the set of intervals which is obtained from an ensemble of repeated experiments. The construction seeks to calculate confidence intervals which are members of a set which contain the true value of the parameter in $100(1-\alpha)\%$ of all cases. If the construction succeeds the resulting intervals are said to have *correct coverage*. In other words, given the true value of the parameter s_{true}, $100(1-\alpha)\%$ of all experiments will give a confidence interval which includes s_{true}. Since we do not know the true value, the algorithm has to fulfill this requirement for all possible values of s.

One feature of the Neyman construction is, that it has to be chosen in advance whether a discovery is going to be announced or whether an upper limit will be reported. In practice, this choice will be made based on the observation. For example, an experimentalist who detects a large excess will not be willing to report an upper limit, on the other hand, one can not report a discovery if the number of events is compatible with the expected background.

This constitutes a problem of the Neyman construction, since it distorts the ensemble of experiments which is used to construct the confidence intervals in the sense that the requirement of correct coverage is no longer fulfilled.

A solution to this problem has been (re-)discovered in 1998 by Feldman & Cousins [96]. This scheme is based on the likelihood ratio hypothesis test [108], where for each possible pair s, n of parameter and experimental outcome the ratio between the likelihood for the tested s and the likelihood for the parameter s being most compatible with the observation n is calculated and then used in the construction of the confidence interval. It turns out that in this scheme, confidence intervals switch from one sided (upper limits) to two sided (discovery) by construction, hence preserving correct coverage. This scheme will be referred to as *likelihood ratio scheme*.

However, also the likelihood ratio scheme has one major drawback. Consider a Poisson process with known background. If the number of observed events is significantly below the expected background, the reported limit will be more stringent than in the case that an experiment has observed a number of events compatible with background. While this is consistent with frequentist statistics (as long as what is detected is a downward fluctuation of the background), it is

often considered counter-intuitive and undesirable. Other schemes have been proposed to solve this problem by normalizing the distribution of events taking into account the fact that the number of background events cannot have been larger than the number of events actually observed [109]. It has however been shown (for example in paper III) that those schemes do not fulfill the requirement of correct coverage and can therefore not be recommended. This method will be referred to as *likelihood ratio scheme with conditioning*.

The likelihood ratio theme is the present standard in particle physics. The problems with frequentist intervals presented above are absent in Bayesian statistics, so a reasonable question is why not Bayesian statistics is chosen instead. The reasons are mainly philosophical. Apart from the fact that s should not be treated as a random variable (unless definable in terms of repeated experiments) in general the function $P(n|s)$, i.e. the probability of making an observation n given the hypothesis s is known, whereas what we like to know is the function $P(s|n)$. To go from the former to the latter Bayes' theorem has to be applied, which states that $P(s|n) \propto P(n|s) \times P(s)$. This means, the a priori probability, $P(s)$ of the hypotheses has to be known or assumed, introducing a certain amount of subjectivity or bias.

This far the statistics of confidence intervals have been discussed from a standpoint where there are no experimental uncertainties or where they are negligible with respect to the statistical uncertainties.

CHAPTER 9

Summary of the papers

Consider the case in which a confidence interval is to be constructed for the parameter s of a PDF $P(n|s,\epsilon)$, where the experimental outcome depends not only on s, but also on another parameter[1], here called ϵ. Since the task is primarily to constrain s, this parameter will be referred to as *primary parameter*, parameters such as ϵ will be referred to as *nuisance parameters*. Nuisance parameters are the parameters in which systematic uncertainties are present, for example the experimental detection efficiency or the background prediction.

9.1 Bayesian method and algorithm (paper I)

Paper I describes the first attempts to solve the problem of including systematic uncertainties in the calculation of confidence intervals. The main idea is a convolution of the PDF representing the statistical process with a PDF parameterising the the systematic uncertainties in the nuisance parameters, or more formally:

$$P(n|s,\epsilon) \rightarrow \int P(n|s,\epsilon')P(\epsilon'|\epsilon)d\epsilon' \tag{9.1}$$

here the integration is performed over an interval suitable for the range of the nuisance parameter. This way of treating systematic uncertainties is Bayesian, since the integral is in all possible true values of ϵ' given the assessment ϵ.
This method is therefore a natural extension of the Bayesian method to calculate confidence intervals which was recommended by the PDG before 1998 [110]. In paper I, building on [111], a Monte Carlo algorithm is described performing the PDG calculation with a PDF like the one given in equation 9.1,

[1] one additional parameter is assumed for simplicity.

i.e. a convolution of the statistical process (a Poisson process) and a PDF describing the uncertainties. The method takes into account uncertainties in the background prediction with a Gaussian parameterisation and uncertainties in the effective area (signal efficiency) with a flat or Gaussian parameterisation. Several applications of this method are discussed and a first attempt at the fusing of the Bayesian treatment of the uncertainties with a frequentist construction of confidence intervals is presented. It is speculated about the differences in the two different implementations (PDG and frequentist construction).
Since the PDG method is currently disfavoured (see discussion in the previous section), after having completed this note we focused entirely on frequentist confidence interval calculation.

9.2 The generalized Cousins & Highland method (paper II)

In 1992, a method was presented by Cousins & Highland [112] which included a Gaussian uncertainty in the signal efficiency in a Neyman construction of confidence intervals by replacing the Poisson distribution describing the physical process by the convolution given in equation 9.1. The combination of the frequentist treatment of the primary parameters and the Bayesian treatment of the nuisance parameters is often referred to as *semi-Bayesian*. In paper II the method proposed in [112] is generalized to take into account uncertainties in the prediction of background processes, uncertainties in the signal detection efficiency and background efficiency and to allow for a correlation between the signal and background detection efficiencies. Furthermore, the method is implemented with the (currently recommended) likelihood ratio scheme with and without conditioning. The generalized method utilizes Monte-Carlo integration which makes implementation of other parameterisations of uncertainties simple. This method will be referred to as Generalized Cousins-Highland (GCH) method.
Figures 4 and 5 of paper II show the effect of introducing uncertainties in the signal and background efficiencies into the interval calculation for different combinations of background expectation and number of observed events. A general result is that the confidence interval becomes wider with increasing uncertainties. However, in cases where there are significantly less events observed than expected from background, the interval's width decreases with increasing uncertainty for the likelihood ratio scheme. Examples for this behaviour are given in table 3 of paper II. In cases where negative values of

the nuisance parameter are unphysical (like for example in case of detection efficiency), it might be reasonable to choose a log-normal distribution for describing the uncertainties instead of a truncated Gaussian distribution. This choice seems to have little effect on the confidence interval for uncertainties smaller than $\sim 40\%$.

The GCH method is compared to an approximative calculation. Assuming a Gaussian uncertainty, the logarithm [2] of the likelihood ratio between the likelihood for the outcome under the present hypothesis and the likelihood under the hypothesis which best explains the data forms a χ^2 distribution, which can be converted into confidence limits. It is found, that the intervals found by the χ^2 approximation generally are larger, implying that they are more conservative (for a given ensemble of experiments).

The most important property of confidence intervals is the coverage (see previous section). A first attempt is made in paper II to calculate the coverage of the GCH intervals. Two different ensembles are considered: an ensemble where the nuisance parameters are fixed at the nominal (estimated) value and one ensemble where the true value of the nuisance parameter is varied according to a Gaussian PDF centered on the estimated value of the nuisance parameter. With respect to the former ensemble, the presented method leads to increasing over-coverage with increasing uncertainties. With respect to the latter there is no over-coverage (except for the unavoidable over-coverage caused by the discrete nature of the Poisson distribution). It is noted that both ensembles can only be seen as approximations to the ensemble with respect to which coverage should be preserved: the one where the nuisance parameter should be *measured* for each experiment

Two applications are presented from high energy neutrino astrophysics to illustrate the importance of including systematic uncertainties in the calculation of confidence intervals. The AMANDA neutrino telescope has recently published limits on cascades from the diffuse flux of cosmic neutrinos in the energy range between 5 TeV and 300 TeV [11]. Based on zero detected events compared to an expected background of 0.01 events, the 90 % confidence level was calculated. The background expectation is based on Monte Carlo simulations which are estimated to have a 30 % Gaussian uncertainty. The systematic uncertainty of the signal efficiency was estimated from detector simulations to be Gaussian and $\sim$ 25 %. Using the GCH method to include systematic uncertainties the finally published limit is about 10 % higher than it would have been if the systematic uncertainties were negligible.

[2] in equation 9 of paper 2 the logarithm unfortunately has been lost.

Another example concerns results published by AMANDA on searches for super-symmetric dark matter in the form of weakly interacting massive particles (WIMPS) [13]. Here the uncertainties in signal efficiency are estimated to range from 10 % to 25 % depending on the assumed signal spectrum. Correlated with signal detection efficiency there is an additional detection efficiency uncertainty for the background, estimated to be $\sim$ 20 %. Finally, the uncertainty in the overall normalization of the atmospheric neutrino flux (which constitutes the background) has to be added. The final limit including systematic uncertainties can be seen in figure 14 of paper II.

9.3 The coverage of the GCH method (paper III)

From a frequentist point of view, an algorithm is said to have the correct *coverage* if, given a confidence level $100(1-\alpha)$% and a large number of repeated identical experiments, it provides correct answers in $100(1-\alpha)$% of the cases, independent of the value of s. In paper III, the coverage of the method developed in paper II is studied using two different approaches. One approach considers an ensemble strictly in accordance with above stated definition of coverage, i.e. an ensemble consisting of *identical* experiments. In this case, the coverage can be calculated analytically. In the other approach, the definition is modified to hold for similar experiments, meaning for an ensemble of experiments with varying nuisance parameters. Calculations of coverage for this ensemble have been done using Monte Carlo simulations. Figure 1 in paper III shows the identical-ensemble-coverage for the likelihood ratio scheme. Flat, Gaussian and log-normal parameterisations of systematic uncertainty are investigated for different sizes of the uncertainties. Apart from the see-saw behaviour of the coverage which is caused by the discrete nature of the Poisson distribution, the coverage is constant with signal expectation. Generally the likelihood ratio scheme leads to over-coverage even without uncertainties. The GCH method causes increased over-coverage, especially for higher signal expectations. The effect is smaller for a flat parameterisation than for Gaussian and log-normal distributions.

Figure 2 in paper III shows the same for likelihood ratio scheme with conditioning applied. It is noteworthy, that introducing conditioning leads to under-coverage for certain signal expectations also without uncertainties. Otherwise, inclusion of uncertainties has similar effects as in the case of likelihood ratio scheme without conditioning.

Figure 3 of paper III shows the mean coverage for a similar-experiments-

ensemble, where the mean has been taken over different signal expectations and constant background expectation. Here the true efficiency is drawn from a Gaussian distribution for each experiment. With respect to this ensemble no additional over-coverage is introduced.
A realization of the similar-experiments ensemble could be an ensemble of experiments in which the detector is "rebuilt" with as a result slightly different efficiencies for each repetition. However, in particle physics the ensemble is one, where the true efficiency is fixed but unknown, but where the assessment of the efficiency is uncertain. To represent this ensemble by Monte Carlo, the *measured* efficiency has to be drawn from a distribution for each experiment. Since in this case the construction has to be performed for each Monte Carlo experiment, the implementation of this test is computationally more cumbersome. Preliminary studies presented in paper III reveal an increase of coverage from 92 % to 94 % for two different signal expectations (true signal equals 3 and 6, no background) which seems to indicate that the GCH method leads to moderate over-coverage with respect to this ensemble.

9.4 A routine for confidence interval calculation (paper IV)

Paper IV gives a technical summary and serves as a short user manual for the FORTRAN routine which has been developed to perform the confidence interval calculations described in the preceding sections.

CHAPTER 10

Outlook

The method to incorporate systematic uncertainties in the calculation of confidence intervals is convenient, has well defined statistical properties and gives intuitive results for most cases. The few cases, where the method gave counter-intuitive results (smaller intervals with increasing uncertainties), inspired [113] to suggest a modification to the method where the averaging over the nuisance parameters is only done in the numerator of the likelihood ratio, whereas the denominator is maximised with respect to the nuisance parameters. While this method gives intuitive results in all tested cases, it is argued here that the suggested modification is at best only half way to a better, fully frequentist method.

Within the theory of likelihood ratio hypothesis testing nuisance parameters are included by maximising both the numerator and the denominator of the likelihood ratio. This is the so called profile-likelihood method, which constitutes a fully frequentist method to treat systematic uncertainties, see [108]. Thus, it is realized that the suggested modification is a hybrid between the method treating the systematics in a Bayesian way and a fully frequentist treatment of the nuisance parameters. Conceptually, this is unsatisfactory: in the original method the nuisance parameters are treated in a Bayesian way, whereas the primary parameter is treated in a frequentist way.

To get rid of the conceptual ambiguities present also in the method presented in papers II and III, the profile likelihood method seems to be the next step. This method is so far largely unexplored within the particle physics community, though there are claims [114] that it provides correct coverage in all cases. Certainly, conclusive result on the profile likelihood method require further investigation.

Part III

AMANDA-II and neutrino oscillations

CHAPTER 11

11.1 Introduction

In this chapter an assessment of the sensitivity of AMANDA-II to neutrino oscillations in the beam of atmospheric neutrinos is presented. This work was performed prior to the actual completion of AMANDA-II, therefore relies on detector simulations incorporating the best knowledge about the AMANDA-II detector at that point. The work presented here is based on two AMANDA internal notes [115] and [116], here we will give a short summary only.

In the approximation that only two neutrino flavors mix with each other, the probability that a neutrino ν of flavor i (e,μ,τ) will turn into one of a different flavor i' is given by:

$$P(\nu_i \rightarrow \nu_{i' \neq i}) = \sin^2 2\theta \, \sin^2 \left(1.27 \, \Delta m^2 \frac{L(\mathrm{km})}{E_\nu(\mathrm{GeV})} \right) \tag{11.1}$$

θ being the mixing angle, Δm^2 the squared mass difference in eV^2 of the two mass eigenstates that build the flavor state, L the distance of the source to the detector and E_ν the neutrino energy. Any experiment covering a range of values of E and/or L should therefore be able to measure the mass difference.

11.2 Neutrino oscillations in AMANDA-II using contained events

In a first study, we concentrated on atmospheric neutrino induced muons completely contained in the AMANDA fiducial volume. For contained events, in

principle, a calorimetric measurement of the neutrino energy should be possible by exploiting the relation between the total light yield and the number of OMs with a hit:

$$E_\nu = a \times N_{\text{om}} + b \tag{11.2}$$

The energy resolution will in this case be given by the statistical uncertainty in the number of OMs with a hit, i.e. $\propto \sqrt{N_{\text{om}}}$.
The energy resolution was in this study determined by simulating contained muons in a generic AMANDA-II detector with 20 strings. The simulated detector consisted of the (at that time already existing) B10 core and 10 additional strings. Three different spacings of OM were simulated for these additional strings (10, 15 and 20 m).
The energy resolution for contained muons was found to be:

$$\frac{\sigma(E_\mu)}{E_\mu} \sim \frac{2}{\sqrt{E_\mu}} \tag{11.3}$$

For neutrinos the resolution will be even worse, since due to its localised topology of the hadronic shower only contributes insignificantly (with ~ 1 hit) to the multiplicity [1].
Even assuming it would be possible to achieve a similar resolution for the neutrino as for the muon, it was found that (with oscillation parameters $\Delta m^2 = 2.2 \cdot 10^{-3}\text{eV}^2$ and $\sin^2\theta = 0.9$) the resolution is not sufficient to allow a mapping of the energy spectrum.
In a next step, we calculated analytically the number of contained events in the AMANDA detector in order to assess the possibility of performing a counting experiment. This is done by integrating the equation:

$$\frac{dN_\mu}{dE_\nu} = \phi_\nu(E_\nu) P(\nu_i \to \nu_{i' \neq i}) \times \frac{1}{2}\left(\frac{d\sigma_{\nu N \to \mu X}}{dE_\mu} + \frac{d\sigma_{\bar{\nu} N \to \mu X}}{dE_\mu}\right) \times \rho N_a \times \Delta t \times L_\mu^{\text{eff}}(E_\mu) \times \Delta A \tag{11.4}$$

where ϕ_ν is the neutrino flux, σ the differential (anti)neutrino-nucleon cross section, Δt is the running time, ρ is the ice density, N_a ,Avogadro's number and $L_\mu^{\text{eff}}\,\Delta A$ is the geometrical volume for contained events. $P(\nu_i \to \nu_{i' \neq i})$ is equal to unity for the case of no oscillations and given by equation 11.1 in case of oscillations.
The integration boundaries are determined by the lower energy threshold for muon detection and the containment requirement. The result is shown for some selected muon detection thresholds in table 11.1 For a comparatively

[1] however, this hit might have a large ADC

E_μ° (GeV)	N_{events}	$N_{\text{events}}^{\text{osc}}$
10	73	37
20	28	10
30	14	2.5
40	8	0.7

TABLE 11.1*: Number of contained events with and without flavor oscillations in a 9 month exposure of AMANDA-II.*

low threshold of $E_\mu^\circ \sim 20$ GeV there is a 3 σ effect. Note, however, that we did not include detection efficiency into the calculations and since count rates are very low, detecting sufficient statistics of contained events seems a difficult if not impossible task.

11.3 Neutrino oscillations in AMANDA-II using zenith angle distribution

In the previous section, the sensitivity to neutrino oscillations was assessed concentrating on contained events. Since the probability for oscillations depends on the path length from the production site of the neutrino to the detector, the zenith distribution of atmospheric neutrinos in AMANDA should be influenced as well. In this section we study the sensitivity of a 19 string AMANDA-II detector towards a distortion of the angular spectrum of atmospheric neutrino induced muons. The analysis proceeds as follows:

- The distribution of reconstructed zenith angle, Θ, is weighted with the corresponding oscillation probability, see equation 11.1. Here it should be noted that the path-length, L, depends on the zenith angle. This is done for a grid of 30×50 points in the $(\sin^2\Theta_m, \Delta m^2)$ plane.

- for each point in the $(\sin^2\Theta_m, \Delta m^2)$ plane we randomly draw 100 pseudo-measurements from a Poisson distribution.

- a χ^2 is calculated for the two distributions normalised to each other in

an angular range $\Theta > 110°$:

$$\chi^2 = \sum_i \frac{(n_i^{\text{osc}} - n_i^{\text{noosc}})^2}{n_i^{\text{noosc}}} \tag{11.5}$$

The detector was considered sensitive to a certain combination of oscillation parameters if the χ^2 was bigger than the χ^2 corresponding to 90 % (95 %, 99 %) confidence levels in 80 % of all pseudo-measurements.
Since the AMANDA-II efficiency for atmospheric neutrino detection was unknown we repeated the above procedure for a couple of assumptions on the efficiency. Figure 11.1 shows the sensitivity contour for the full level 2 efficiency for atmospheric neutrinos as well as the sensitivity contour assuming a reduction to 20, 30 and 40 % of the efficiency at level 2. Since the year 2000 AMANDA-II is operational. It is impossible to directly compare the predictions made in this study with the atmospheric neutrino efficiency reached in the real detector. For example, we simulated a detector with trigger threshold of 18 hits, whereas the real AMANDA-II threshold is set to 24. The loss in efficiency for low energy events caused by the high trigger threshold affects especially the sensitivity to neutrino oscillations since they are most effective at low energies. Also we assumed efficiencies with respect to a level 2 pre-trigger, which was inspired by the B10 analysis. The AMANDA-II level 2 actually used is different from the assumptions we made in this study. The AMANDA-B10 efficiency for atmospheric neutrinos with respect to level 2 was about 10 %, thus clearly below the efficiency necessary to be sensitive to neutrino oscillations. For AMANDA-II it is most probably not much larger than that.

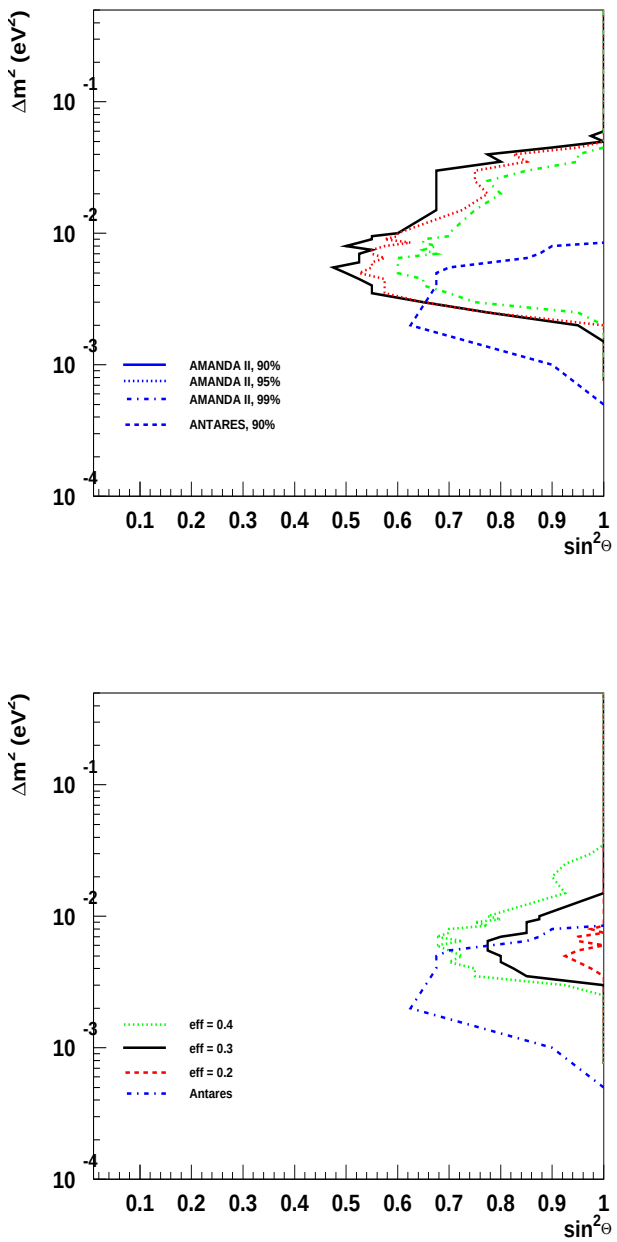

FIGURE 11.1: *The 90 % (95 %,99 %) confidence level sensitivity regions for AMANDA-II with efficiency comparable to the level 2 efficiency (upper) and the level 2 efficiency reduced to 20, 30 and 40 % (lower). Also included is the sensitivity that ANTARES claims to have [117] based on Monte Carlo simulations*

References

[1] "Kungliga Ventenskapsakademiens pressmeddelande: Nobelpriset i fysik, 2002", http://www.kva.se/.

[2] G. Galilei, "Sidereus Nuncius", Venice, Italy (1610).

[3] W. Wendker, "Astronomie und Astrophysik", VCH Verlag, Hamburg, Germany (1990).

[4] J. G. Learned and K. Mannheim, "High-energy neutrino astrophysics", *Ann. Rev. Nucl. Part. Sci.* **50** (2000) 679–749.

[5] J. W. Cronin, S. P. Swordy, and T. K. Gaisser, "Cosmic rays at the energy frontier", *Sci. Am.* **276** (1997) 32–37.

[6] **BAIKAL** Collaboration, B. K. Lubsandorzhev, "The Lake Baikal neutrino experiment: Present status and future prospects", *Nucl. Instrum. Meth.* **A502** (2003) 145–149.

[7] **AMANDA** Collaboration, E. Andres *et al.*, "Observation of high-energy neutrinos using Cerenkov detectors embedded deep in Antarctic ice", *Nature* **410** (2001) 441–443.

[8] **AMANDA** Collaboration, J. Ahrens *et al.*, "Observation of high energy atmospheric neutrinos with the Antarctic Muon and Neutrino Detector Array", *Phys. Rev.* **D66** (2002) 012005, `astro-ph/0205109`.

[9] **AMANDA** Collaboration, J. Ahrens *et al.*, "Search for point sources of high energy neutrinos with AMANDA", *Astrophys. J.* **583** (2003) 1040–1057, `astro-ph/0208006`.

[10] **AMANDA** Collaboration, J. Ahrens *et al.*, "Limits on diffuse fluxes of high energy extraterrestrial neutrinos with the AMANDA-B10 detector", *Phys. Rev. Lett.* **90** (2003) 251101, `astro-ph/0303218`.

[11] **AMANDA** Collaboration, J. Ahrens *et al.*, "Search for neutrino-induced cascades with the AMANDA detector", *Phys. Rev.* **D67** (2003) 012003, `astro-ph/0206487`.

[12] **AMANDA** Collaboration, R. Hardtke *et al.*, "The AMANDA search for high energy neutrinos from gamma-ray bursts", *AIP Conf. Proc.* **662** (2003) 150–152.

[13] **AMANDA** Collaboration, J. Ahrens *et al.*, "Limits to the muon flux from WIMP annihilation in the center of the earth with the AMANDA detector", *Phys. Rev.* **D66** (2002) 032006, `astro-ph/0202370`.

[14] **AMANDA** Collaboration, P. Niessen *et al.*, "Search for relativistic monopoles with the AMANDA detector", Prepared for 27th International Cosmic Ray Conference (ICRC 2001), Hamburg, Germany, 7-15 Aug 2001.

[15] **IceCube** Collaboration, J. Ahrens *et al.*, "Sensitivity of the IceCube detector to astrophysical sources of high energy muon neutrinos", `astro-ph/0305196`.

[16] T. Kajita and Y. Totsuka, "Observation of atmospheric neutrinos", *Rev. Mod. Phys.* **73** (2001) 85–118.

[17] T. K. Gaisser, F. Halzen, and T. Stanev, "Particle astrophysics with high-energy neutrinos", *Phys. Rept.* **258** (1995) 173–236, `hep-ph/9410384`.

[18] T. K. Gaisser and M. Honda, "Flux of atmospheric neutrinos", *Ann. Rev. Nucl. Part. Sci.* **52** (2002) 153–199, `hep-ph/0203272`.

[19] M. Honda, T. Kajita, K. Kasahara, and S. Midorikawa, "Calculation of the flux of atmospheric neutrinos", *Phys. Rev.* **D52** (1995) 4985–5005, `hep-ph/9503439`.

[20] L. V. Volkova, "Energy spectra and angular distributions of atmospheric neutrinos", *Sov. J. Nucl. Phys.* **31** (1980) 784–790.

[21] K. Mitsui, H. Komori, and Y. Minorikawa, "Energy spectrum of cosmic ray neutrinos in the atmosphere", *Nuovo Cim.* **C9** (1986) 995–1020.

[22] A. V. Butkevich, L. G. Dedenko, and I. M. Zheleznykh, "Spectra of hadrons, muons, and neutrinos in the atmosphere as the solution of a direct problem", *Sov. J. Nucl. Phys.* **50** (1989) 90–99.

[23] P. Lipari, "Lepton spectra in the earth's atmosphere", *Astropart. Phys.* **1** (1993) 195–227.

[24] G. Ingelman and M. Thunman, "High Energy Neutrino Production by Cosmic Ray Interactions in the Sun", *Phys. Rev.* **D54** (1996) 4385–4392, `hep-ph/9604288`.

[25] G. Domokos, B. Elliott, and S. Kovesi-Domokos, "Cosmic neutrino production in the Milky Way", *J. Phys.* **G19** (1993) 899–912.

[26] G. Ingelman and M. Thunman, "Particle Production in the Interstellar Medium", `hep-ph/9604286`.

[27] C. Distefano, D. Guetta, E. Waxman, and A. Levinson, "Neutrino flux predictions for known galactic microquasars", *Astrophys. J.* **575** (2002) 378–383, `astro-ph/0202200`.

[28] K. Mannheim, R. J. Protheroe, and J. P. Rachen, "On the cosmic ray bound for models of extragalactic neutrino production", *Phys. Rev.* **D63** (2001) 023003, `astro-ph/9812398`.

[29] T. K. Gaisser, "Cosmic Rays and Particle Physics", Cambridge University Press, Cambridge, U.K. (1990).

[30] Y. A. Gallant, "Particle Acceleration at Relativistic Shocks", `astro-ph/0201243`.

[31] J. P. Rachen and P. Meszaros, "Photohadronic neutrinos from transients in astrophysical sources", *Phys. Rev.* **D58** (1998) 123005, `astro-ph/9802280`.

[32] A. Mucke, R. Engel, J. P. Rachen, R. J. Protheroe, and T. Stanev, "Monte Carlo simulations of photohadronic processes in astrophysics", *Comput. Phys. Commun.* **124** (2000) 290–314, `astro-ph/9903478`.

[33] F. Halzen and E. Zas, "Neutrino fluxes from active galaxies: A model-independent estimate", *Astrophys. J.* **488** (1997) 669–674, `astro-ph/9702193`.

[34] F. Halzen and D. Hooper, "High-energy neutrino astronomy: The cosmic ray connection", *Rept. Prog. Phys.* **65** (2002) 1025–1078, `astro-ph/0204527`.

[35] M. S. Schubnell *et al.*, "Very High Energy Gamma-Ray Emission from the Blazar Markarian 421", `astro-ph/9602068`.

[36] A. Mucke, J. P. Rachen, R. Engel, R. J. Protheroe, and T. Stanev, "On photohadronic processes in astrophysical environments", *Publ. Astron. Soc. Austral.* **16** (1999) 160, `astro-ph/9808279`.

[37] L. Nellen, K. Mannheim, and P. L. Biermann, "Neutrino production through hadronic cascades in AGN accretion disks", *Phys. Rev.* **D47** (1993) 5270–5274, `hep-ph/9211257`.

[38] F. W. Stecker and M. H. Salamon, "High energy neutrinos from quasars", *Space Sci. Rev.* **75** (1996) 341–355, `astro-ph/9501064`.

[39] K. Mannheim, "Gamma-rays and neutrinos from a powerful cosmic accelerator", *Phys. Rev.* **D48** (1993) 2408–2414, `astro-ph/9306005`.

[40] T. K. Gaisser, R. J. Protheroe, and T. Stanev, "Gamma-ray production in supernova remnants", *Astrophys. J.* **492** (1998) 219, `astro-ph/9609044`.

[41] A. M. Atoyan, F. A. Aharonian, R. J. Tuffs, and H. J. Volk, "On the gamma-ray fluxes expected from Cassiopeia A", `astro-ph/0001186`.

[42] L. Bergstrom, "Non-baryonic dark matter: Observational evidence and detection methods", *Rept. Prog. Phys.* **63** (2000) 793, `hep-ph/0002126`.

[43] P. Bhattacharjee, C. T. Hill, and D. N. Schramm, "Grand unified theories, topological defects and ultrahigh- energy cosmic rays", *Phys. Rev. Lett.* **69** (1992) 567–570.

[44] I. Taboada, "Search for High Energy Neutrino Induced Cascades with the AMANDA-B10 Detector", PhD thesis, University of Pennsylvania, Philadelphia, USA (2002).

[45] J. G. Learned and S. Pakvasa, "Detecting tau-neutrino oscillations at PeV energies", *Astropart. Phys.* **3** (1995) 267–274, `hep-ph/9405296`.

[46] **IceCube** Collaboration, J. Ahrens *et al.*, "IceCube: The next generation neutrino telescope at the South Pole", `astro-ph/0209556`.

[47] R. Gandhi, C. Quigg, M. H. Reno, and I. Sarcevic, "Ultrahigh-energy neutrino interactions", *Astropart. Phys.* **5** (1996) 81–110, `hep-ph/9512364`.

[48] N. Schmitz, "Neutrinophysik", Teubner Verlag, Stuttgart, Germany (1997).

[49] H. Bichsel, D. E. Groom, and S. R. Klein, "Passage of particles through matter (Rev.)", *Phys. Rev.* **D66** (2002) 010001.

[50] J. D. Jackson, "Classical Electrodynamics", Third Edition, John Wiley & Sons, New York, USA (1998).

[51] A. Bouchta, "Muon analysis with the AMANDA-B four-string detector", PhD thesis, Stockholm University, Stockholm, Sweden, USIP-98-07 (1998).

[52] E. V. Bugaev *et al.*, "Atmospheric muon flux at sea level, underground and underwater", *Phys. Rev.* **D58** (1998) 054001, `hep-ph/9803488`.

[53] **ANTARES** Collaboration, T. Montaruli *et al.*, "ANTARES status report", Presented by T. Montaruli on behalf of the ANTARES Collaboration, to appear in the proceedings of 28th International Cosmic Ray Conferences (ICRC 2003), Tsukuba, Japan, 31 Jul - 7 Aug (2003).

[54] Z. Djilkibaev, "Light propagation in water and ice", Prepared for International Workshop on Simulations and Analysis Methods for Large Neutrino Telescopes, Zeuthen, Germany, 6-9 Jul (1998).

[55] P. B. Price, "Optical properties of ice and ocean for ultrahigh-energy neutrino astrophysics", Prepared for International Workshop on Simulations and Analysis Methods for Large Neutrino Telescopes, Zeuthen, Germany, 6-9 Jul (1998).

[56] C. Spiering, "Parameters characterizing the physics capabilities of underwater/ice neutrino telescopes", Prepared for International Workshop on Simulations and Analysis Methods for Large Neutrino Telescopes, Zeuthen, Germany, 6-9 Jul (1998).

[57] **AMANDA** Collaboration, E. Andres *et al.*, "The AMANDA neutrino telescope: Principle of operation and first results", *Astropart. Phys.* **13** (2000) 1–20, `astro-ph/9906203`.

[58] **AMANDA** Collaboration, P. Askebjer *et al.*, "Optical properties of the South Pole ice at depths between 0.8-km and 1-km", *Science* **267** (1995) 1147–1150, `astro-ph/9412028`.

[59] P. B. Price, "Kinetics of conversion of air bubbles to air hydrate crystals in Antarctic ice", `astro-ph/9501073`.

[60] **AMANDA** Collaboration, K. Woschnagg *et al.*, "Optical properties of South Pole ice at depths from 140- meters to 2300-meters", Prepared for 26th International Cosmic Ray Conference (ICRC 99), Salt Lake City, UT, 17-25 Aug (1999).

[61] P. Marciniewski, "Fast Digital Trigger Systems for Experiments in High Energy P hysics", PhD thesis, Uppsala University, Uppsala, Sweden (2001).

[62] G. C. Hill, "Experimental and Theoretical Aspects of High Energy Neutrino Astrophysics", PhD thesis, University of Adelaide, Adelaide, Australia (1996).

[63] A. M. Dziewonski and D. L. Anderson, "Preliminary reference earth model", *Phys. Earth Planet. Interiors* **25** (1981) 297–356.

[64] A. D. Martin, W. J. Stirling, and R. G. Roberts, "Parton distributions of the proton", *Phys. Rev.* **D50** (1994) 6734–6752, `hep-ph/9406315`.

[65] J. Wentz *et al.*, "Simulation of atmospheric muon and neutrino fluxes with CORSIKA", *Phys. Rev.* **D67** (2003) 073020, `hep-ph/0301199`.

[66] D. Chirkin and W. Rhode, "Muon Monte Carlo: A new high-precision tool for muon propagation through matter", Hamburg DESY - DESY-PROC-2002-01 (02/08,rec.Oct.) 15-22.

[67] A. Karle, "Monte Carlo simulation of photon transport and detection in deep ice: Muons and cascades", Prepared for International Workshop on Simulations and Analysis Methods for Large Neutrino Telescopes, Zeuthen, Germany, 6-9 Jul (1998).

[68] S. Hundertmark, “AMASIM neutrino detector simulation program”, Prepared for International Workshop on Simulations and Analysis Methods for Large Neutrino Telescopes, Zeuthen, Germany, 6-9 Jul (1998).

[69] K. Woschnagg, “Combined uncertainty in the timing calibration”, personal communication.

[70] P. Niessen, “Simulated bubbles and their effect on some observables in AMANDA-B4”, AMANDA Internal Report, A-IR/19981101 (1998).

[71] K. Woschnagg, “Optical properties of ice”, http://amanda.berkeley.edu/kurt/ice2000.

[72] S. Hundertmark, L. Kopke, and M. van der Donckt, “Proposal for AMANDA monitoring”, AMANDA Internal Report.

[73] R. Brun and F. Rademakers, “ROOT: An object oriented data analysis framework”, *Nucl. Instrum. Meth.* **A389** (1997) 81–86.

[74] J. Klug, “Enhancement of Up/Down Signal Ratio and Crosstalk studies in AMANDA”, Diploma thesis, Uppsala University, Uppsala, Sweden (1997).

[75] I. Taboada, “Cross Talk Cleaning”, Talk given at AMANDA collaboration meeting, Stockholm (2002).

[76] **AMANDA** Collaboration, J. Ahrens *et al.*, “Muon Track Reconstruction in AMANDA”, submitted to Nuclear Instruments and Methods.

[77] M. Kowalski, I. Taboada, *et al.*, “Cascade reconstruction in AMANDA”, Hamburg DESY - DESY-PROC-2002-01 (02/08,rec.Oct.) 135-139 (2002).

[78] D. Pandel, “Bestimmung von Wasser- und Detektorparametern und Rekonstruktion von Myonen bis 100 TeV mit dem Baikal Neutrinoteleskop NT-72”, Diploma Thesis, Humboldt University, Berlin, Germany (1996).

[79] W. H. Press *et al.*, “Numerical Recipes in C - The Art of Scientific Computing”, Cambridge University Press, Cambridge, UK (1997).

[80] F. James and M. Roos, "'MINUIT' a system for function minimization and analysis of the parameter errors and correlations", *Comput. Phys. Commun.* **10** (1975) 343–367.

[81] **AMANDA** Collaboration, T. DeYoung *et al.*, "Application of Bayes' theorem to muon track reconstruction in AMANDA", Prepared for Conference on Advanced Statistical Techniques in Particle Physics, Durham, England, 18-22 Mar (2002).

[82] S. M. Young, "A Search for point sources of high-energy neutrinos with the AMANDA-B10 neutrino telescope", PhD thesis, University of California, Irvine, USA, UMI-30-10279 (2001).

[83] P. Biron von Curland, Alexander, "Search for atmospheric muon-neutrinos and extraterrestric neutrino point sources in the 1997 AMANDA-B10 data", PhD thesis, Humboldt University, Berlin, Germany, DESY-THESIS-2002-025 (2002).

[84] **AMANDA** Collaboration, J. Ahrens *et al.*, "Search for extraterrestial point sources of neutrinos with AMANDA-II", submitted to Physical Review Letters.

[85] T. DeYoung, "Observation of atmospheric muon neutrinos with AMANDA", PhD thesis, Wisconsin University, Madison, USA, UMI-30-12563 (2001).

[86] T. Neunhoeffer, "Angular resolution of AMANDA-II", Talk given at AMANDA meeting, Stockholm (2002).

[87] A. Smola and B. Scholkopf, "A Tutorial on Support Vector Regression", NeuroCOLT2 Technical Report Series, NC2-TR-1998-030 (1998).

[88] A. Vaiciulis, "Support Vector Machines in analysis of top quark production", *Nucl. Instrum. Meth.* **A502** (2003) 492–494, `hep-ex/0205069`.

[89] N. Cristianini and J. Taylor-Shawe, "An introduction to Support Vector Machines and other kernel-based learning methods", Cambridge University Press, Cambridge, UK (2000).

[90] H. Goldstein, "Klassische Mechanik", (German translation), Aula-Verlag, Wiesbaden, Germany (1991).

[91] J. Mercer, "Functions of positive and negative type and their connection with the theory of integral equations", *Philos. Trans. Roy. Soc. London* **A 209** (1909) 415–446.

[92] B. Schölkopf, P. L. Bartlett, A. Smola, and R. Williamson, "Shrinking the tube: a new Support Vector regression algorithm", in *Advances in Neural Information Processing Systems 11*, M. S. Kearns, S. A. Solla, and D. A. Cohn, eds., pp. 330 – 336. MIT Press, Cambridge, MA, 1999.

[93] C.-C. Chang and C.-J. Lin, "Training ν-Support Vector Classifiers: Theory and Algorithms", *Neural Computation* **13(9)** (2001) 2119–2147.

[94] C.-C. Chang and C.-J. Lin, "LIBSVM: a library for Support Vector Machines", http://www.csie.ntu.edu.tw/∼cjlin/libsvm/.

[95] G. C. Hill and K. Rawlins, "Unbiased cut selection for optimal upper limits in neutrino detectors: The model rejection potential technique", *Astropart. Phys.* **19** (2003) 393–402, `astro-ph/0209350`.

[96] G. J. Feldman and R. D. Cousins, "A Unified approach to the classical statistical analysis of small signals", *Phys. Rev.* **D57** (1998) 3873–3889, `physics/9711021`.

[97] R. Mukherjee *et al.*, "EGRET observations of high-energy gamma ray emission from blazars: An update", *Astrophys. J.* **490** (1997) 116–135.

[98] A. Y. Neronov and D. V. Semikoz, "Which blazars are neutrino loud?", *Phys. Rev.* **D66** (2002) 123003, `hep-ph/0208248`.

[99] R. Gandhi, C. Quigg, M. H. Reno, and I. Sarcevic, "Neutrino interactions at ultrahigh energies", *Phys. Rev.* **D58** (1998) 093009, `hep-ph/9807264`.

[100] A. Goobar, "Uncertainties in the transmissitivity measurements for AMANDA OMs", personal communication.

[101] Hamamatsu, "Uncertainties in QE/CE measurements for the HAMAMATSU R5912 pmt", manufacturer specifications.

[102] A. Biron and H. Wissing, "Impact of varied OM sensitivities on the AMANDA-B10 analysis", AMANDA Internal Report, A-IR/20001202 (2000).

[103] P. Olbrechts and C. Wiebusch, “On the angular sensitivity of optical modules in ice”, AMANDA Internal Report, A-IR/20010102 (2001).

[104] D. Chirkin, “Muon range uncertainties in MMC”, personal communication.

[105] S. Hundertmark, “Vertical ice properties for the AMANDA simulation”, AMANDA Internal Report A-IR/20001001 (2000).

[106] A. Biron, “Reconstruction Uncertainties due to Time Calibration errors”, AMANDA Internal Report, A-IR/20001101 (2000).

[107] J. Neyman, “Outline of a Theory of Estimation Based on the Classical Theory of Probability”, *Philos. Trans. Royal Soc. London* **A 333** (1937) 333–380.

[108] A. Stuart and J. K. Ord, “Kendall’s Advanced Theory of Statistics, Vol 2: Classical Inference and Relationship”, Oxford University Press, New York (1991).

[109] B. P. Roe and M. B. Woodroofe, “Improved probability method for estimating signal in the presence of background”, *Phys. Rev.* **D60** (1999) 053009, `physics/9812036`.

[110] **Particle Data Group** Collaboration, C. Caso *et al.*, “Review of particle physics”, *Eur. Phys. J.* **C3** (1998) 1–794.

[111] J. Conway, “Inclusion of systematic uncertainties in upper limits and hypothesis tests”, 1st Workshop on Confidence Limits, CERN, Geneva, Switzerland, 17-18 Jan (2000).

[112] R. D. Cousins and V. L. Highland, “Incorporating systematic uncertainties into an upper limit”, *Nucl. Instrum. Meth.* **A320** (1992) 331–335.

[113] G. C. Hill, “Comment on [Including systematic uncertainties in confidence interval construction for Poisson statistics]”, *Phys. Rev.* **D67** (2003) 118101, `physics/0302057`.

[114] G. Feldman, “Multiple Measurements and Parameters in the Unified Approach”, 2nd Wokshop on Confidence Limits, FERMILAB, Chicago, USA (2000).

[115] O. Botner, J. Conrad, A. Hallgren, and C. P. de los Heros, "On the possibility of measuring neutrino oscillations With AMANDA-II using contained events", AMANDA internal report (2000).

[116] O. Botner, J. Conrad, A. Hallgren, and C. P. de los Heros, "On the sensitivity of AMANDA-II and B10 to oscillation parameters using zenith angle distribution", AMANDA internal report (2000).

[117] **ANTARES** Collaboration, P. Amram *et al.*, "A Deep Sea Telescope for High Energy Neutrinos", http://antares.in2p3.fr/antares/.

Acknowledgements

First of all I would like to thank my thesis adviser Allan Hallgren for his continuous stream of ideas, questions, answers and shared insights without which this thesis would be much more of a joke.
I am also very grateful to Olga Botner, my co-adviser, for all her professional but also (at times) moral support and for pushing in the right directions at the right times in order to keep me on track. Olga has the rare gift of letting one feel that criticism is meant to help and nothing else.
When I first came to ISV I had never touched a FORTRAN program or seen a PAW kumac. In this time the help of Carlos P. de los Heros was crucial. Later on he continued to be helpful with all kinds of technical and physics questions and was always open for discussion, usually useful, always interesting. Thanks a lot !
Olga, Allan and Carlos are thanked for essentially being available for answering questions or discussing issues at any time (and this is thought of as a message to future PhD students).
I guess, the whole AMANDA collaboration contributed in one or the other way to the completion of this thesis. Some people however more directly than others: Thanks to Peter Niessen for setting up the 99 Monte Carlo, Paolo Desiati for help with the Wisconsin cluster and several simulation issues, Tonio Hauschildt and David Steele for useful discussion about their (and my) point source analysis, Alexander Biron for help with coordinate transformations, Othmane Bouhali for providing cross talk filtered data and FIM MC, Darryn Schneider for keeping the Wisconsin cluster up and running most of the time, Till Neunhoeffer for help with installing the parabola fit software, Francis Halzen for a hint in the writing of this theory part and Gary Hill for information on nusim and for being one of the few (if not the only one) listening to me when I talked about statistics.
Thanks to Chih-Jen Lin for his support with the Support Vector Machine package. Regarding the limit calculation method I benefited greatly from discus-

sions with Robert Cousins.
Thanks to Allan, Carlos and Adam Bouchta for reading the manuscript and many useful suggestions for improvement. Special thanks to Olga for her very thorough reading and for even checking the math in the theory and analysis sections.
Part of the data analysis has been performed at the National Supercomputer Center in Linköping whose support is herewith acknowledged.
In Uppsala I'd like to thank Adam Bouchta for a number of interesting discussions and suggestions during the last year of my thesis. Thanks also to Jö Fahlke who was very helpful in the transition from UNIX to LINUX and to Anna Davour for being a considerate office mate. I am grateful to Ib Koersner for his extremely efficient system administration. A huge thanks goes to Inger Ericson who always had an eye on me and who is running the whole place anyway.
Thanks to Mårten Stenmark (amongst many other things for being the only sane person in the institute) and to Fredrik Tegenfeldt (amongst many other things for the Käbi Läretei story). My apologies to Bernhard Huber for all the beers we did not drink.
Danke meinen Eltern, Monika und Wolf-Dietrich Conrad, und meiner Großmutter, Lenore Orlowski, für all die Unterstützung während der letzten 30 Jahre. Und zuletzt:
Köszönct én drága, szeretett Rékucim. Azért, hogy létezel és tartalmat adsz életemnek, hogy doktori tanulmányaim legkeményebb évét életem legboldogabb évére varázsoltad.

Uppsala, September 2003